UNIVERSITA' DEGLI STUDI DI PADOVA
DEPARTMENT OF INDUSTRIAL ENGINEERING

MASTER DEGREE COURSE IN ELECTRICAL ENGINEERING

MASTER THESIS

" Models and tests of induction contour hardening process "

SUPERVISOR: Ing. Forzan Michele
CO-EXAMINER: Prof. Bocher Philippe (ETS, Montréal)
Ing. Spezzapria Mattia

GRADUATE: Lorenzo Ciccarone

SESSION 2013/2014

Ringraziamenti

“Ai miei genitori che mi hanno sempre supportato in tutte le decisioni prese;
A mio fratello per avermi ispirato nella scelta degli studi in ingegneria;
A Carolina per la serenità e felicità che mi ha dato in questi anni,
e che continuerà anche nei prossimi;
Ai miei compagni d’avventura,
in particolare Marco, Nicolò, Martino, Davide e Giovanni,
che mi hanno sopportato e con i quali mi son divertito in questi anni;
A tutti i miei amici di sempre che mi hanno dato il giusto svago;
Al professor Forzan che mi ha dato l’irripetibile opportunità
di svolgere quest’interessantissima tesi
in un paese speciale come il Canada;
Al professor Bocher per avermi accolto
e seguito durante la permanenza presso i laboratori dell’ETS a Montréal;
All’ingegner Spezzapria che mi ha guidato e consigliato in quest’esperienza.”

Abstract

I processi di riscaldamento d'induzione magnetica stanno diventando sempre più utilizzati nella vita quotidiana, basti pensare ai fornelli ad induzione che si stanno diffondendo in tutte le cucine, grazie ai quali cucinare è diventato più veloce ed efficiente. Anche nei processi industriali il riscaldamento ad induzione è sempre più usato per gli stessi motivi: per ottenere lavorazioni molto veloci, e ottimizzare l'utilizzo dell'energia elettrica. Purtroppo non può essere applicata in tutti i settori elettrotermici, ma è particolarmente indicato nei processi di tempra, dove porta notevoli miglioramenti in diversi punti di vista rispetto alla carbocementazione. In particolare in questo scritto è analizzata la tempra ad induzione delle ruote dentate, realizzando prima un modello di simulazione numerica tramite software di calcolo agli elementi finiti, e successivamente effettuando dei test per poter verificare l'attendibilità del modello elaborato. La difficoltà principale nel test è la misurazione delle temperature nel pezzo, visto che vi sono delle variazioni fino a migliaia di gradi in pochissimi secondi. Per questo motivo è stata utilizzata una tecnica innovativa basata sull'utilizzo di speciali vernici sul pezzo da analizzare che hanno la proprietà di evaporare ad una ben precisa temperatura e di una potente videocamera ad alta velocità. In questo modo è possibile determinare con buona precisione la distribuzione di determinate temperature sulla superficie del pezzo.

Abstract

Processes concerning the magnetic induction are becoming increasingly used in everyday life , like the induction cookers that are spreading in every kitchen, thanks to which cooking has become faster and more efficient. Even in industrial processes the induction heating is increasingly being used for the same reasons : to obtain very fast processing, and optimize the use of electricity. Unfortunately it cannot be applied in all sectors of electroheat, but it is particularly suitable in the process of hardening, where in differents ways is a major improvement respect to the carburizing. In this paper is analyzed the induction hardening of gears, first realizing a numerical simulation model using finite element software , and then carrying out the tests in order to verify the model developed . The main difficulty in the test is the detection of temperatures in the piece, as there are variations of thousands of degrees in a few seconds. For this reason it has been used a novel technique based on the use of special coatings on the analyzed workpiece that have the property to evaporate at a precise temperature and with a powerful high speed video camera. In this way it's possible to determine with good accuracy the distribution of certain temperatures on the surface of the gear.

Contents

I Theory 5

1 Hardening Process 7
- 1.1 Fe-C Diagram 7
- 1.2 Heating Process 10
- 1.3 Quenching 12
- 1.4 Tempering 15

2 Induction Heating 16
- 2.1 Introduction 16
- 2.2 Magnetic Theory 17
- 2.3 Skin Effect 25
- 2.4 Thermic Theory 26
- 2.5 Induction Hardening 27
- 2.6 Complex geometries: Gears 28

3 Power Supply 31
- 3.1 Types of Power Supplies 31
- 3.2 Voltage-fed series resonant inverters 33
  - 3.2.1 Resonant frequency 33
  - 3.2.2 Quality factor 34
  - 3.2.3 Power in the workpiece 34
- 3.3 Current-fed parallel resonant inverters 35
  - 3.3.1 Resonant frequency 36
  - 3.3.2 Power in the workpiece 36
- 3.4 Regulation 37

4 Induction Coils 38
- 4.1 Magnetic Flux Concentrator 38
- 4.2 Coil Characteristics Versus Frequency 40

5 Finite Element Method on 2D Gear 41
- 5.1 Formulation 41
- 5.2 Weigthed Residual Method 42
- 5.3 Building Stiffness Matrix K and Mass Matrix M 43
- 5.4 Boundary Conditions 44
- 5.5 Meshing 44

5.6 Results 45
5.6.1 Magnetic Field H 45
5.6.2 Current Density J 46

II Simulation **47**

6 Material Properties: AISI 4340 **50**
6.1 Electric Resistivity 50
6.2 Relative Magnetic Permeability 50
6.3 Volumetric Heat Capacity 51
6.4 Thermic Conductivity 53

7 Modelization of Induction Hardening on Cyinder **54**
7.1 Geometry 54
7.2 Mesh 55
7.3 Material Caratherization 56
7.4 Scenario and Solution 59
7.5 Parametric Solution 61
7.5.1 Curie Temperature 61
7.5.2 Central Temperature Volumetric Heat 61
7.6 Costant Power Solution 62

8 Modelization of Induction Hardening on a gear **65**
8.1 Geometry 65
8.2 Mesh 66
8.3 Formulations 67
8.4 Scenario 68
8.5 Solutions 68
8.6 Linear vs Non Linear B-H Relationship 70
8.7 Considerations 73

III Experimental Test **75**

9 Induction Hardening Machine: EFD SINAC 650 **77**
9.1 Different Working Modality 78

10 Data Acquisition **80**

11 Test on Simple Geometry **83**

11.1 Comparison Costant Power vs Costant Current 83

11.2 Results 83

12 Test on Gear: EFD112539 **85**

12.1 Model Construction 87

12.2 Test and Solutions 87

12.3 Results 89

12.4 Edge Effect 91

12.5 Conclusions 94

Part I

Theory

1 Hardening Process

Hardening is the particular process that makes a material, in the specific case steel, harder. The hardness of a metal is directly proportional to the uniaxial yield stress at the location of the imposed strain. A harder metal will have a higher resistance to plastic deformation than a less one. Harder materials are required for many applications:

- construction materials - high strength reduces the thickness of material which generally saves weight and cost.
- machine cutting tools (drill bits, taps, lathe toos) which must be harder than the material they are opertating on in order to be effective.
- knife blades - a high hardness blade keeps a sharp edge.
- bearings - necessary to have a very hard surface that will withstand continued stresses.
- armor plating - high strength is extremely important both for bullet proof plates and for heavy duty containers for mining and construction.
- anti-fatigue - superficial hardening can drastically improve the service life of mechanical components with repeated loading/unloading , such as axels, cogs and gears.

To fully understand of the hardening process is important the get the carateristichs of metals, in particular the martensitic transformation.

1.1 Fe-C Diagram

The description of the characteristics of steel products and their possible applications can not ignore the knowledge of the equilibrium structures of various alloys as a function of the percentage of carbon and temperature. These structures are represented in the diagram of equilibrium Fe-C. The iron and carbon combinate to form the carbide Fe3C, containing 6.67% by weight of carbon. It's of practical interest only that region of the Fe-C diagram regarding the alloys with a carbon content between 0 and 6.67%. The pure iron is polymorphic and can occur in several allotropic modifications:

- α-iron, body centered cube (BCC) , stable still 911°C.
- γ-iron, face centered cube (FCC), stable still 1392°C.
- δ-iron, body centered cubo (BCC), stable still 1536°C (fusion point).

In the study of phenomena that occur in iron-carbon alloys during solidification and cooling, it is necessary to consider on the one hand the formation, modification, and the disappearance of some phases, and the other hand the nature, morphology and the kinetics of

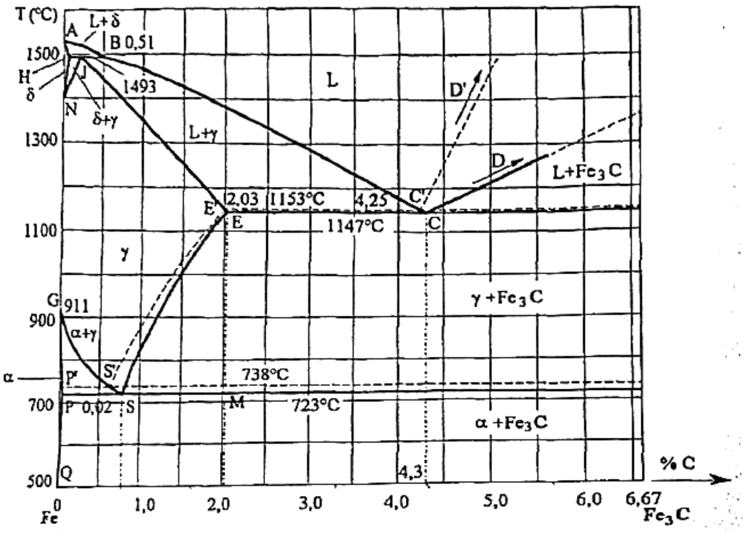

Figure 1.1: Fe-C Diagram [limited at 6,67% of C]

formation of other structural components.The temperatures at which the transformations take place by a variety allotropic to others are indicated with the letter A (anomaly) followed by an numeric index established conventionally. To the pure iron with A4 indicates the temperature of the $\gamma - \delta$ transformation (1392 °) and with that of the A3 transformation $\alpha - \delta$ (911 °). For alloys based on Fe, so also for Fe-C, the following critical points are defined:

- A4: temperature where under there is stable austenite, and above there is δ-ferrite, in the figure it is defined by the line NJ

- A3: temperature where under there is α-ferrite, and above there is stable austenite, in the figure it is defined by the line GSM

- A1: temperature where there is the equilibrium between austenite and paerlite, in the figure it is defined by the line PM

Usually the steel for hardening has a concetration of C about 0.4 % , so we analyse only that part of the diagram, neglecting also the δ-fase which doesn't influence the result of solidification, as we can see in figure below.

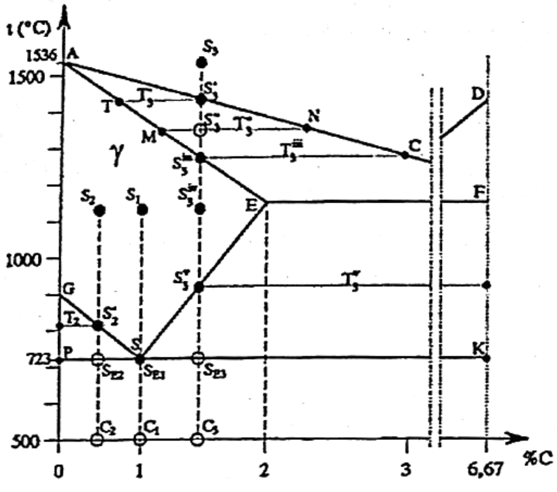

Figure 1.2: Fe-C Diagram simplified

Please note the two fundamental aspects:

- The solubility of carbon in Fe-γ decreases with decrease in temperature;
- The existence of the allotropic transformation of Fe-γ in Fe-α.

If the alloy has a carbon concentration lower than 0.8% is said "hypoeutettoidic", and follows the curve indicated by S_2. In this alloy the austanite cools without undergoing trasformations to the point $S_2^{'}$, located on the line GS. Here appear the first crystals of ferrite-α primary, that increase with decreasing temperature. Correspondingly, the amount of austenite decreases, enriched in carbon. Lowering the temperature to the eutettodic horizon, the system is constituted by ferrite-α and by austenite that has gradually enriched in carbon to reach the eutettodic composition (C=0.8%). From this, about 723 ° C, begin to form the first of pearlite nodules. The temperature remains constant until all the eutettodic austenite became pearlite. At room temperature, the alloy is therefore constituted by crystals of primary α-ferrite in a matrix of pearlite, the phases are only α-ferrite and Fe_3C.

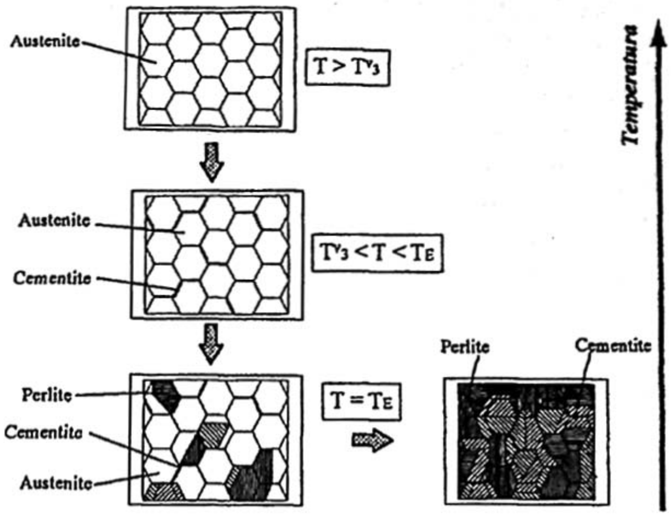
Austenite
T > T'3
Austenite
Cementite
T'3 < T < TE
Perlite
Cementite
Austenite
T = TE
Perlite
Cementite
Temperatura

Figure 1.3: Schematic representation of the structures assumed by a steel ipereutettoidico during a slow cooling.

1.2 Heating Process

The heating in the hardening process consists in bringing the piece to a temperature greater than AC3, so as to complete the transformation austenitic steel. However, this temperature is not simple to calculate, because it depends also from the other elements that make up the steel, which can then raise it or lower it, as seen in the figure. Furthermore, the Fe-C diagram is valid in "thermodynamic equilibrium", which means that the temperature

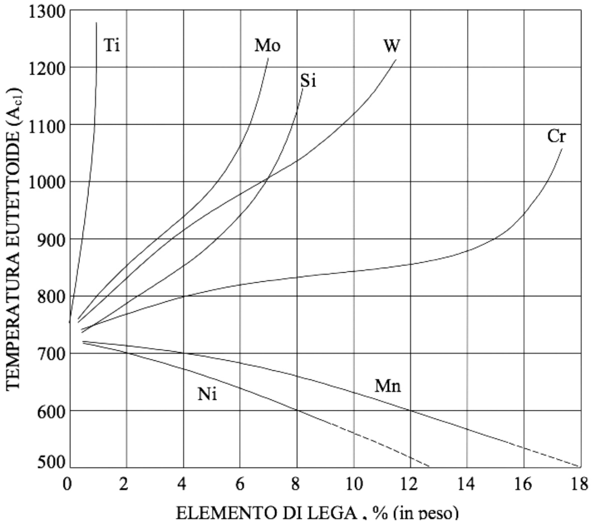

Figure 1.4: Influence of alloying elements on the Ac1 temperature

variations are infinitesimal. The trasformation temperatures Ac1 and Ac3 depend both from composition of the steel and from the heating speed.

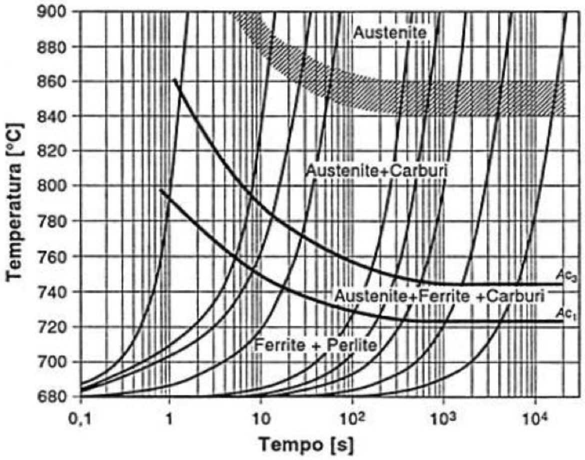

Figure 1.5: Continuous Heating Transformation Curves

1.3 Quenching

The speed and the fluids by which it is carried out the cooling elements are fundamental for determining the result of hardening. The influence of cooling rate on the structure of the hardened material is highlighted by the Bain diagram characteristic of every steel, shown in the figure.

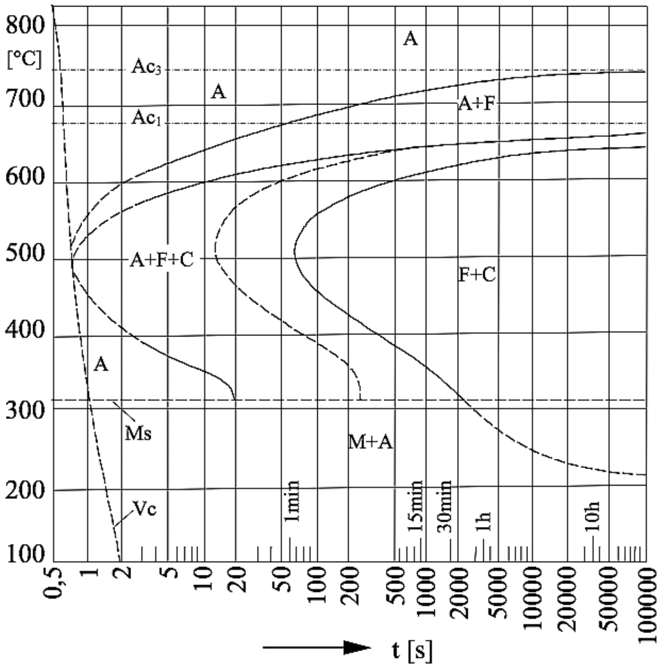

Figure 1.6: TTT Bain Curve

The curves of this diagram, also called TTT curves (Temperature - Time - Transformation), represent the locus of points of start and end of the isothermal transformations at the various temperatures indicated. The left curve joins all the points representing the time required, at various temperatures, for the beginning of the austenite transformation, with the right curve instead represent all the points, at various temperatures, the time needed for the austenite transformation to complete. In the lower part of the graph there are two horizontal lines which correspond to the critical points Ms and Mf: they are the temperatures at which, for a certain cooling speed, that start and complete the transformation of austenite into martensite, respectively. In reality most of the cooling is continue, so there are applied anisothermal diagrams, or curves CCT (Continuous - Cooling - Transformation), in which occurs a shift to the right of the curves start and end processing, but which are substantially similar to that described above. Indeed, the cooling curves, plotted on the diagram from the Ac3 temperature with different speeds, the curves intersect the start and end processing at different points, giving rise to different structures of the hardened zone at the end of cooling.

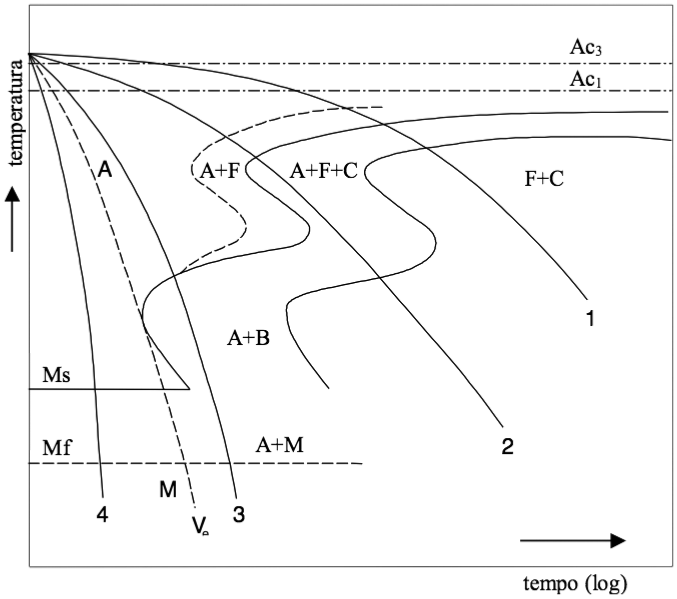

Figure 1.7: Influence of cooling speed on the final structure

In particular, for the cooling rate greater than or equal to the critical speed of quenching Vc, the curve 4 avoids intersections both the area of pearlitic transformation that bainitic one: it has the total transformation of austenite into martensite, and then realizes the complete hardening. The choice of the cooling fluid has importance not less than the cooling mode, this choice is related to the properties and the type of steel and shape and size of the piece that we want to obtained. The most used material for quanching are: water, oil, emulsions of oil, solutions of water and salts, air, molten salts and polymers based fluids. These help getting cooling rate very different from each other and then let choose the most appropriate quanching speed. It is necessary, on the one hand, that the cooling is particularly fast, but on the other, that below the martensitic temperature the cooling rate is as low as possible. In fact, a too fast change of volume induces considerable internal stresses that can determine deformations and cracks. During the quenching of steel in liquid media, the process may be split into the following three stages: (a) the vapor blanket stage, (b) the boiling stage, and (c) the convection stage.

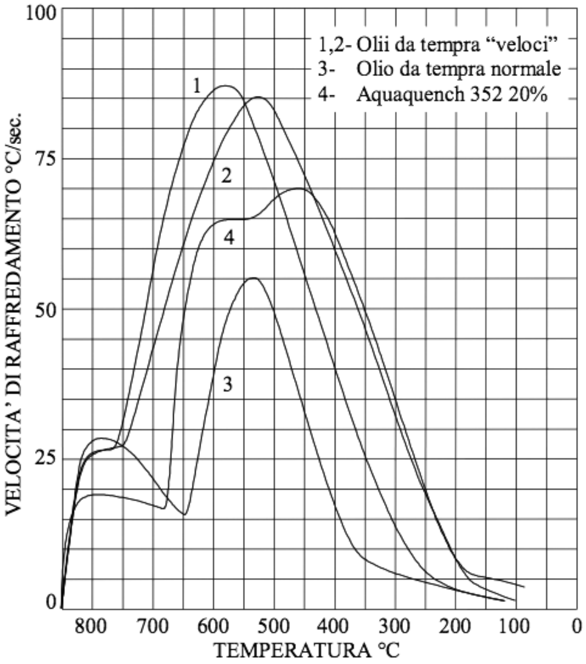

Figure 1.8: Cooling rates for polymer based fluids

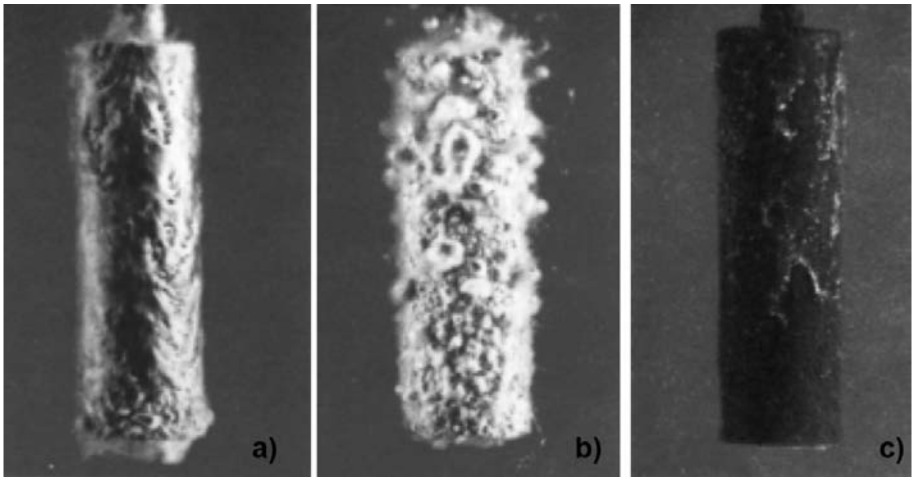

Figure 1.9: Photo sequence of a hot steel rod being quenched. (a) When the rod is immersed, a polymer film forms on its surface. (b) After 25 s, boiling occurs over the entire rod as the cooling rate increases. (c) After 75 s, quenched liquid has completely redissolved, and the heat removal is achieved entirely by convection.

The vapor blanket stage occurs when the workpiece is first quenched for cooling from austenite. The very hot surface temperature of the workpiece vaporizes the quenchant, and a thin vapor pocket forms around the work- piece. Heat transfer occurs by radiation and conduction through the vapor blanket, which acts essentially as an insulating layer because of the relatively poor conductivity of a vapor. The vapor stage is a period of relatively slow cooling, and the cooling effect of various quenchants varies greatly due to the differences in the thickness of vapor pockets that are formed.The boiling stage is the second stage of cooling. The vapor pocket collapses, and the quenchant comes into contact with the hot metal surface of the part, resulting in nucleate boiling to cool the part. This stage of quenching typically has the highest rate of heat extraction.The convection stage is the third stage of cooling, and it starts when the surface temperature of the part being cooled decreases below the boiling point of the quenchant. Heat transfer occurs by direct contact between the surface of the part being cooled and by convection of heat through the quenchant. The cooling rate is low because of the low temperature differential between the part being cooled and the quenchant.

1.4 Tempering

Steels are tempered to obtain specific values of mechanical properties, to relieve quenching stresses, and to ensure dimensional stability. The highest hardness produced for any given steel without any other surface process is obtained by quenching to a fully martensitic microstructure. A high hardness characteristic of a martensitic microstructure is produced from the straining of the iron lattices by the carbon. Because hardness is directly related to tensile strength, steel composed of 100% martensite is at its strongest possible condition. However, the condition of highest strength is also the condition at which steel is most subject to brittle fracture due to lack of ductility.

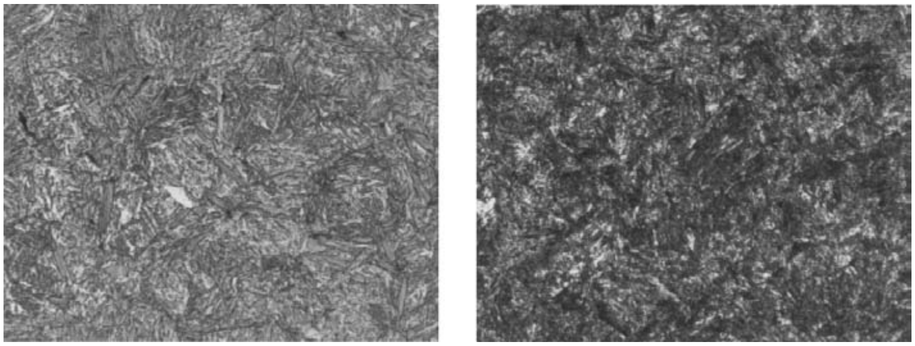

Figure 1.10: Left: Untempered martensite. Right: Tempered martensite.

2 Induction Heating

2.1 Introduction

Induction heating is one of the most used techniques for heating electrically conductive materials, most of the cases consisting of metals. The advantages of this technology, that make it irreplaceable in many industrial processes, are the follows:

- heating starts inside the piece
- localization of heating in specific zones of the piece
- high energy efficiency of process
- constancy of the finished product characteristics , due to the high repeatability of the process
- lack of thermally inert components, so short heating cycles
- leakage of losses outside the pieces, with better working conditions for operators

The main sectors of application of this technology are:

- Hardening
- Lamination of hot metals
- Welding
- Fusion of metals

2.2 Magnetic Theory

> *"Take, for example, the reciprocal electrodynamic action of a magnet and a conductor. The observable phenomenon here depends only on the relative motion of the conductor and the magnet, whereas the customary view draws a sharp distinction between the two cases in which either the one or the other of these bodies is in motion. For if the magnet is in motion and the conductor at rest, there arises in the neighbourhood of the magnet an electric field with a certain definite energy, producing a current at the places where parts of the conductor are situated. But if the magnet is stationary and the conductor in motion, no electric field arises in the neighbourhood of the magnet. In the conductor, however, we find an electromotive force, to which in itself there is no corresponding energy, but which gives rise—assuming equality of relative motion in the two cases discussed—to electric currents of the same path and intensity as those produced by the electric forces in the former case".*
>
> — Albert Einstein, On the Electrodynamics of Moving Bodies

For an initial analysis of the phenomenon, let's consider a massive cylinder of constant resistivity and permeability, and around it is disposed an induction coil powered by sinusoidal current.

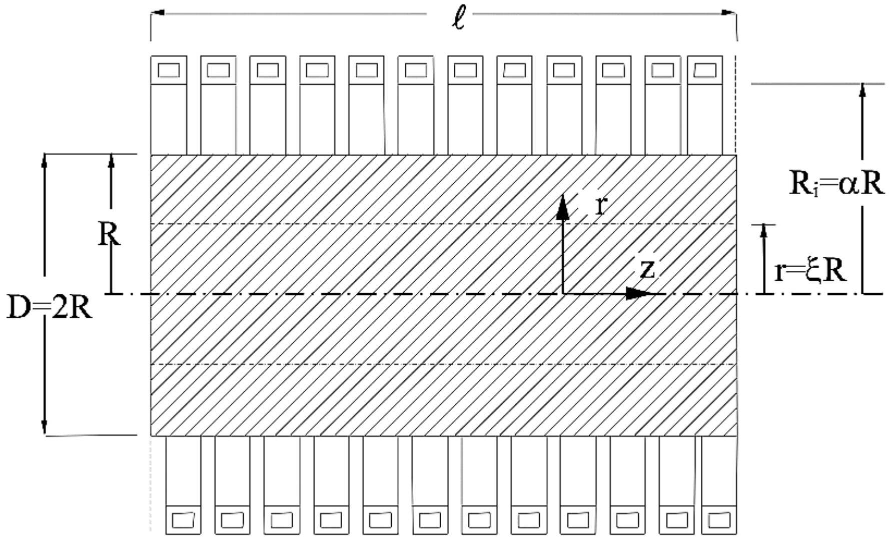

Figure 2.1: Model of inductor and load

Let's define some adimensional parameters in cylindrical coordinates (r,φ,z):

$$\xi = \frac{r}{R}$$

$$\alpha = \frac{R_i}{R}$$

Assuming the length l as a portion of a cylindrical configuration of infinite length, the intensity of the magnetic field in the space between the inductor and the cylinder has a direction along the axis z and the intensity is practically equal to :

$$\dot{H}_0 = \frac{N\dot{I}}{l}$$

For the frequencies used in these processes, we neglect the displacement currents, so we can write Maxwell's equations in this form:

$$\left\{\nabla \times \bar{H} = \tfrac{\bar{E}}{\rho} \quad ; \nabla \times \bar{E} = -j\omega\mu\mu_0\bar{H}\right. \tag{2.1}$$

So, considering the particular geometry, we obtain:

$$\frac{d^2\dot{H}}{dr^2} + \frac{1}{r}\frac{d\dot{H}}{dr} - j\frac{\omega\mu_0\mu}{\rho}H \dot{=} 0 \tag{2.2}$$

Let's introduce others fundamentals paremeters to simplify the calculations, starting from the so called "*skin dept*":

$$\delta = \sqrt{\frac{2\rho}{\omega\mu\mu_0}}$$

$$m = \frac{\sqrt{2}R}{\delta}$$

So we obtain

$$\frac{d^2\dot{H}}{d\xi^2} + \frac{1}{\xi}\frac{d\dot{H}}{d\xi} - jm^2\dot{H} = 0 \tag{2.3}$$

As well known the solution of this type of equation is obtained by Bessel equation:

$$\dot{H} = \dot{H}_0\frac{ber(m\xi) + j\,bei(m\xi)}{ber(m) + j\,bei(m)} \tag{2.4}$$

The chart in the figure shows how, due to the eddy currents, the field lines are concentrated mostly in the surface layers of the cylinder. This phenomenon is more pronounced greater is the value of m.

Simillary we can calculate the distribution of current density in the piece.

$$\dot{G} = \frac{\dot{E}}{\rho} = -\frac{\dot{H}_0}{R}m\frac{ber'(m\xi) + j\,bei'(m\xi)}{ber(m) + j\,bei(m)} \tag{2.5}$$

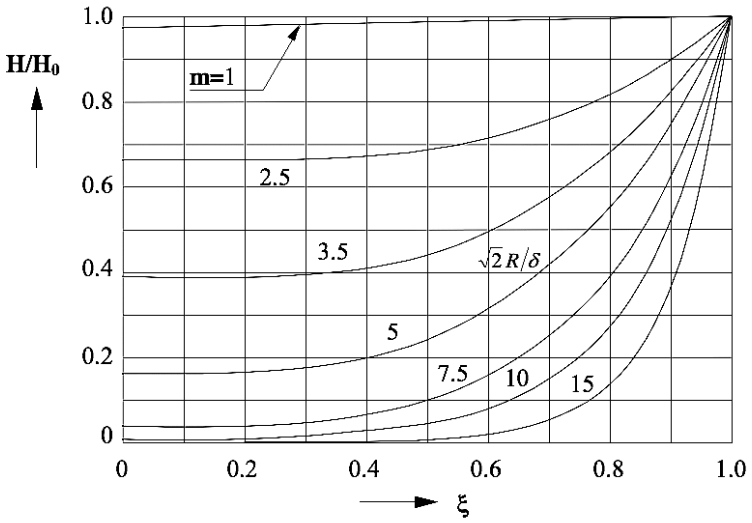

Figure 2.2: Distribution along r of magnetic field with different values of m

Also in this case the magnitudes inside the cylinder are reduced in amplitude compared to those on the surface. In fact, the current density is always zero in correspondence to the cylinder axis and, as m increases, is concentrated in a layer thinner and thinner under the surface.

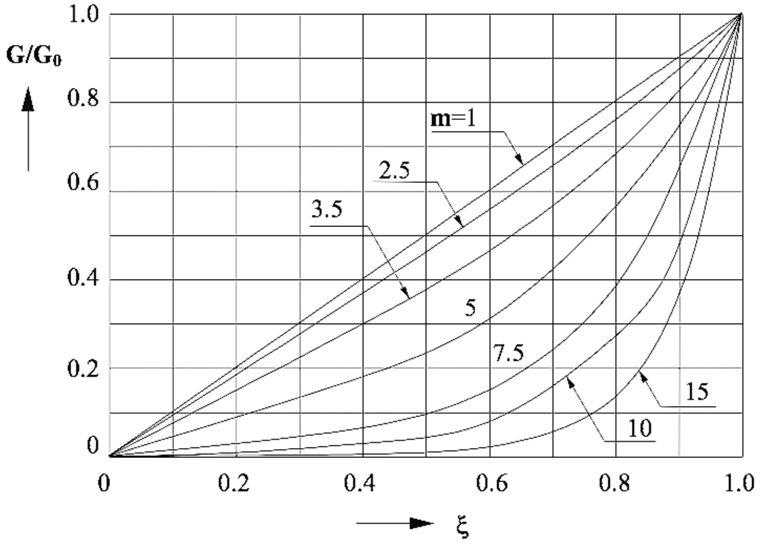

Figure 2.3: Distribution along r of current density with different values of m

Distributions along the radius of the specific power induced per unit volume are obtained easily from those of the current density, infact

$$W = \rho G^2 = W_0 \frac{ber'^2(m\xi) + bei'^2(m\xi)}{ber'^2(m) + bei'^2(m)} \tag{2.6}$$

In the figure there are the diagrams of the power density: they show that the specific power is always distributed unevenly inside the cylinder, with trends rapidly from the surface towards the axis and highly variable in function of the parameter m. It follows that the induction heating is more useful for differentiated surface heating with the frequency increase.

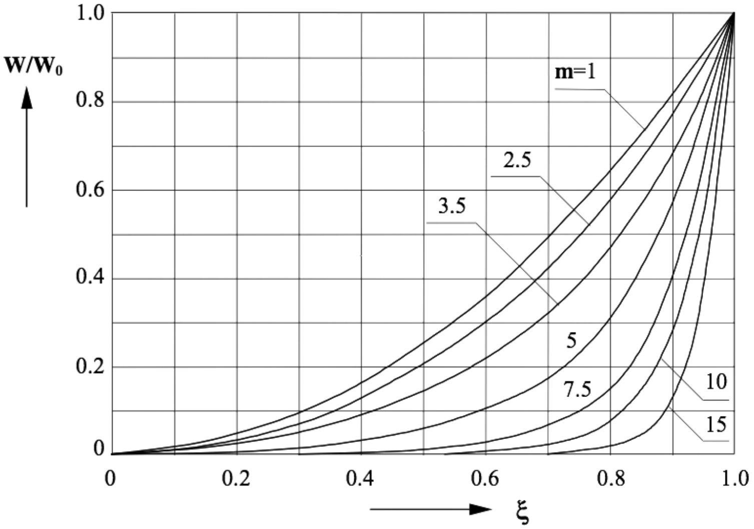

Figure 2.4: Distribution along r of power density with different values of m

Now let's introduce some parameters that simplify the tractation of the problem, like P,Q and A,B which depends only from Bessel functions, and are rapresented in function of m in the chart of the figure.

$$P + jQ = \frac{ber'm + jbei'm}{berm + jbeim} \;;\; A + jB = \frac{2}{m}(P + jQ)$$

Using the integration of the Poynting vector we can derive the active and reactive power transmitted in the piece.

$$P_c + jQ_c = -\dot{E}_0 \dot{H}_0 2\pi R\ell = H_0^2 \frac{\rho}{\delta} \sqrt{2}(P + jQ) 2\pi R\ell \tag{2.7}$$

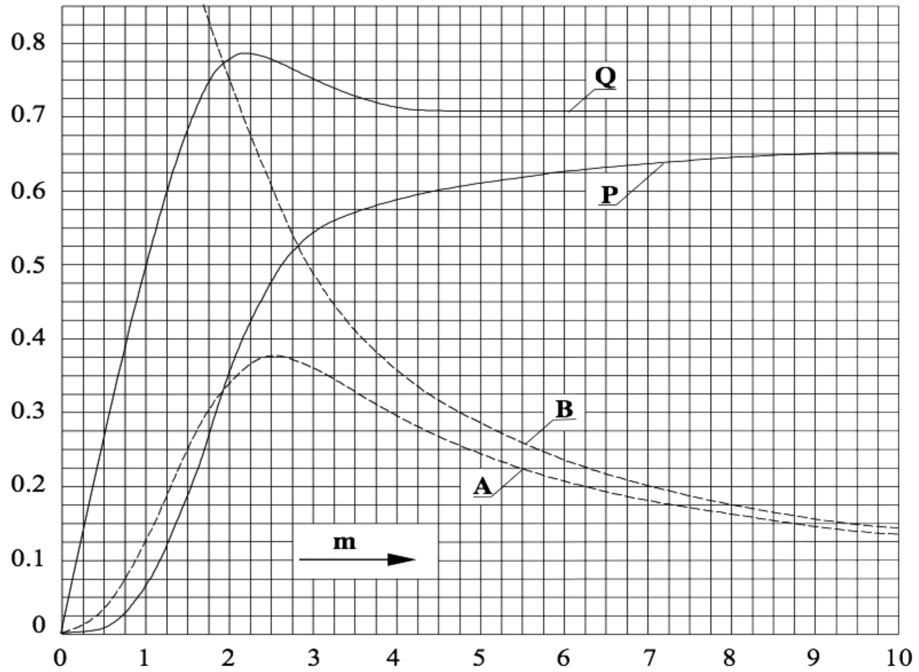

Figure 2.5: Plot of coefficients P,Q and A,B

Let's define the reactance of the induction coil in the absence of load and considered as a portion of the length l of a configuration infinitely long.

$$x_{i0} = \omega N^2 \frac{\mu_0 \pi R^2 \alpha^2}{\ell} \tag{2.8}$$

In that way the formula 7 becomes:

$$P_c + jQ_c = \frac{x_{i0}}{\alpha^2} \mu (A + jB) I^2 \tag{2.9}$$

Assuming an ideal inductor resistance as zero, consisting of a layer of current radial thickness negligible located to the radius Ri, the determination of the impedance of the equivalent system also requires the calculation of the reactive power Qa put into count in the space of air between the cylinder and the coil, in which the intensity of the magnetic field is H0.

$$Q_a = \frac{x_{i0}}{\alpha^2} (\alpha^2 - 1) I^2 \tag{2.10}$$

So the total power results:

$$P_c + j(Q_a + Q_c) = \frac{x_{i0}}{\alpha^2} \left\{ \mu A + j \left[\alpha^2 - (1 - \mu B) \right] \right\} I^2 \tag{2.11}$$

The equivalent impedance is then easily calculated as:

$$Z_{e0} = r'_c + j(x_a + x'_c) \tag{2.12}$$

With

$$r'_c = \frac{x_{i0}}{\alpha^2}\mu A \ ; \ x'_c = \frac{x_{i0}}{\alpha^2}\mu B \ ; \ x_a = \frac{x_{i0}}{\alpha^2}(\alpha^2 - 1) \tag{2.13}$$

Increasing the frequency, at constant field H0, increases the active power delivered to the load and simultaneously decreases the thickness of the surface layer within which said power is put into count. Thereby performing the heating at high frequencies it is possible to use significant values of specific power, as is necessary for example in the case of surface hardening.

In similar way we calculate also the total power in the inductor with the formula:

$$P_i + jQ_i = H_0^2 \frac{\rho_i}{\delta_i}(A_i + jB_i)2\pi R_i \ell_i \tag{2.14}$$

So we obtain the values of resistence and reactance of the inductor:

$$r_i = x_{i0}\frac{\delta_i}{R_i}A_i k_i \ ; \ x'_i = x_{i0}\frac{\delta_i}{R_i}B_i \tag{2.15}$$

Note that the parameter ki is a coefficient greater than one that takes into account the axial spacing between coils. The electrical efficiency of the inductor coil with load is calculated as ratio between the power trasformated in heat in the body and the total active power absorbed by the inductor, as shown in the formula

$$\eta_e = \frac{r'_c}{r_i + r'_c} = \frac{1}{1 + \frac{R_i \ell \delta A_i k_i}{R \ell_i \delta_i \sqrt{2}P}} \tag{2.16}$$

For high values of m, quantities like $A_i k_i$ and $\sqrt{2}P$ tend to 1, and if the inductor is well dimensioned, so $\ell = \ell_i$, the maximum efficiency is calculated with the formula:

$$\eta_{e\,max} = \frac{1}{1 + \alpha\sqrt{\frac{\rho_i}{\rho\mu}}} \tag{2.17}$$

The curves reveal that for m> 2.5 the electrical efficiency of the inductor is virtually independent of frequency, while below this value, the heating is not convenient. The efficiency also decreases significantly to vary the ratio of α, especially in the case of non-magnetic materials or magnetic materials above the Curie point. Finally, the efficiency reaches values sufficiently good (about 90%) in the heating of magnetic steels or high resistivity materials, while always remains at rather low values (50%) in the case of materials

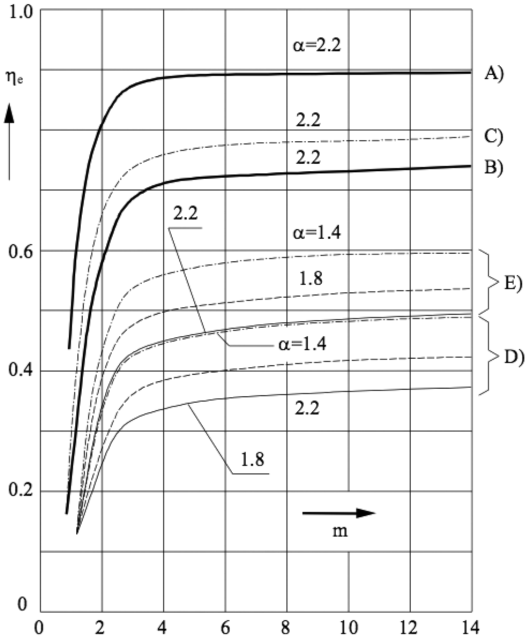

Figure 2.6: Electrical efficiency of the inductor-load system as a function of m

of low resistivity.

The merit factor is known as the ratio between the active and the reactive power absorbed by the inductor (neglecting xi)

$$Q_0 = \frac{x'_c + x_a}{r_i + r'_c} = \frac{\alpha^2 - (1 - \mu B)}{\mu A}\eta_e = Q'_0\eta_e \tag{2.18}$$

Q'_0 is the merit factor of the system in the case of ideal inductor with no resistance, which plot is indicated in Figure . Hence, to obtain the real merit factor simply multiply by the efficiency of the inductor.

In a similar way we can calculate the power factor using the formula, with the values shows in Figure:

$$cos\varphi = \frac{r_i + r'_c}{\sqrt{(r_i + r'_c)^2 + (x_a + x'_c)^2}} = \frac{1}{\sqrt{1 + (Q'_0\eta_e)^2}} \tag{2.19}$$

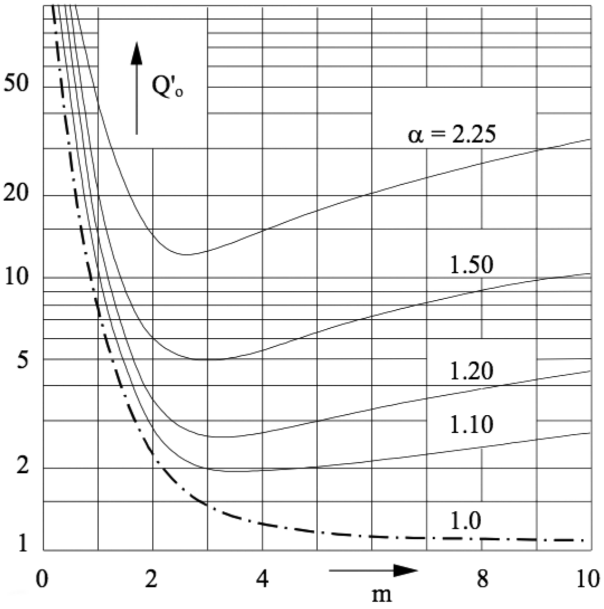

Figure 2.7: Value of the merit factor as a function of m (null inductor resistance)

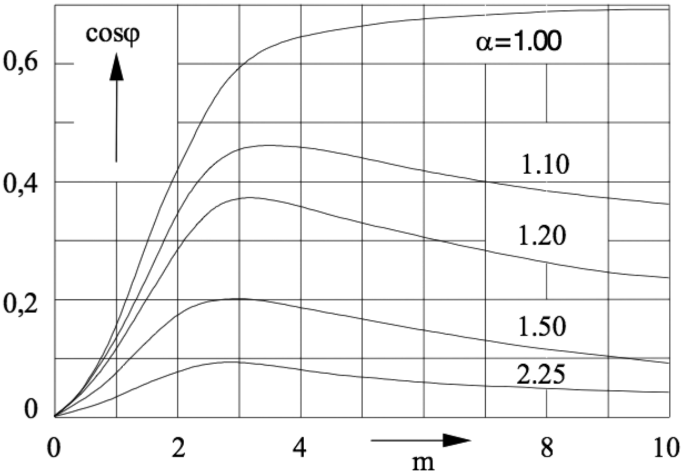

Figure 2.8: Values of power factor in function of m

2.3 Skin Effect

For the induction heating process to be efficient and practical, certain relationships of the frequency of the electromagnetic field that produces the eddy currents, and the properties of the workpiece, must be satisfied. Because almost all of the heat is produced at the surface, the eddy currents flowing in a cylindrical workpiece will be most intense at the outer surface, while the currents at the center are negligible. The depth of heating depends on the frequency of the ac field, the electrical resistivity, and the relative magnetic permeability of the workpiece. The Figure shows reference depths for various materials at different temperatures. The reference depths decrease with higher frequency and increase with higher temperature. The reference depth becomes the theoretical minimum depth of heating that a given frequency will produce at a given power and workpiece temperature. For a fixed frequency, the reference depth varies with temperature because the resistivity of conductors varies with temperature. With magnetic steels the magnetic permeability varies with temperature, decreasing to a value of one (the same as free space) at the Curie temperature, at which steel becomes non-magnetic. Because the reference depth increases when steel is heated over the Curie temperature, the a/d ratio of 4 when austenitizing must be based on the reference depth when the steel is at a temperature above the Curie. The figure shows an illustration of the deeper depth of current penetration over the Curie. Because of these effects the reference depth of non-magnetic materials may vary by a factor of two or three over a wide heating range, whereas for magnetic steels it can vary by a factor of 20.

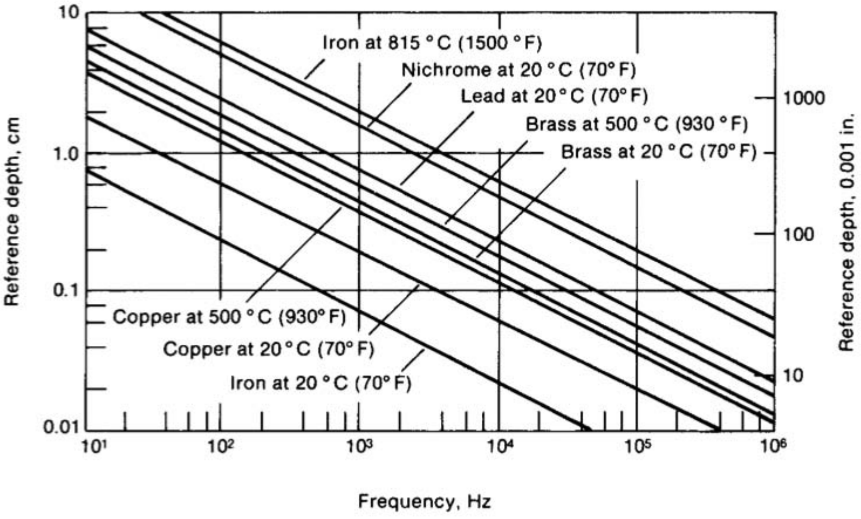

Figure 2.9: Reference depth for various materials.

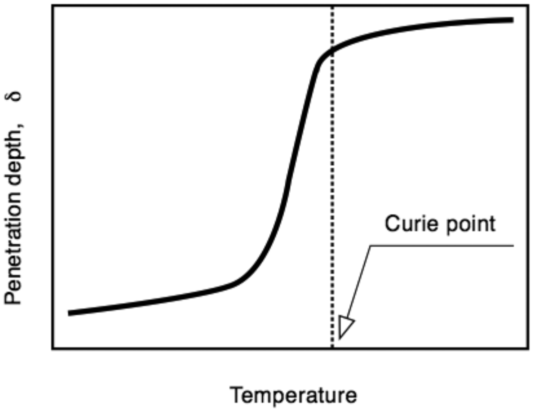

Figure 2.10: Variation of current penetration depth through Curie.

2.4 Thermic Theory

For the case of a long cylinder considered here, where the transmission of heat takes place only in the radial direction, and thermal parameters of the material constituting the cylinder are constant, the Fourier equation in cylindrical coordinates is

$$\frac{\partial \theta}{\partial t} = k\left(\frac{\partial^2 \theta}{\partial r^2} + \frac{1}{r}\frac{\partial \theta}{\partial r}\right) + \frac{w(r)}{c\gamma} \tag{2.20}$$

Now introducing the adimensional parameters

$$\tau = \frac{kt}{R^2};\ \Theta = \frac{2\pi\lambda}{P_u}\theta;$$

Pu is the power trasformed in heat in the cylinder per axyal length unit

$$P_u = 2\pi R^2 \int_0^1 \xi w(\xi) d\xi$$

And defining

$$\Psi(\xi) = \frac{w(\xi)}{\int_0^1 \xi w(\xi) d\xi} = m\frac{ber'^2(m\xi) + bei'^2(m\xi)}{ber(m)ber'(m) + bei(m)bei'(m)}$$

the Fourier equation is rewritten in the formula

$$\frac{\partial \Theta}{\partial \tau} = \frac{\partial^2 \Theta}{\partial \xi^2} + \frac{1}{\xi}\frac{\partial \Theta}{\partial \xi} + \Psi(\xi) \tag{2.21}$$

Assuming that initial temperature at all points is a zero , and that the heating occurs with no heat losses to the surface of the cylinder, the equation is solved with the following initial and boundary conditions .

$$\Theta(\xi) = 0 \; for \; \tau = 0$$

$$\frac{\partial \Theta}{\partial \xi} = 0 \; for \; \tau > 0 \; and \; \xi = 1$$

At very high frequencies, where the depth of penetration is small compared to the diameter, the heating result of surface type and the equations of the thermal transient are those known for the heating with constant heat flux to the surface of the body, with the values show in Figure

$$\Theta = 2\tau + \frac{1}{2}\xi^2 - \frac{1}{4} - 2\sum_{n=1}^{\infty} \frac{J_0(\beta_n \xi)}{\beta_n^2 J_0(\beta_n)} e^{-\beta_n \tau} \tag{2.22}$$

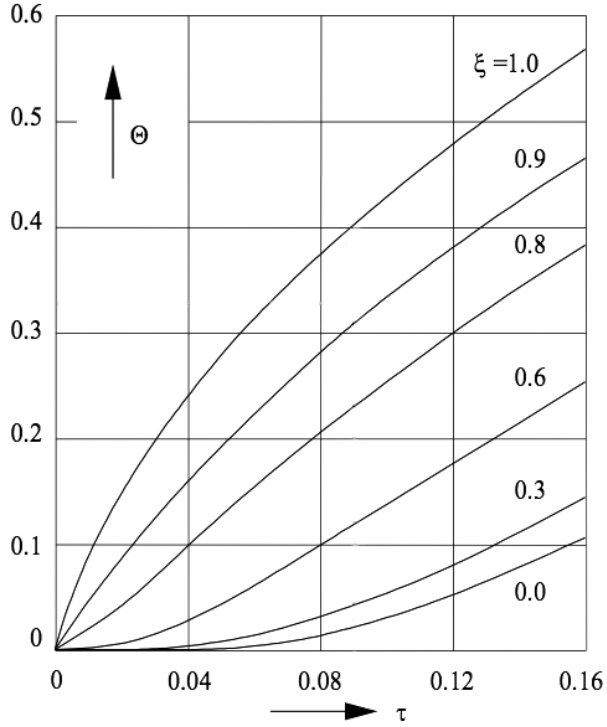

Figure 2.11: Thermal transient for high values of m

2.5 Induction Hardening

The surface hardening is the most interesting application of induction heating: with the hardening of a surface layer is possible to obtained very different proprieties from the ones in the core. This is achieved with a heat treatment consisting essentially of the heating of the material to a temperature above the critical one, and a permanence at this temperature for a time sufficient to obtain the structural balance of the affected areas, and a subsequent rapid cooling to fix the structure at high temperatures. There are no general rules that allow to establish the optimal distribution of induced currents in the body to be treated. Values indicative of the thickess of quenching, and the corresponding values of specific power and heating times which allow to obtain them, can be determined analytically even assuming the material characteristics unchanged during heating. From

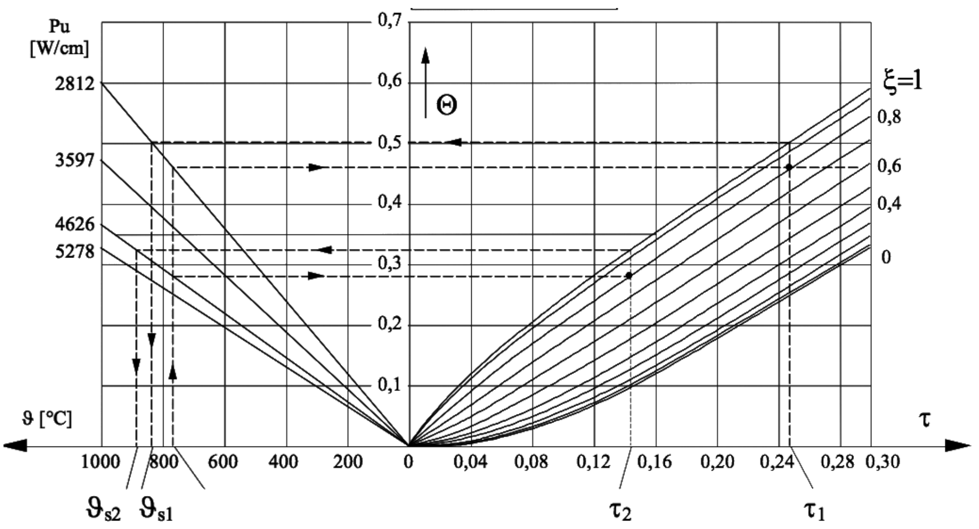

Figure 2.12: Diagram for the determination of the radial distribution of temperature at the end of the transient heating [Steel C45, m=3, D=25mm]

this diagram, knowing the thickness to be quenched and the temperature Ac3, is possible to determine the radial distribution of temperature at the end of the transient heating, and the corresponding surface temperature and the time and power required. In particular, the diagrams reveal that the same hardened depth can be obtained with several pairs of values time-power and so with different temperature distributions along the radius at the end of heating. In fact, in the first instants of the cooling, the temperature gradients are such as to give rise to a transmission of heat to the inner layers of the body subjected to treatment and then to a thickness of tempering higher than those evaluable at the end of heating.

2.6 Complex geometries: Gears

A typical example of hardening of bodies geometrically complex is that of simultaneous hardening of the gear, to obtain a thickness hardened uniform along the entire periphery of the workpiece, so in correspondence of both the tip of the tooth, both on the bottom of the root. In this case the choice of the frequency are of fundamental importance not only considerations of electrical type, but also thermal. Reliability and high dimensional accuracy (to ensure good fit) are among the requirements for gears. Keeping distortion as low as possible during heat treatment is most important. Induction heat treating is one of the very important processes used for heat treatment of gears. Gears, because of the wide varieties, sizes, and differences in tooth profiles, represent unique applications. External spur and helical gears, bevel and worm gears, internal gears, racks, and sprockets are good examples of the kinds of gears of which the size can range from less than 6 mm (0.25 in.) to greater than 3 m (12 feet). As with shafts, the hardened pattern may be through the cross section, as with small armature shafts, to single-teeth case hardening, as is done with large gears. A wide variety of frequencies and induction processes are used, because of the way the induced currents are produced in gear teeth with different profiles, sizes, and pitches. The heat treating processes use single-shot heating techniques and a variety of scanning techniques. A wide number of different frequencies are used to accommodate the different patterns and tooth profiles. The size of gear, the hardening requirements, and the production requirement influence the type of induction-hardening process used. High quantity production lots can be induction hardened single shot, whereas small quantities of large gears need to be run one tooth at a time to keep the capital equipment costs low. From the electrical point of view, a good trasfert of energy between inductor and body to be hardened is required that the parameter m never drops below 2-2.5 and that the choice of frequency is related to the thickness of quenching desired, so the choice of a single frequency appears to be a compromise solution . Assuming that each tooth could be replaced by a cylinder of radius R1 and consider the main body of the gear as a bigger cylinder of radius R2, it appears evidente that would be theoretically necesary two differente frequency. Using this approximation we can obtain the following curves, in which are put in correlation the power values on the workpiece, the heating times and the

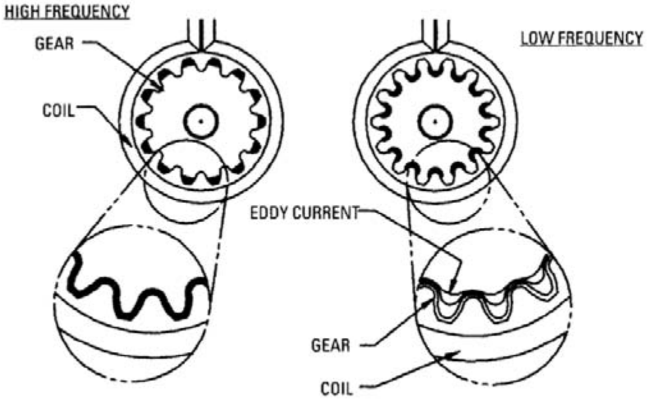

Figure 2.13: Dual Frequency Effect on Gear

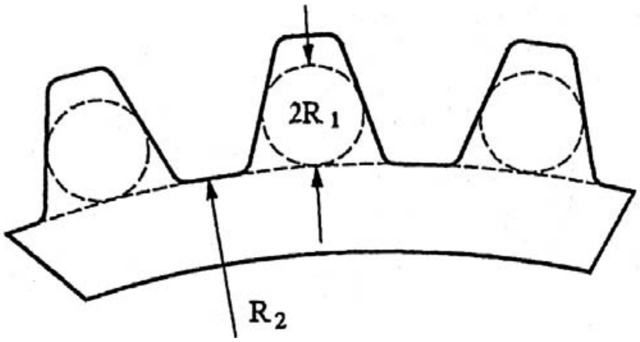

Figure 2.14: Modelization of Gear

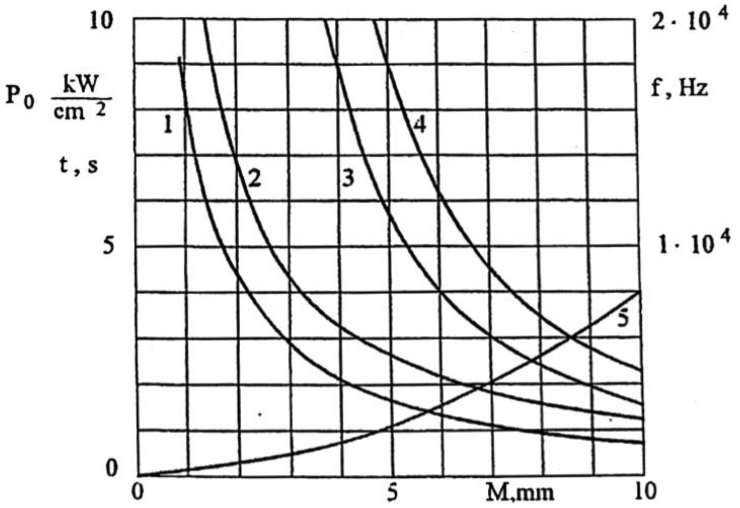

Figure 2.15: Parameters for the simultaneous hardening of gears module M [1-specific power into gear and 2-specific power output of the generator; 3-4 - Frequency; 5-heating time]

frequency. Unfortunately, these approximations entails to an incorrect prediction of the real behavior of the piece subjected to the process. For this reason is more useful using numerical methods such as finite element method (FEM).

3 Power Supply

3.1 Types of Power Supplies

There are many different types of induction heating power sources, ranging from line frequency coils, to heat for shrink fitting, to many different types of induction power supplies. Most induction power supplies sold for heat treating today are either some type of solid state or oscillator (vacuum) tube. The power supplies are basically frequency changers that change the 50 Hz, three-phase current furnished by the electric utility into a higher-frequency, single-phase current for induction heating. These power supplies are often referred to as converters, inverters, or oscillators, depending on the circuits and electronic devices used, with many possible combinations of conversion techniques.

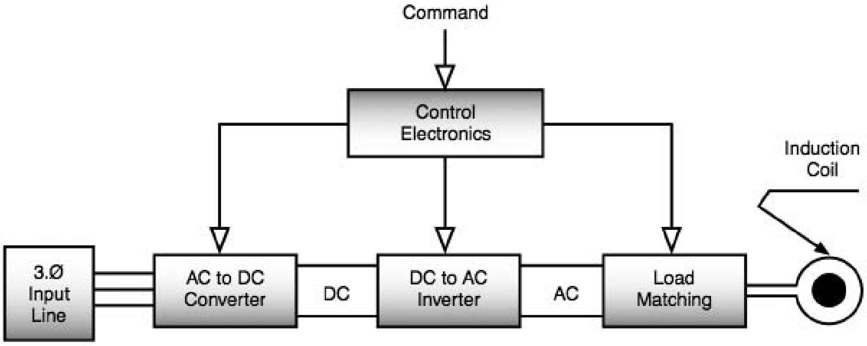

Figure 3.1: Induction heat treat power supply basic diagram.

Solid-state power supplies convert the line alternating voltage (ac) to produce single-phase, direct-current (dc) voltage. Inversion is then accomplished through using thyristors (silicon controlled rectifiers, or SCRs), or transistors such as isolated gate bipolar transistors (IGBTs) or metal- silicon-dioxide field-effect transistors (MOS FETs), to produce dc pulses that are then made sinusoidal to form high frequency, ac. (Some current source power supplies do this in one step.) Radio frequency (RF) (oscillator or vacuum tube) power supplies use a transformer to change the input voltage to high voltage before conversion to dc.

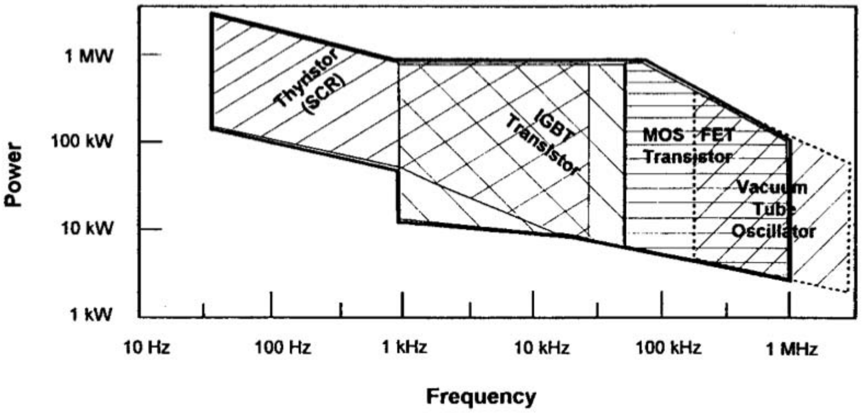

Figure 3.2: Modern inverter power types for heat treating

One of the most common topologies of resonant power supplies is the series resonant converter. The circuit utilises a simple resonant tank and, when operated slightly above resonance, can offer zero voltage switching (ZVS) for the MOSFETs. Since the maximum device voltage is clamped to the supply voltage, lower voltage MOSFETs with a smaller channel resistance can be used, limiting the conduction losses. The operating frequency can be a significant fraction of a megahertz . However, the MOSFETs have to commutate all of the current in the work piece which, in the absence of an impedance matching transformer, can be in the order of kiloamperes. The alternative is to use a parallel resonant tank in a current-fed inverter configuration. The current commutated by the transistors is comparatively small, and the conduction losses are kept under control, but the switches are exposed to the peak resonant voltage which may be much larger than the supply voltage. The problem is exacerbated for applications requiring high-frequency operation, where the quality factor of the parallel resonant tank can be very large. IGBTs are usually employed, as they can block much larger voltages than MOSFETs. However, the maximum operating frequency of these devices is well below that achievable with MOSFETs.

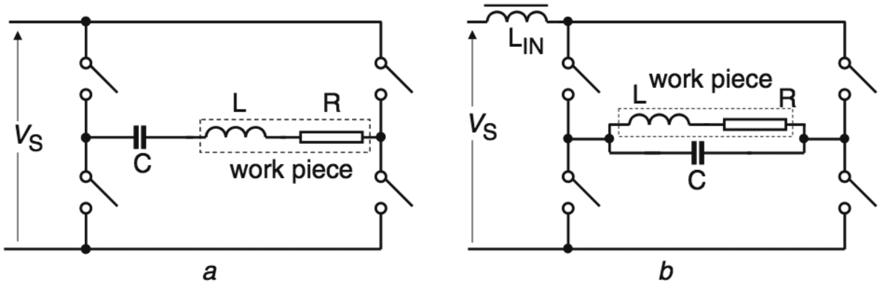

Figure 3.3: Conventional resonant inverters for induction heating [a) Voltage-fed series resonant inverter; b) Current-fed parallel resonant inverter]

3.2 Voltage-fed series resonant inverters

In series resonant tanks, the inductor is connected in series with the capacitor. In this case, the tank behaves as a current source and the inverter used is a voltage-fed inverter, which means that the inverter is fed with a constant voltage source. This implies that the inverter is fed by a capacitor with a high capacitance value that maintains the voltage constant. In most applications above 5 kW, the inverter used is the H-bridge, as shown in figure. This topology is used because allows transmitting the same power with less current for a given voltage Ue . In voltage-fed inverters, two switches of the same inverter leg cannot be turned-on at the same time, otherwise short-circuit occurs. The time be- tween the turning-off of one of these switches and the turning on of the other is called dead-time. In this topology, antiparallel diodes are necessary to allow inductor's current conduction when the opposite switches are turned-off.

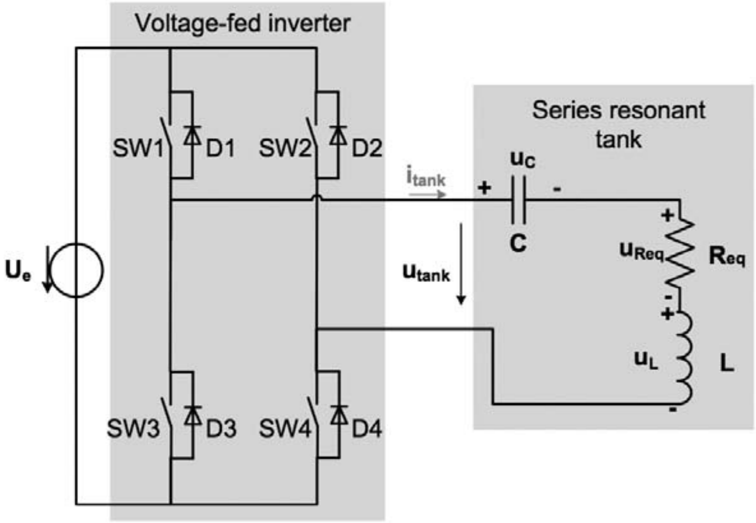

Figure 3.4: Voltage-Fed Series Resonant Inverter

3.2.1 Resonant frequency

Observing the RLC circuit of a VFSRI, the following equation is accomplished

$$u_{tank} = u_{Req} + u_L + u_C = R_{eq} i_{tank} + L\frac{\partial i_{tank}}{\partial t} + \frac{1}{C}\int i_{tank} dt \tag{3.1}$$

Using Laplace transformation with initial condition equal to zero let's obtain the following second order system with a zero

$$H_s(s) = \frac{I_{tank}(s)}{U_{tank}(s)} = \frac{sC}{s^2LC + sCR_{eq} + 1} = sC\frac{\omega_n^2}{s^2 + 2\zeta\omega_n s + \omega_n^2} \tag{3.2}$$

The roots of this second order system are

$$s_1, s_2 = -\zeta\omega_n \pm j\omega_n\sqrt{1-\zeta^2} \tag{3.3}$$

where

- ω_n is the undamped natural frequency of the system,

$$\omega_n = \frac{1}{\sqrt{LC}}$$

- ζ is the damping ratio,

$$\zeta = \frac{R_{eq}}{2}\sqrt{\frac{C}{L}}$$

Resolving the equation in the frequency domain, the resonance frequency coincide with the undamped frequency of the system,

$$\omega_r = \frac{1}{\sqrt{LC}} \tag{3.4}$$

and the transfer function at this frequency is equal to

$$H_s(\omega_r) = \frac{I_{tank}(\omega_r)}{U_{tank}(\omega_r)} = \frac{1}{R_{eq}} \tag{3.5}$$

3.2.2 Quality factor

Considering that the converter is commutating at resonant frequency, the quality factor is equal to

$$Q = \frac{\omega_r L}{R_{eq}} = \frac{1}{\omega_r C R_{eq}} \tag{3.6}$$

Combining this equation with the definition of damping ratio and knowing that the resonant and the natural frequency are equal for the series tanks, the following equation is accomplished

$$Q = \frac{1}{2\zeta} \tag{3.7}$$

3.2.3 Power in the workpiece

With regard to the power transmitted to the workpiece, it can be easily calculated considering that Req represents the workpiece resistance

$$P = I_{tank}^2 R_{eq} = \frac{U_{eq}^2}{R_{eq}} \tag{3.8}$$

Bearing in mind that the power is maximum when the current is maxi- mum, the power is maximum at resonant frequency . Considering that the voltage across the resistance is equal to the first harmonic of u_{tank} , then

$$P(\omega_r) = \frac{(U_{R_{eq}(\omega_r)})^2}{R_{eq}} = \frac{(\frac{4U_e}{\sqrt{2}\pi})^2}{R_{eq}} = \frac{8U_e^2}{\pi^2 R_{eq}} \tag{3.9}$$

It is observed from this equation, that the power delivered to the workpiece can be controlled by the voltage of the voltage-source Ue. This is the most intuitive power control method.

3.3 Current-fed parallel resonant inverters

In case of parallel tanks, the inductor is connected in parallel with the ca- pacitor. Contrarily to a series connection, the tank behaves like a voltage source and the inverters used are current-fed. This implies that the inverter is fed with a high inductance that maintains the current and behaves as a constant current source. A parallel tank and an ideal CFPRI are shown in figure. In case of current-fed inverters, the current path cannot be opened and switches from the same inverter leg have to overlap. Switches have to be unidirectional in current but bidirectional in voltage. If diodes are not added, the capacitor would discharge.

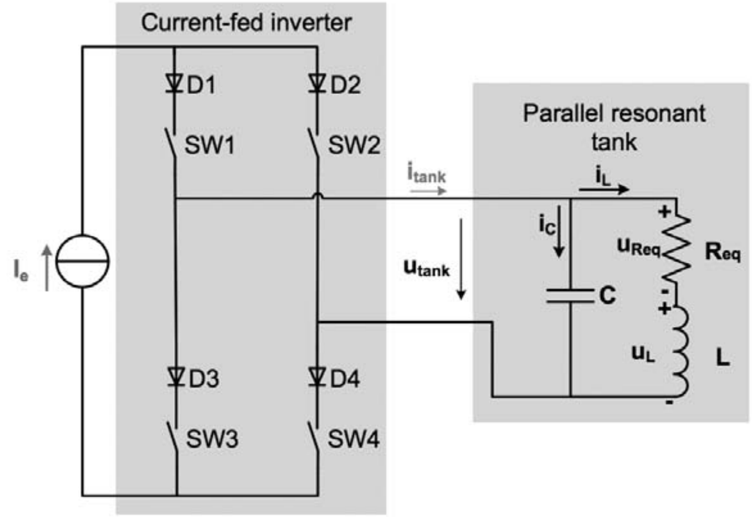

Figure 3.5: Current-fer parallel resonant inverter

3.3.1 Resonant frequency

Proceeding like in VFSRI but for CFPRI, the RLC circuit in figure accomplishes the following equations

$$i_{tank} = i_C + i_L \tag{3.10}$$

$$i_C = C\frac{du_{tank}}{dt} \tag{3.11}$$

$$i_L = \frac{1}{L}\int u_L dt \tag{3.12}$$

$$u_{tank} = u_L + u_{R_{eq}} \tag{3.13}$$

Using Laplace transformation with initial conditions equal to zero, and obtaining the next second order system with a zero

$$H_p(s) = \frac{U_{tank}(s)}{I_{tank}(s)} = \frac{sL + R_{eq}}{s^2LC + sCR_{eq} + 1} = (sL + R_{eq})\frac{\omega_n^2}{s^2 + 2\zeta\omega_n s + \omega_n^2} \tag{3.14}$$

The roots of this second order system are the same than those found for VFSRI . In this case, the same definitions of undamped natural frequency ωn and damping ratio ζ shown are used. Assuming the definition of resonant frequency as the maximum of a transfer function, the mathematical expression is more complex for CFPRI than for VFSRI. Proceeding similarly and calculating the maximum with the help of mathematical softwares, the maximum of Hp(s) is

$$\omega_r = \frac{\sqrt{C\sqrt{2LCR_{eq}^2 + L^2} - C^2R_{eq}^2}}{LC} \tag{3.15}$$

considering the definition of quality factor for the series model of the inductance- workpiece system

$$\omega_r = \omega_n = \sqrt{\sqrt{\frac{2}{Q^2} + 1} - \frac{1}{Q^2}} \tag{3.16}$$

where for high values of Q, so for most of the time, $\omega_r = \omega_n$, like in the case of VFSRI.

3.3.2 Power in the workpiece

Considering that the current in the inductance is the same as in the equivalent resistance, the power transmitted to the workpiece is equal to

$$P = I_L^2 R_{eq} \tag{3.17}$$

Assuming a high Q value, the power at resonant frequency is

$$P(\omega_r) = I_L(\omega_r)^2 R_{eq} \approx (QI_{tank}(\omega_n))^2 R_{eq} \approx (Q\frac{4I_e}{\sqrt{2}\pi})^2 R_{eq} = \frac{8I_e^2 Q^2 R_{eq}}{\pi^2} \tag{3.18}$$

In this case, the power delivered to the wokpiece can be controlled with the current source Ie.

3.4 Regulation

The ability to produce the same amount of power for each part during the heating cycle is important. The power supplies need to have regulation for two reasons. The first is so that the power supply has constant output if there is a change of the line voltage during operation (not an unusual circum- stance). The manufacturers normally rate their power supply over the range of input voltage for which constant output can be produced. However, if the power supplies are being run at full power, regulation may not be achieved over large voltage swings, such as the line voltage ranging from 480 V down to 430 V in the same day. Solid- state power supplies regulate to constant output through closed-loop controls to hold constant power, constant voltage, or constant current. The firing rate of the semiconductors is changed to cause a frequency shift so that the constant output is maintained. Each method of regulation of solid-state has areas of application. When the controls are set to hold constant power, there is no drop of power during heating. Voltage and current regulation tend to the output power better when there are wide variations in impedance during the heating cycle, such as when a scanner passes over different diameters of a workpiece when heating.

4 Induction Coils

The coil, also known as inductor, is basically a transformer primary that induces high-frequency output of an induction power supply into a workpiece, which is effectively the transformer secondary. Longitudinal flux (reverse current flow) induction coils are by far the most widely used type of coil, with solenoid types of coils most commonly used. Longitudinal flux coils should not be confused with channel coils, which are orientated in the longitudinal direction of a workpiece. The workpiece is surrounded or enveloped, with the turns on opposite sides so that induced current flows around the workpiece. When the air gap between the coil and workpiece is reasonable for the frequency and load conditions involved, heating can be quite efficient because the flux lines tend to be confined. The coils can be oriented so that long workpieces are either encircled by a solenoid coil with the current flowing around the circumference of the part, or, in the case of channel coils, oriented perpendicular to the workpiece so that the current flows along the longitudinal direction. Factors that influence coil design and selection include the dimensions and shape of the workpiece, number of workpieces to be heated, hardness pattern desired, production process to be used (such as single shot or scanning), frequency and power input, how the workpiece is to be quenched, and coil-life considerations.

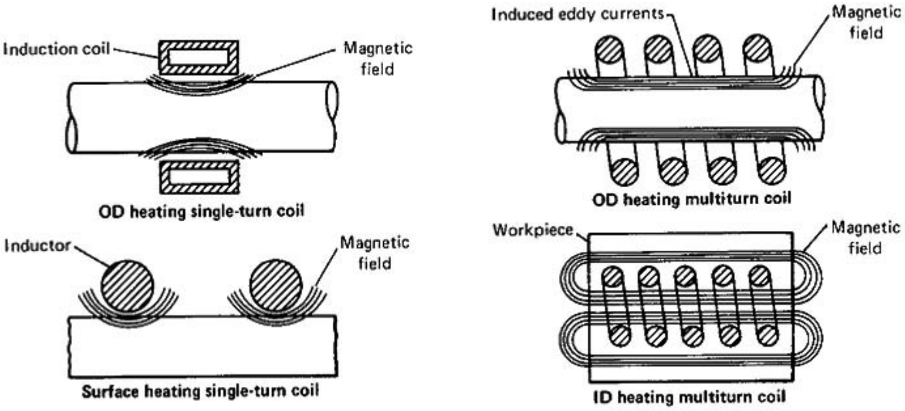
Induction coil
Magnetic field
OD heating single-turn coil
Induced eddy currents
Magnetic field
OD heating multiturn coil
Inductor
Magnetic field
Surface heating single-turn coil
Workpiece
Magnetic field
ID heating multiturn coil

Figure 4.1: Typology of Coils

4.1 Magnetic Flux Concentrator

Magnetic flux concentrators or intensifiers are used very effectively to increase the efficiency of some coils. In other cases, flux concentrators are necessary to produce the pattern required in the workpiece. Because of proximity effect, a significant part of the conductor's current flows near the surface of the conductor that faces the workpiece. The remainder of the current is concentrated on the sides of the conductor with a current induced in a

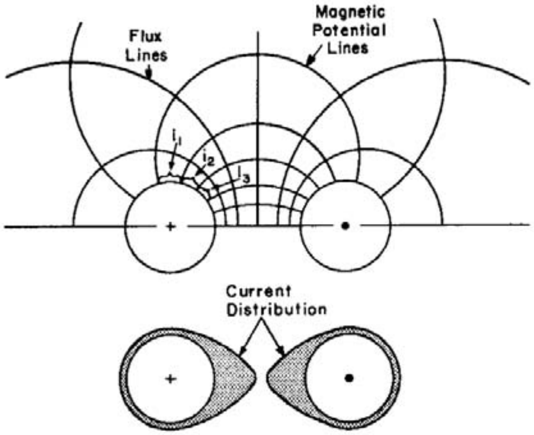
Flux Lines
Magnetic Potential Lines
i_1
i_2
i_3
Current Distribution

Figure 4.2: Flux plot of two parallel conductors carrying current in opposite directions.

general area in the workpiece close to the conductor. Correctly applied, the benefits are:

- Reduction of operating power levels required to obtain the desired heating of workpieces
- Improvement of process efficiency and decrease in the amount of energy used

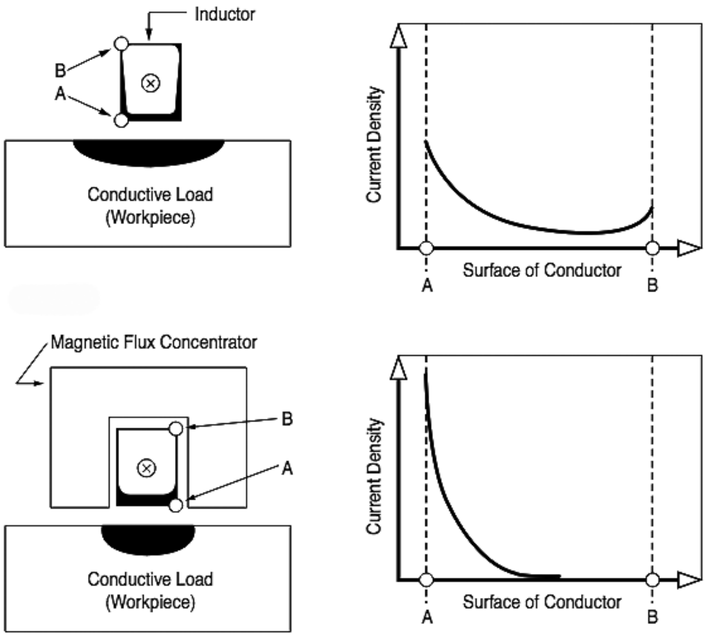
Inductor
B
A
Conductive Load (Workpiece)
Current Density
Surface of Conductor
A
B
Magnetic Flux Concentrator
B
A
Conductive Load (Workpiece)
Current Density
Surface of Conductor
A
B

Figure 4.3: Current distribution in straight conductor

4.2 Coil Characteristics Versus Frequency

Coils in the lower frequencies of 1 to 10 kHz can have mechanical vibration that requires rigid restraint and mounting techniques, particularly in the 1 kHz region. Close space multi-turn coils will spread apart when power is applied unless they are restrained. These lower frequencies are used for deeper case hardening and for larger diameter through heating applications. The coils used for heat treating in the 3 to 25 kHz frequency range tend to be low-turn coils, although coils used for continuous heating of bars and tubes can use multi-turn coils such as those used in the forging industry. Machined coils are more likely to be used with the low frequencies, while coils made from tubing are more likely to be used with high frequencies. High frequency has higher edge effect, which is an effect in which there is more current concentration at the end of a bar that produces deeper heating. This can affect coil selection from the viewpoint that the higher frequencies are more limited in the use of wide or multi-turn coils in scanning operations due to this edge effect tendency. The figure shows the effect of coil placement at various locations, both on the outside diameter (OD) and inside diameter (ID) of round parts. The position and overlap of the coil affects the heating effect at the edges. Coils are designed with overlap and then positioned so that the heating at the edge produces the same depth of pattern as produced in the center. The lower the frequency, the more overlap is required because of the edge-heating effect.

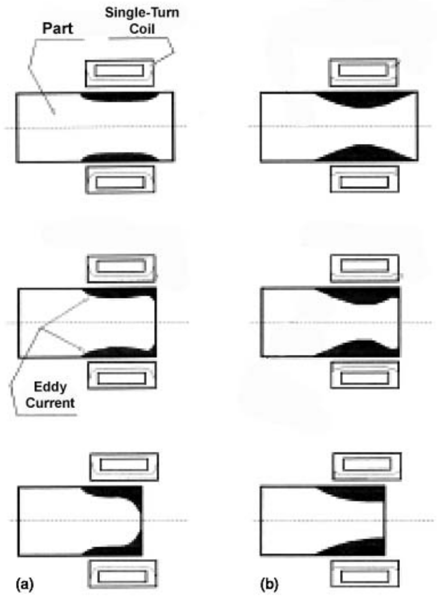

Figure 4.4: Electromagnetic end effect for: a) high and b) low frequency

5 Finite Element Method on 2D Gear

In mathematics, finite element method (FEM) is a numerical technique for finding approximate solutions to boundary value problems. It uses variational methods (the calculus of variations) to minimize an error function and produce a stable solution. Analogous to the idea that connecting many tiny straight lines can approximate a larger circle, FEM encompasses all the methods for connecting many simple element equations over many small subdomains, named finite elements, to approximate a more complex equation over a larger domain. In general in finite element discretization we have that the area of study is subdivided into non-overlapping finite elements. The sides of finite elements intersect at nodes. Since analitical solution is almost impossible to obtain in complex geometries like gears, let's use this method to determine the distribution of quantities in the piece.

5.1 Formulation

For the 2D formulation the magnetic field H is always perpendicular to the plane, and the current density parallel.

$$\bar{E} = (E_x(x,y), E_y(x,y), 0)$$

$$\bar{J} = (J_x(x,y), Jy(x,y), 0)$$

$$\bar{B} = (0, 0, B_z(x,y))$$

$$\bar{H} = (0, 0, H_z(x,y))$$

Now lets introduce the electric vector potential T, for which

$$\bar{J} = \nabla \times \bar{T}$$

So T is perpendicular to the plane, like H, in fact

$$T = T_0 + H + \nabla\phi = H \tag{5.1}$$

The harmonic first Maxwell differential equation is

$$\nabla \times \bar{E} = -j\omega\mu\bar{H} \tag{5.2}$$

From the first part

$$\nabla \times \bar{E} = \nabla \times \rho\bar{J} = \nabla \times \rho\nabla \times \bar{T} \tag{5.3}$$

And from the other part

$$-j\omega\mu\bar{H} = -j\omega\mu\bar{T} \tag{5.4}$$

So the general formulation becomes

$$\nabla \times \rho \nabla \times \bar{T} - j\omega\mu\bar{T} = 0 \tag{5.5}$$

But if T is only perpendicular to the plane, is possible to substitute it with the scalar quantity H

$$\nabla \times \rho \nabla \times H_z - j\omega\mu H_z = 0 \tag{5.6}$$

5.2 Weigthed Residual Method

The weigthed residual method is the way to solve this DAE (Differential Algebric Equation) . It is based on solving this kind of equation:

$$\int\limits_{\Omega} w\mathcal{L}(V)d\Omega = 0 \tag{5.7}$$

This equation is also true for an approximate solution where the potential v is the sum of the calculated potential in some points in the space multiply by the so called shape function: these are linear functions that defy the intermediate values of potential in the space between the calculated points.

$$\tilde{V} = \sum_i N_i V_i \tag{5.8}$$

$$\int\limits_{\Omega} N_i \mathcal{L}(\tilde{V})d\Omega = 0 \tag{5.9}$$

For the Galërkin method lets substitute the weigthed function w with the shape function Ni, so substituting this equation instead of L

$$-\int\limits_{\Omega} \rho \nabla N_i \cdot \nabla \left(\sum_j H_j N_j \right) d\Omega + j\omega \int\limits_{\Omega} \mu N_i \left(\sum_j H_j N_j \right) d\Omega = 0 \tag{5.10}$$

After some simple passages

$$-\sum_j V_j \int\limits_{\Omega} \rho \nabla N_i \nabla N_j d\Omega + j\omega \sum_j V_j \int\limits_{\Omega} \mu N_i N_j d\Omega = 0 \tag{5.11}$$

In matrix way, introducing Stiffness matrix K and Mass matrix M :

$$[[K] + j\omega\,[M]]\,[H_z] = [f] \tag{5.12}$$

5.3 Building Stiffness Matrix K and Mass Matrix M

The Stiffness matrix K is the discrete equivalent of " $\nabla \times \rho \nabla$ " . In order to build it, must be computed its coefficients k. Let's assume to choose i and j as it's represented in the figure. The following integral calculate the wanted value

$$k_{ij} = \int\limits_{\Omega} \rho \nabla N_i \nabla N_j d\Omega \tag{5.13}$$

It's possible to write the integral on Ω as the sum of the integral computed in each triangular element ΔKi.

$$k_{ij} = \sum_{k=1} \int\limits_{\Delta k_k} \rho \nabla N_i \nabla N_j d\Omega \tag{5.14}$$

Only the integral on the elements which belong both to the support areas of i and j are not equal to zero, while in the other elements Ni or Nj is zero as they are computed out of their support area. It's easy to understand that K matrix is very sparse, the more sparse the more nodes there are in Ω, because the number of non-zero coefficient is more or less constant. As $\nabla N_i \nabla N_j = \nabla N_j \nabla N_i$, we get $k_{ij} = k_{ji}$ and so K matrix is also symmetric (before adding boundary conditions).

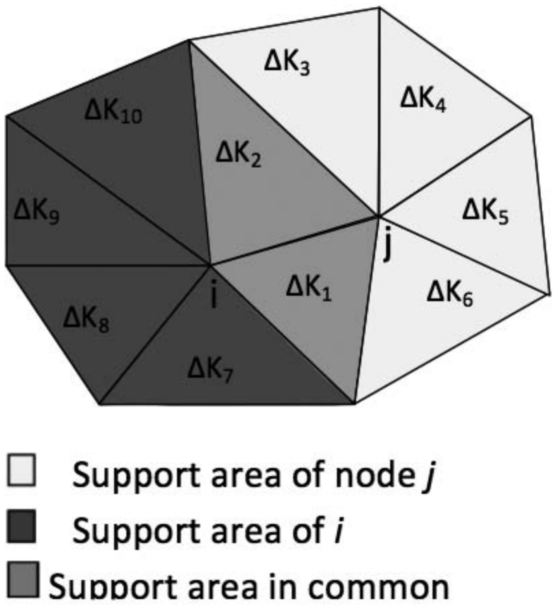

Figure 5.1: Subdivision of space in finite elements

For each triangular element, the shape function can be written as a polynomial (first order shape function), so the gradient will be a costant. To build the Stiffness Matrix we need to calculate in every element the value of the integral in every local node, and update the value of the integral in the node. In very similar way we can build also the Mass Matrix.

5.4 Boundary Conditions

As in Finite Differences Method, the solution of the simple system studied up to now is a zero vector potentials, because any boundary conditions are imposed. The matrix K depends only from geometry, materials and the mesh: the way to impose the Dirichlet Boundary Conditions is very simple. In matrix K lets put all the elements in the row corresponding to the nodes in the boundary equal to zero, except the one in the diagonal, which is equal to 1. In known-potential vector there are, corresponding to the boundary nodes, the values of known potentials f.

5.5 Meshing

The first thing to do when it's known the dimensions of the gear, is to create the mesh. The geometry could be simplify considering only one tooth of the gear. Then is possible to divide in two parts the tooth, using the central symmetry. The element length varies from a minimum determined by the skin effect, to a maximum with a relaxation ratio that lets get a ligther mesh.

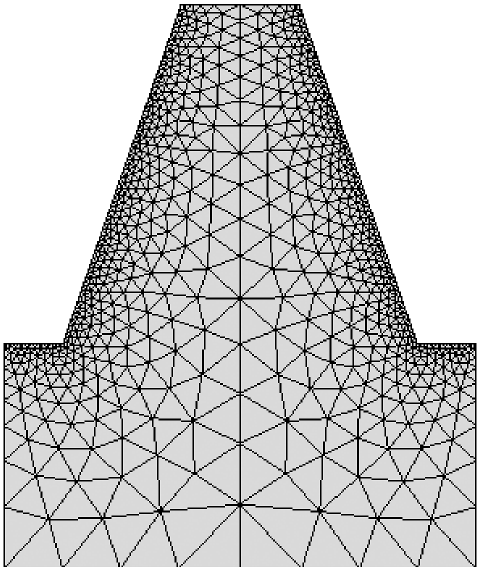

Figure 5.2: Mesh of Tooth of Gear

5.6 Results

5.6.1 Magnetic Field H

Once resolved the system indicated before, it's possible to represent the distribution of H field on the piece. We can see how is strongly affected from the Frequency: in MF the field penetrate in all the tooth, instead in HF the field is concentrate in a thin superficial layer.

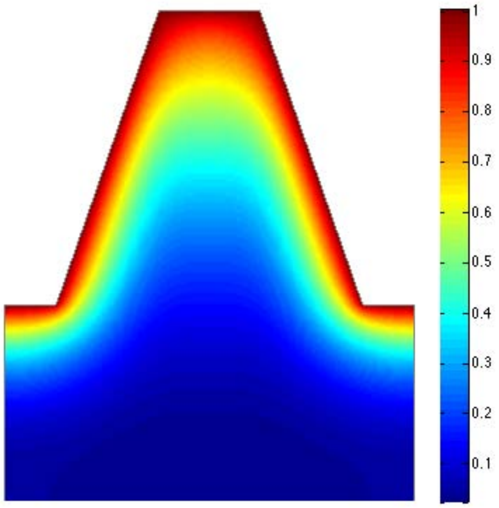

Figure 5.3: Distribution of H/H0 at 10kHz

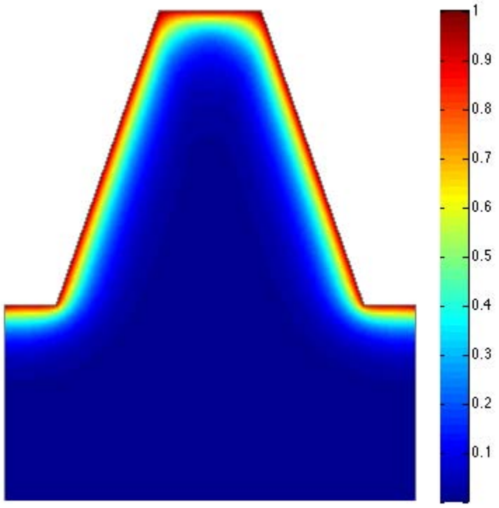

Figure 5.4: Distribution of H/H0 at 100kHz

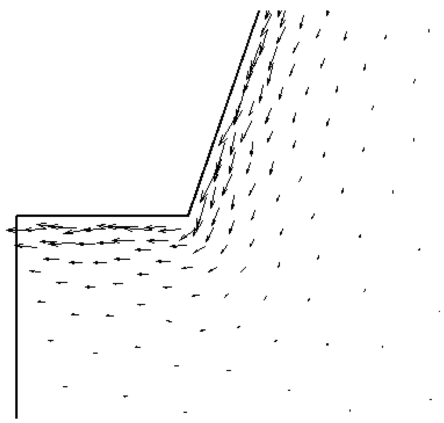

Figure 5.5: Current Density Distribution on the root at 10 kHz

5.6.2 Current Density J

From previous formulation it's possible to calculate the current density, $J = \nabla \times H$. The curl in a 2D problem with the potential vector perpenticular to the plane is simply the gradient vector rotate of 90°, so the components of the vector J are

$$\bar{J} = \left(\frac{\partial H_z}{\partial y}; -\frac{\partial H_z}{\partial x}; 0 \right) \tag{5.15}$$

The derivates of the vector H are automatically determined in the building of the stiffness matrix K, so it's easy to calculate the value of the current density in every point of domain.

Part II

Simulation

Introduction

In this little section is rapresented the workflow followed in the analisys of the simulations and tests done.

- First simulations were performed with simple geometry (cylinder) in order to identify the best parameters can be used to represent as closely as possible the material.
- Subsequently was analyzed more complex geometry already tested previously, focusing in the differences between linear models (magnetic permeability as a function only of temperature) and nonlinear (magnetic permeability as a function of both temperature and magnetic field).
- Done the appropriate considerations in the simulations, the tests were performed first with simple geometry, comparing the two modes of operation of the machine, and identifying the most suitable for a comparison with numerical simulations.
- Finally, tests were carried out with complex geometry to go and compare the results obtained with the complete model studied with simulations.

6 Material Properties: AISI 4340

AISI 4340 is a heat treatable alloy steel, containing little quantities of nickel, chromium and molybdenum. It is known for its toughness and capability of developing high strength in the heat treated condition while retaining good fatigue strength. Typical applications are for structural use, such as aircraft landing gear, power transmission gears and shafts and other structural parts.

Element	%
Carbon	0.38 - 0.43
Chromium	0.7 - 0.9
Manganese	0.6 - 0.8
Molybdenum	1.65 - 2
Nickel	1.65 - 2
Phosphorus	0.035 max
Silicon	0.15 - 0.3
Sulphur	0.04 max
Iron	Balance

Table 6.1: Composition of AISI 4340

To introduce this material in the simulations, we must define some typical electric and thermic parameters that caracterize the material.

6.1 Electric Resistivity

Common feature of all metals, the resistivity increase in funcion of Temperature, with approximately costant slope, and with a flection in proximity of Ac1 temperature, where it decreases the growing rate. Generally it could be described by an analitic linear relation which doesn't take into account the saturazion in proxymity of the Ac1 temperature. In the image there is the measured values of resistivity in function of temperature.

6.2 Relative Magnetic Permeability

The ferromagnetic material has the propriety of conducting in good way the magnetic fields, but it has a saturation value beyond that it's not able to conduct more very well. While in non magnetic materials is equal to 1, in magnetic material it starts from the value of the permeability at 20°C , varies a little increasing temperature, then collapses to unit value reaching the Curie temperature of the material, becoming diamagnetic.

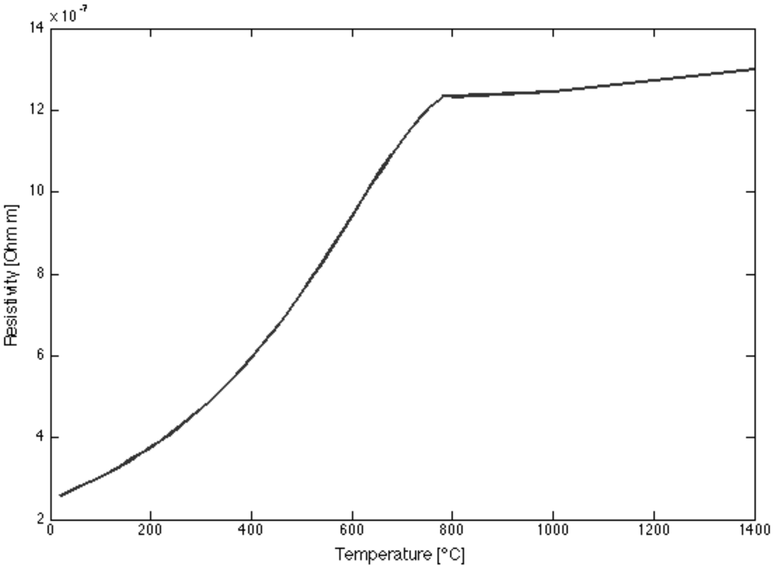

Figure 6.1: Resistivity in function of Temperature

6.3 Volumetric Heat Capacity

The heat capacity of a material is the heat quantity necessary to raise its temperature by one Celsius degree. In other words, it is a quantity that permits to evaluate the amount of heat exchanged by a body during a process characterized by a temperature variation. The so-called volumetric heat capacity (i.e., specific heat capacity per unit volume) is particularly important as it allows to take the energy of phase transition into account.

γC_{p0}[J/m^3°C]	γC_{pi}[J/m^3°C]	En[J/m^3]	σ_{dev}[°C]	τ[°C]	T_γ[°C]
3.6E6	4.7E6	850E6	100	300	870

Table 6.2: Tipical Values of Heat Capacity

With these values we can plot the curve of Volumetric Capacity in function of temperature. Specific heat of steel increases linearly with temperature until the temperature of the beginning of austenitization (Ac1), then increase until the peak, and finally decrease in proxymity of the end of austenitization (Ac3). This curve is obtained in steady state condition, se doesn't rapresent correctly the behaviour of the fast induction hardening process. As we can see in Chapter 1, the temperatures Ac1 and Ac3 varies in function of the heating velocity, and generally the are shifted to higher values. So it will be necessary to modify the values of σ_{dev} and T_γ.

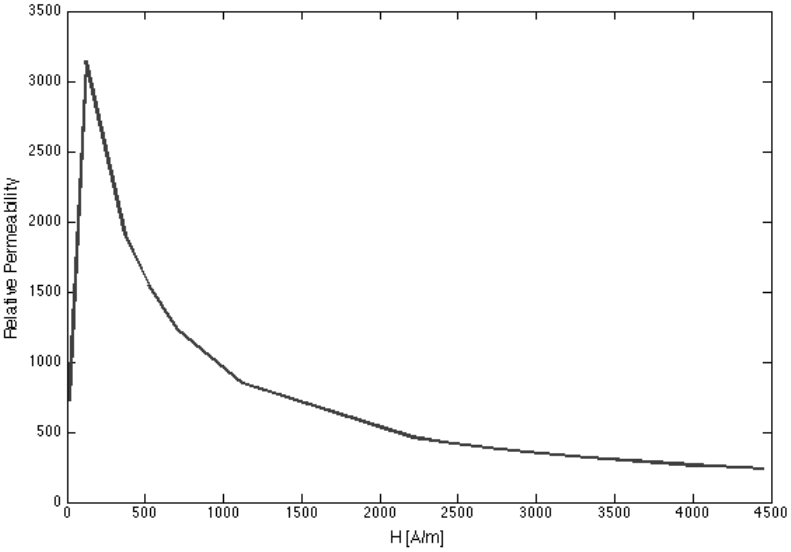

Figure 6.2: Relative Permeability in function of field H

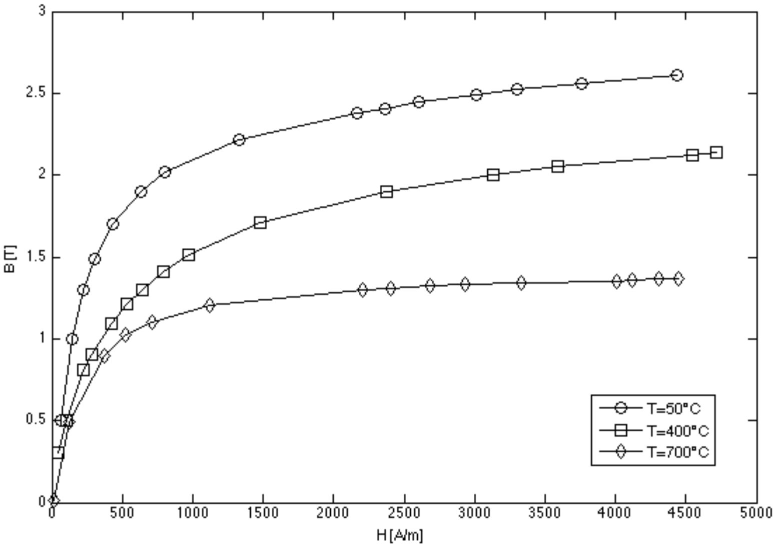

Figure 6.3: B-H Curves in function of Temperature

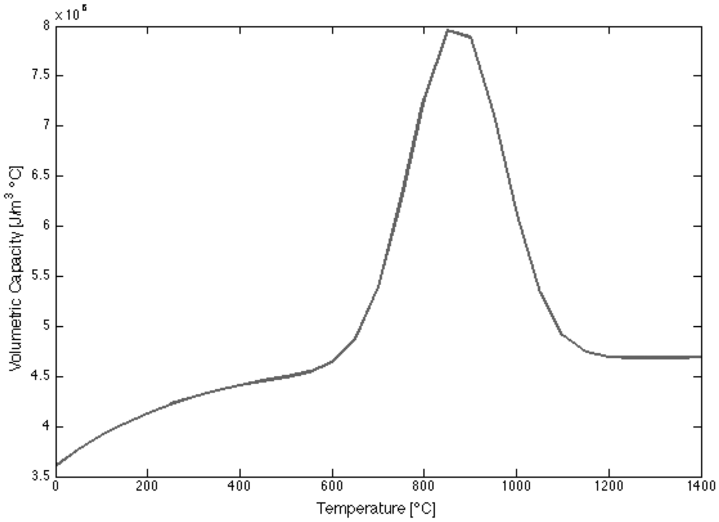

Figure 6.4: Volumetric Heat Capacity in function of Temperature

6.4 Thermic Conductivity

Thermal conductivity defines the heat flow is transmitted by conduction in the materials in function of time. In the case of induction hardening of gears we have to remember that steel has rather high thermal conductivity, so heat generated in a thin region in the surface is rapidly transferred to the cold heart of the piece and hence, it becomes difficult to control heat generated in the surface. It doesn't varies so much depending from temperature, in fact most of the time it is considered costant.

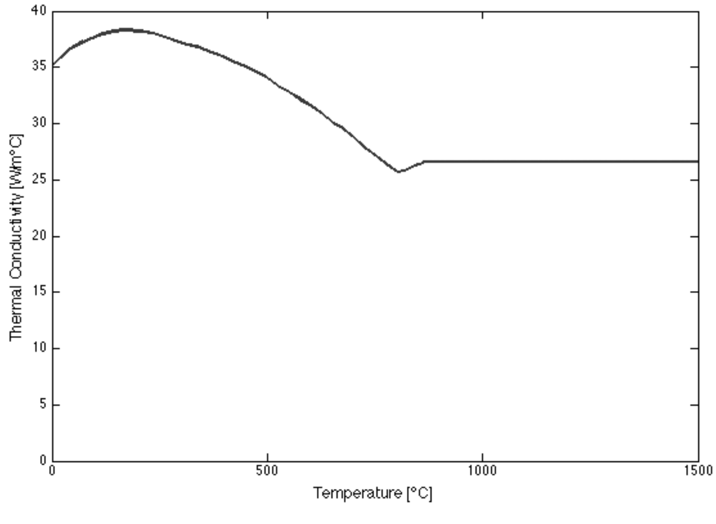

Figure 6.5: Thermal Conductivity in function of Temperature

7 Modelization of Induction Hardening on Cyinder

7.1 Geometry

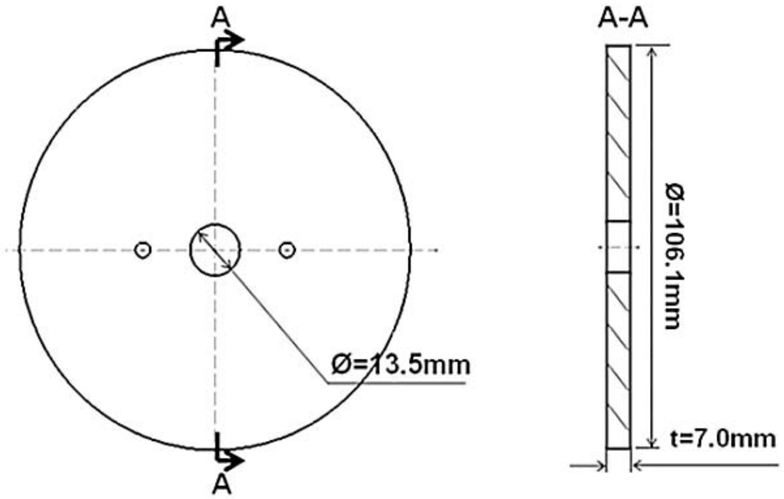

Figure 7.1: Dimension of the cylinder

The modelization starts with the geometry. In this case there is a 2D axialsymmetric model, since the magnetic field H is always parallel to the plane, and the current density vector J is always perpendicular.

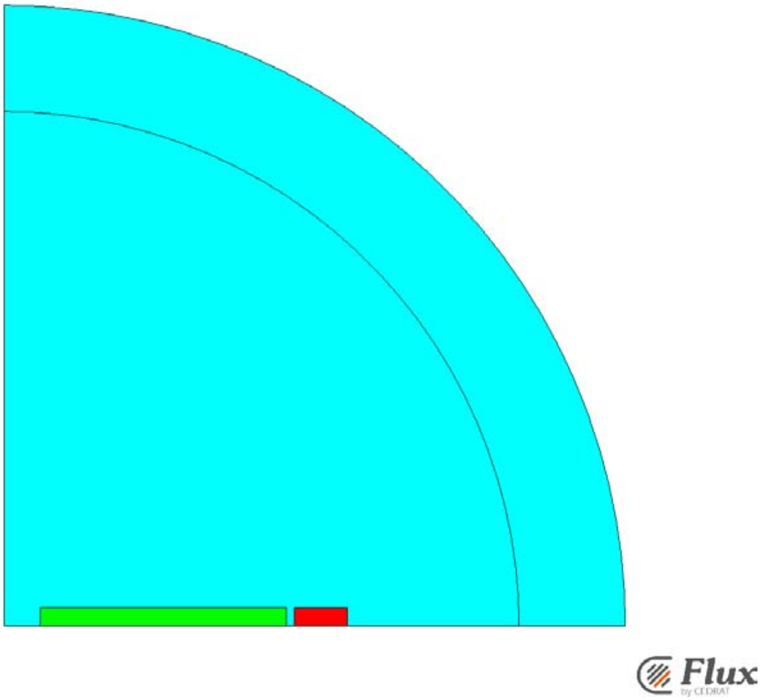

Figure 7.2: Geometry of 2D Model

In the figure it's possible to see how is imposed also a simmetry on the x axis, so the model is limitated to a little portion of the disc. In green there is the disk, in red the simplified inductor, and all around the air, limited by the infinite box.

7.2 Mesh

The mesh process is fundamental to obtain a good solution of the simulation: it has to be finer in the critical point, but also relaxed in no critical ones. In this way the simulation will produce correct results with no big computation power. So near the gap surface the disk elements must have a thickness at least half times the skin depth. So for this material is around 0.3 mm . Same procedure also for the inductor. It's important to use also the mapped region: in this way the solution is more precise than the one with triangular mesh.

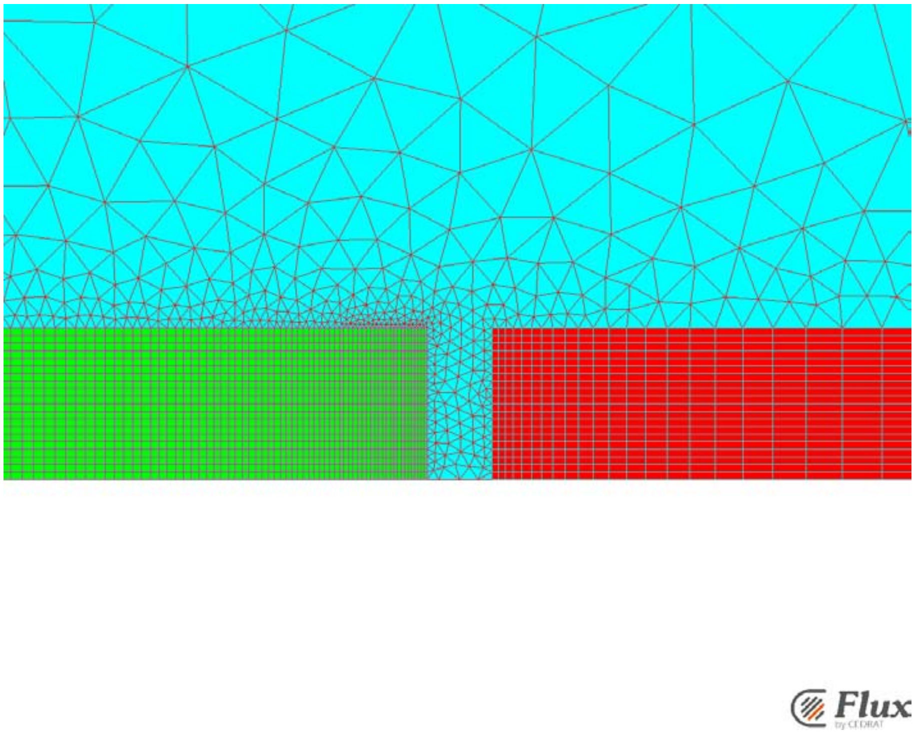

Figure 7.3: Particular of the Mesh

7.3 Material Caratherization

At this time let's define the material propreties: they are all in function of Temperature. Magnetic Permeability could be described in two different equations: linear and with saturation.

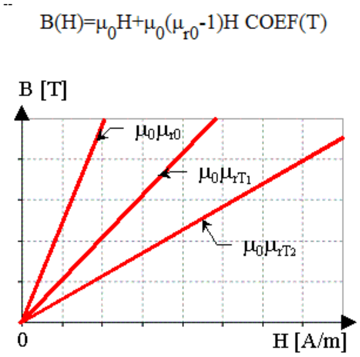

$$B(H)=\mu_0 H+\mu_0(\mu_{r0}-1)H\ COEF(T)$$

Figure 7.4: Linear Relation between B-H + Exponential Relation between B-T

$$B(H) = \mu_0 H + J_{s0} \frac{H_a + 1 - \sqrt{(H_a + 1)^2 - 4H_a(1 - a)}}{2(1 - a)} \mathrm{COEF}(T)$$

$$H_a = \mu_0 H \frac{\mu_{r0}\ \mathrm{COEF}(T) - 1}{J_{s0}}$$

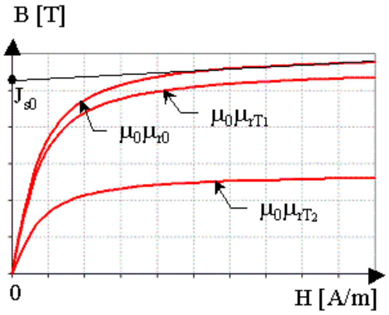

Figure 7.5: Relation between B-H with saturation + Exponential Relation between B-T

In the equation shown in the figures 2 the relationship with the Temperature is define with COEF(T). This coefficient is defined by two exponentials:

- the first, with a negative curvature, is used when the coefficient ranges from 1 to 0.1 (T<T1)

  $$COEF_1(T) = 1 - e^{\left(\frac{T - T_c}{C}\right)} \tag{7.1}$$

  Where Tc is the Curie Temperature, and in this way T1 is the temperature for $COEF_1(T_1) = 0.1$.

- the second, with a positive curvature, is utilized in the neighborhood of the Curie point, when this coefficient ranges from 0.1 to 0 (T>T1)

  $$COEF_2(T) = e^{\left(\frac{10(T_2 - T)}{C}\right)} \tag{7.2}$$

  Where the quantity T2 has the value so that the connection of the two exponentials could be effected in T1.

The shape of the COEF(T) function is represented in the figure below. The decrease of the COEF(T) coefficient is more or less rapid following the value of the C temperature constant. Electric Resistivity is simply considered linear with a stabilization to the Curie Temperature, but it could be also tabulated with different values, as shown in the plot.

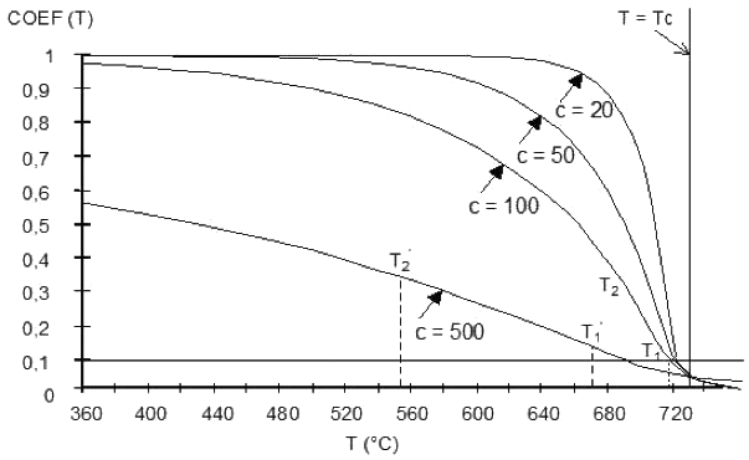

Figure 7.6: Shape of COEF(T) in function of factor C

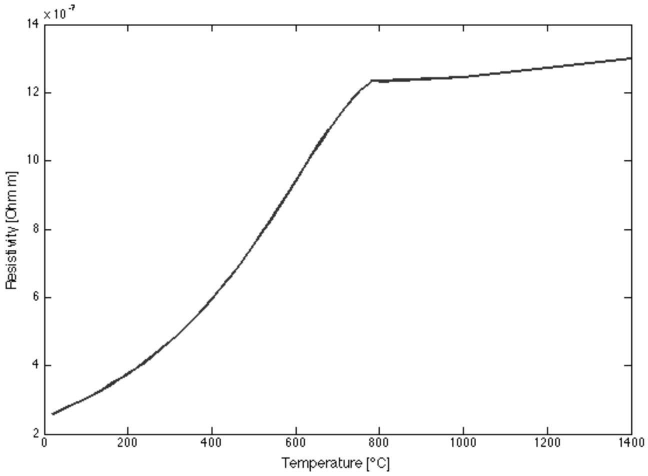

Figure 7.7: trend of the electrical resistivity as a function of temperature

For Thermal parameters we can use a particular function to explain the Specific Heat, which permit us to make more precise calculation, considering also the energy used by material near the central transformation curve.

$$\rho C_p(T) = \rho C_{pi} + (\rho C_{p0} - \rho C_{pi})e^{-T/\tau} + E \cdot Gauss(T)$$

$$Gauss(T) = \frac{1}{\sigma\sqrt{2\pi}} e^{-\frac{1}{2}\left(\frac{T-T_c}{\sigma}\right)^2}$$

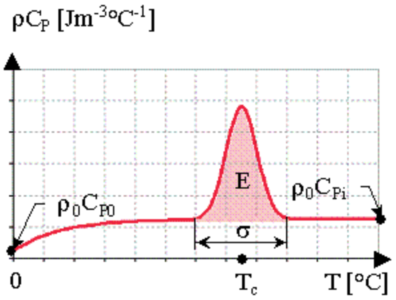

Figure 7.8: Variation of ρCp as a function of Temperature

For Thermal Conductivity, we can consider it costant, or we can tabulate it in function of Temperature.

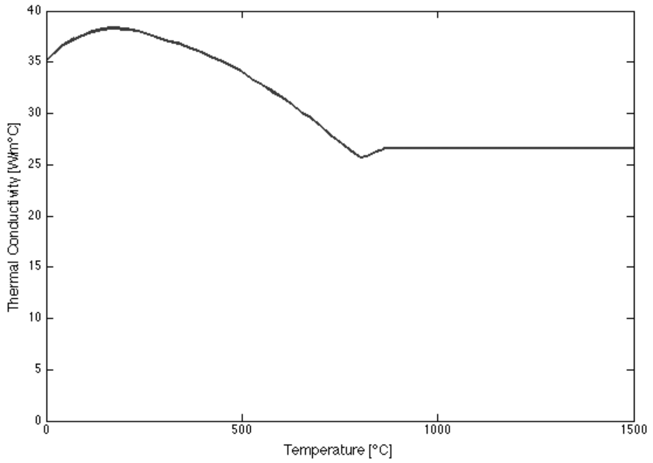

Figure 7.9: Tabulated values of Thermal Conductivity

7.4 Scenario and Solution

The simulation consists in a single shot pulse of 0.5 seconds in HF (190 kHz). In this way is possible to compare with sperimental tests done on the same geometry. From the simulation is possible to see the temperature distribution at the end of the process, and the distribution of the power on the piece, which is localized all on the surface. It's also clearly visible the edge effect that concentrate the heat on the corner of the piece.

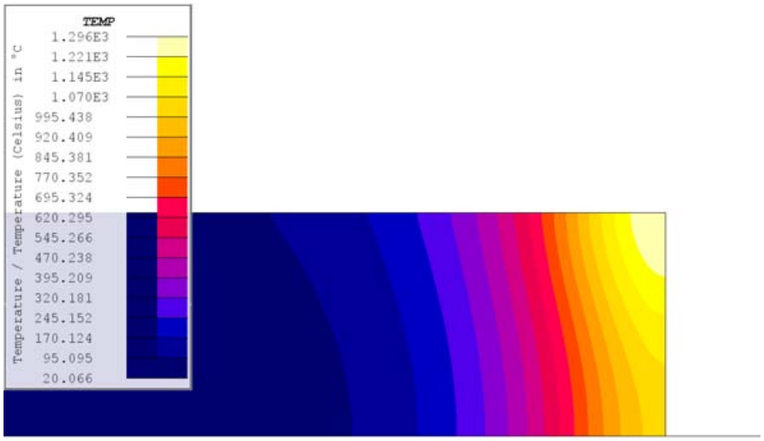

Figure 7.10: Temperature Distribution at 0.5 s

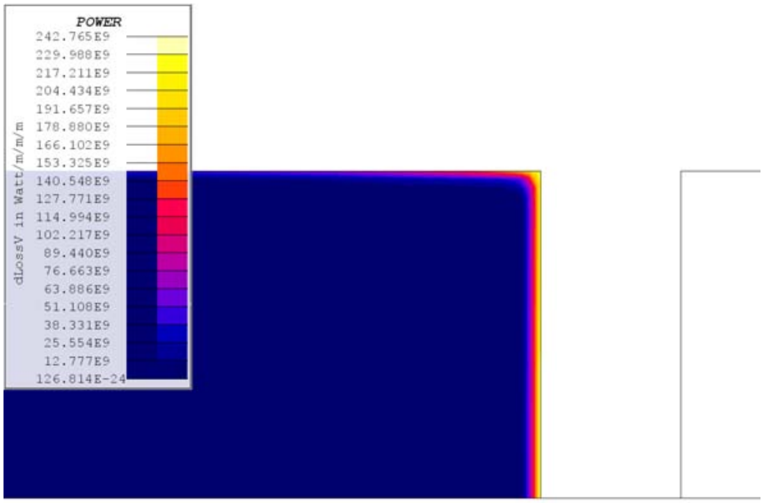

Figure 7.11: Distribution of Power on piece at beginning of the process

7.5 Parametric Solution

To find the correct material parameters to use in the model it has been solved two different parametric simulations: in first one the Curie Temperature varies from a minimum of 700°C to 775°C; in the second one the Central Temperature, parameter of Volumetric Heat heavly influenced by the speed of heating, varies from 800°C to 900°C.

7.5.1 Curie Temperature

As it is possible to see in the following figure, the variation of the Curie temperature doesen't affect so much the distribution of 816°C isotherm, probably beacuse it's near to the imposed Curie Temperature. The difference is visible to higher temperatures (like 927°C and 1038°C) where highest heating rate to get similar results with the tests is with higher values of the Curie Temperature. For this reason is reasonable consider the Curie Temperature equal to 775°C.

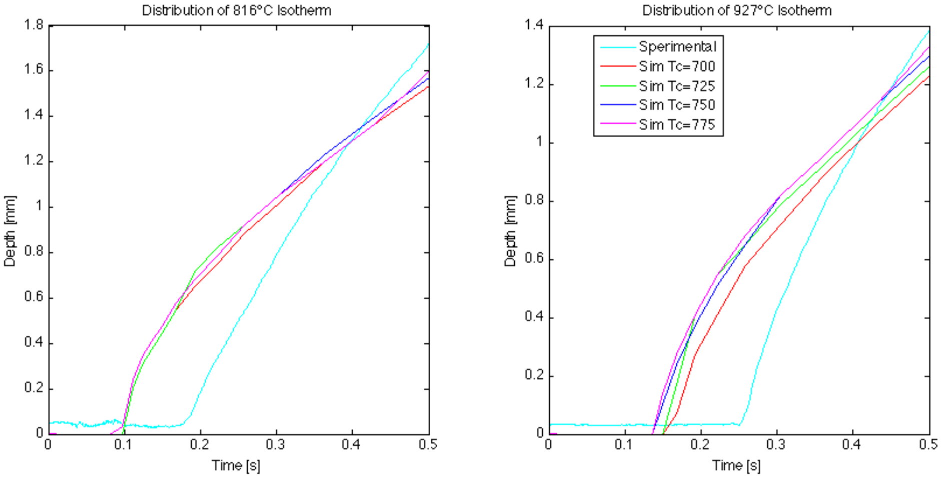

Figure 7.12: Comparison with different Curie Temperature

7.5.2 Central Temperature Volumetric Heat

The volumetric heat curve is obtained by sperimental test, done with very little variation of the temperature, so in so called "static condition". The problem is that the transformation temperature of the material change in function of the heating rate. So it's intresting to see how change the distribution of the temperature on the piece in function of the different shifted curve, show as follow.

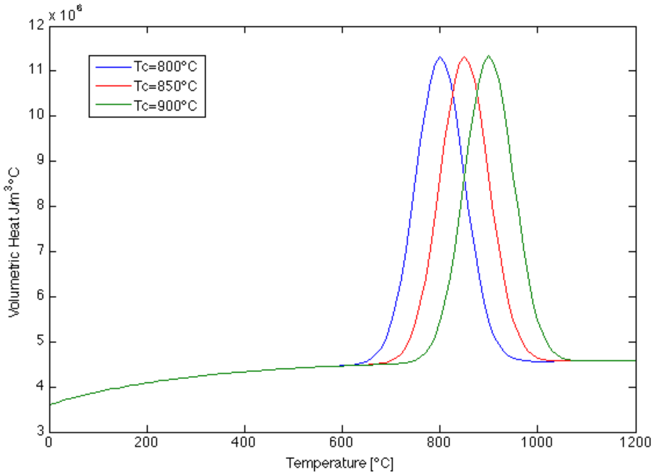

Figure 7.13: Volumetric Heat Curve Shifted

There are no significant differences of the isotherm distribution in function of the Central Temperature of Volumetric Heating Curve. For this reason let's consider the Central Temperature used in literature for this kind of heating: 870°C . So the Ac1 temperature will be approximately 810°C and Ac3 920°C.

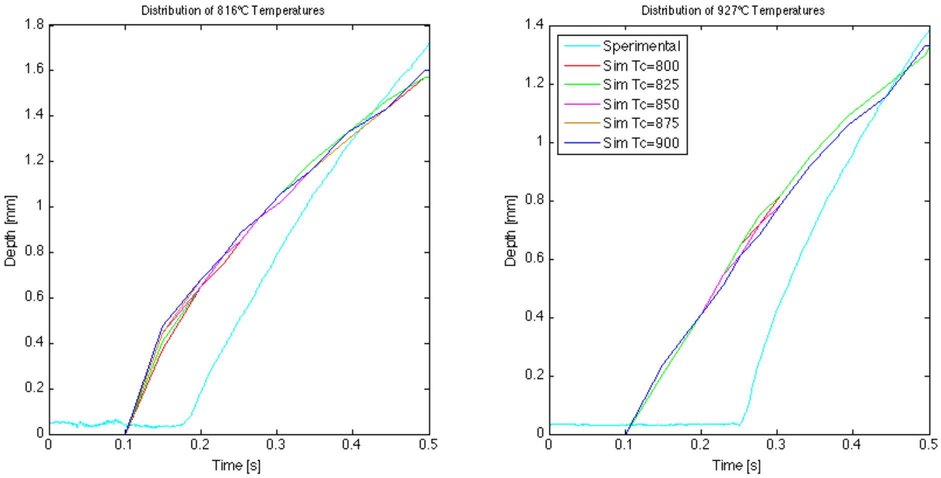

Figure 7.14: Comparison with different Central Temperature

7.6 Costant Power Solution

The results with the parameters show before is quite different from the results obtained in the test, but final distribution is quite similar. The main problem is that the simulation are lead by an imposed voltage on the inductor, instead the sperimental tests are controlled in

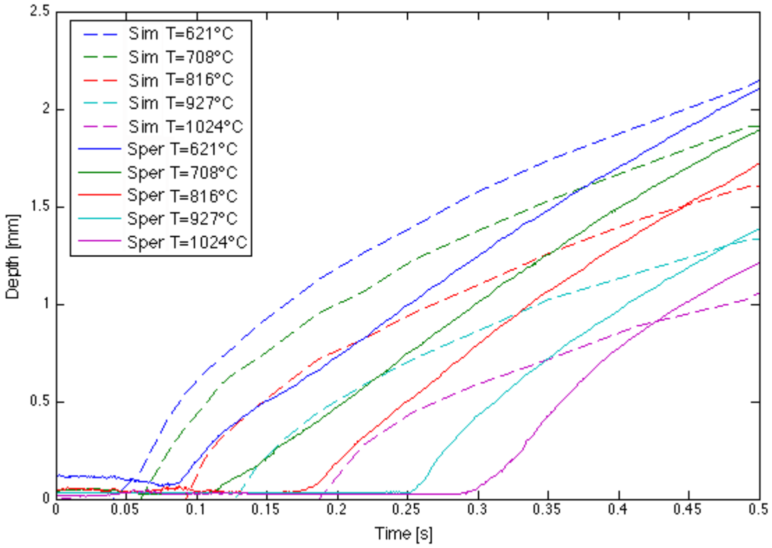

Figure 7.15: Temperature Distribution

costant power. In the simulation the power in the piece can change also of 5-10%, and this will change a lot the results. For this reason is intresting to simulate the process of costant power. Unfortunately with the software is impossible to do, but it's possible to change the voltage, so the peak of power will be lower, and the power at the end of the process will be higher. It's possible to see how the solution is better, more similar to the test. This suggest to perform other test imposing the current on the coil instead of the power of the machine.

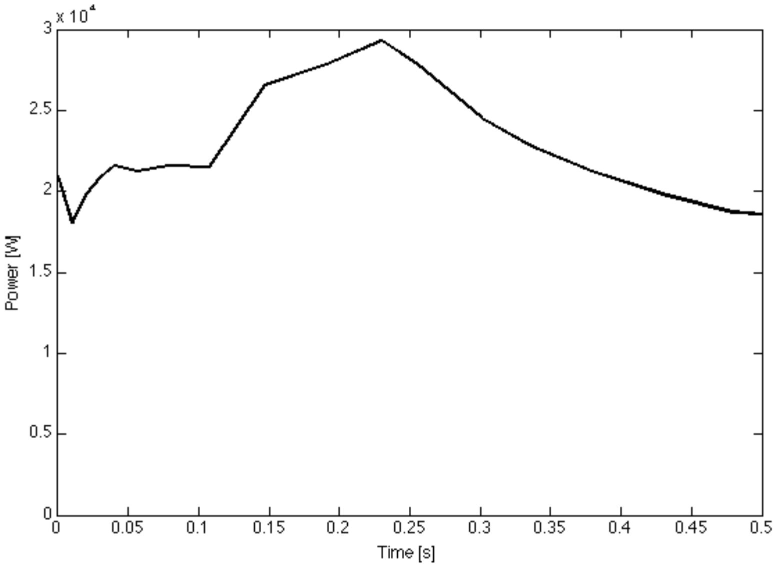

Figure 7.16: Power behaviour in Time

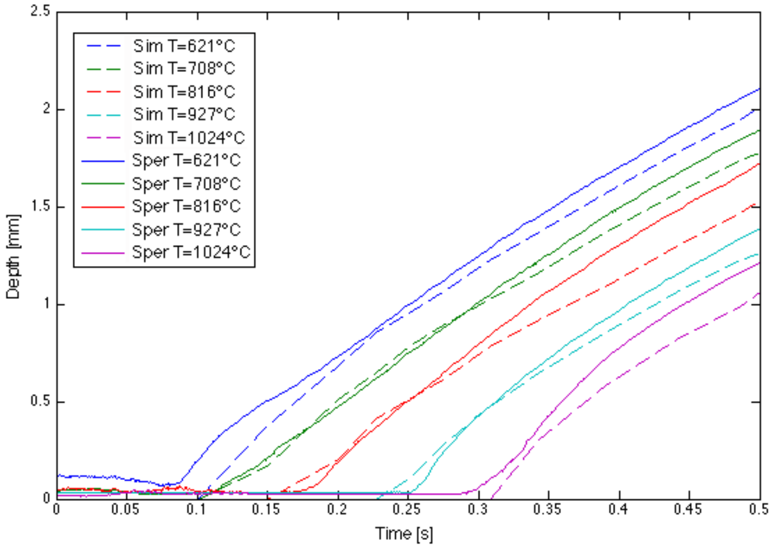

Figure 7.17: Distribution with Power Control

8 Modelization of Induction Hardening on a gear

8.1 Geometry

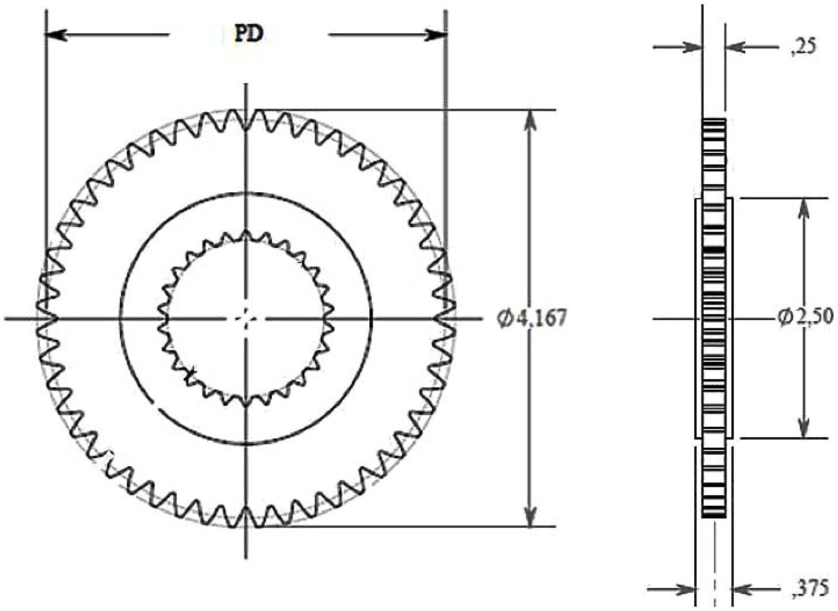

Figure 8.1: Dimensions of the Gear

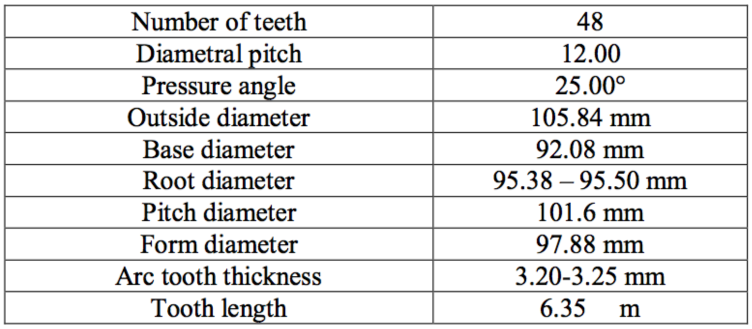

Number of teeth	48
Diametral pitch	12.00
Pressure angle	25.00°
Outside diameter	105.84 mm
Base diameter	92.08 mm
Root diameter	95.38 – 95.50 mm
Pitch diameter	101.6 mm
Form diameter	97.88 mm
Arc tooth thickness	3.20-3.25 mm
Tooth length	6.35 m

Figure 8.2: Data of the gear

The modelization starts with the geometry. In this case let's consider only 1/8 of tooth of gears, so there are 3 different conditions of symmetry:

- On plane x-y,
- Along the root
- On the top of the tooth

Same operations have been done also to the inductor, obtaining the following geometry.

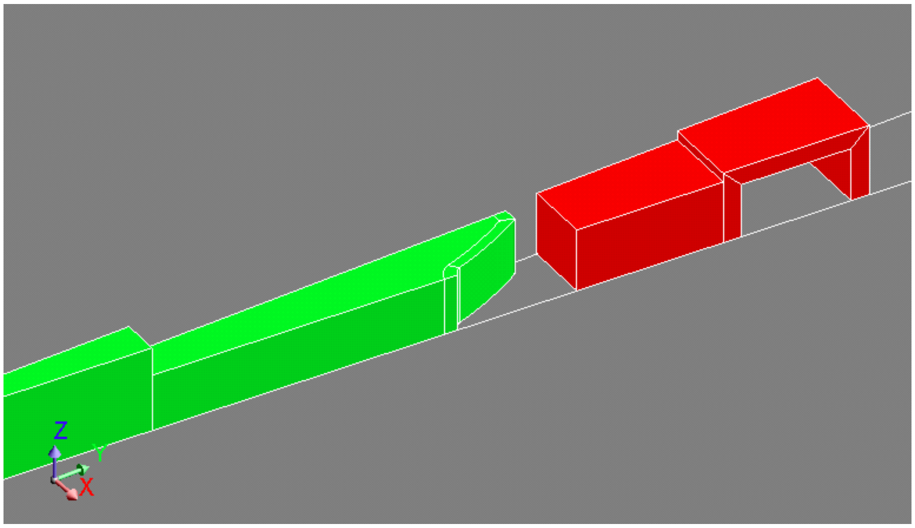

Figure 8.3: Geometry of Problem

8.2 Mesh

In this model is really important to create an appropriate mesh, in order to have both precise solution and fast calculation. For this reason different types of Meshlines have been created. First of all on the external layer of the tooth are imposed at least 2 elements in the skin effect depth (size element 0.07 mm), then is applied a relax factor size elements in the depthh of the piece. Same process is applied also on the conductor . Then on the volumes of conductor and the external volumes of the tooth are imposed mapped elements: in this way there is better solution, with no heavier calculation. In all other volumes are imposed relaxing rules in this way the model is ligther.

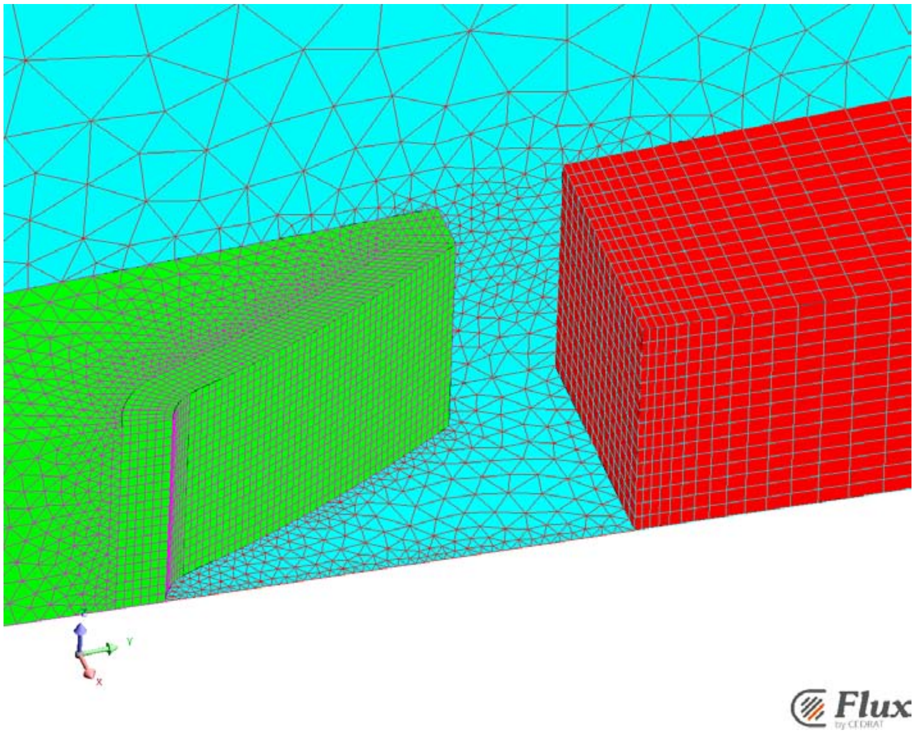

Figure 8.4: Particular of Mesh of Tooth and Inductor

8.3 Formulations

The formulation used in this kind of problem is the T, ω approach:

$$\nabla \cdot J = 0 \rightarrow \bar{J} = \nabla \times \bar{T} \tag{8.1}$$

$$\nabla \times (\bar{H} - \bar{T}) = 0 \rightarrow \bar{H} - \bar{T} = -\nabla\omega \tag{8.2}$$

$$\nabla \times \rho\nabla \times \bar{T} + \mu\frac{\partial\bar{T}}{\partial t} - \mu\nabla\frac{\partial\omega}{\partial t} = 0 \tag{8.3}$$

$$-\nabla \cdot \mu\nabla\omega + \mu\nabla \cdot T = 0 \tag{8.4}$$

The first equation says that if in all the space there is the divergence of current density equal to zero, then there must be an electric potential vector T. So the curl of this electric potential vector is equal to the current density. The second equation consider that both curl of H and T are equal to J, neglecting displacing current, so their difference must be equal to zero. If the curl of a vector is zero, there must be a scalar potential ω. Combining the first two equation with the other Maxwell equations, it's possible to easily obtain equation 3 and 4, which resolve the problem. In such way it computes quickly the eddy currents and so the power dissipation in the piece. All these equations are solved in the domain of frequency (harmonic solution), and it's used a direct solver, which is quicker but it needs a lot of RAM. The thermal problem is solved with Fourier equations, and it is solved as a transient, this separation between thermal and magnetic is possible thanks to the magnetic time costant which is very little compard to the thermal one.

8.4 Scenario

A scenario has been created for the resolution of the problem. First was imposed a voltage of 1.65 V on the symmetrical planar faces of the coil, with a frequency of 190 kHz for a time of 2 seconds. This is a simple pulse recipe, just to check if the modelization procedure is correct for the process analyzed. The time step is adaptative, so the solver decide the best time step value to use in order to get convergence of the problem.

8.5 Solutions

After the calculation process, lasted about 2 days on the workstation with 16 Gb of RAM, it's possible to figure out the distributions of the main quantities, like temperature .

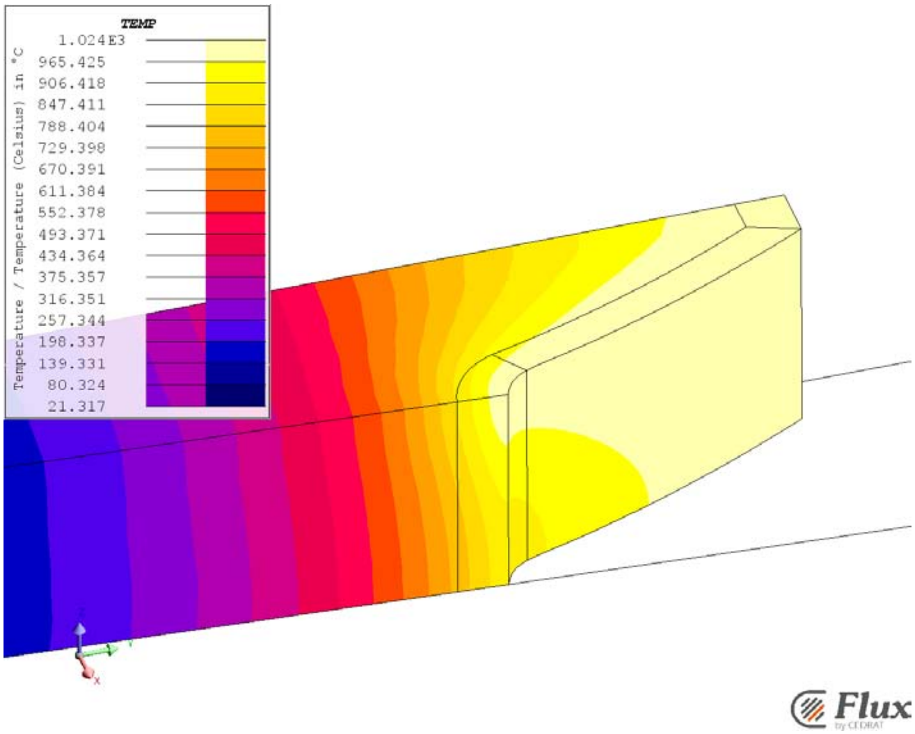
TEMP
Temperature / Temperature (Celsius) in °C
1.024E3
965.425
906.418
847.411
788.404
729.398
670.391
611.384
552.378
493.371
434.364
375.357
316.351
257.344
198.337
139.331
80.324
21.317
x
Flux
by CEDRAT

Figure 8.5: Temperature Distribution after 2 s

Is visible how is important the edge effect: in fact the peak of the temperature is not uniform in all the external part of the tooth. This is confirmed also by the distribution of the volumetric power in the piece: it is almost concetrate in the external part of the root, as show in the figure.

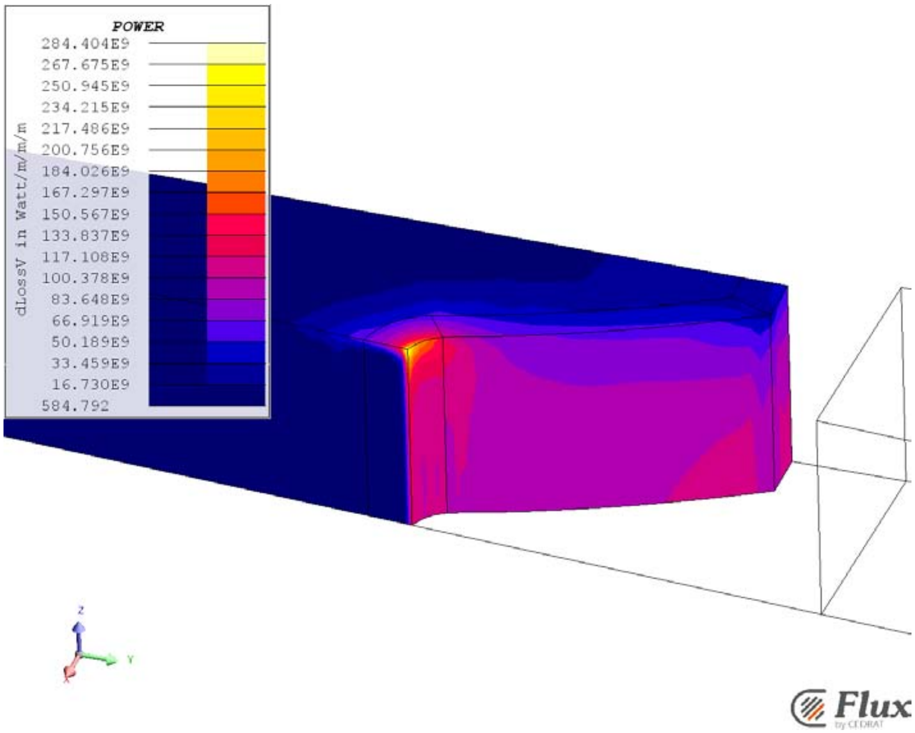
POWER
284.404E9
267.675E9
250.945E9
234.215E9
217.486E9
200.756E9
184.026E9
167.297E9
150.567E9
133.837E9
117.108E9
100.378E9
83.648E9
66.919E9
50.189E9
33.459E9
16.730E9
584.792
dLossV in Watt/m/m/m
Z
Y
X
Flux
by CEDRAT

Figure 8.6: Power Distribution

We can do also a visual check of the depth of the isotherms comparing the simulation results with the test already done on the piece.

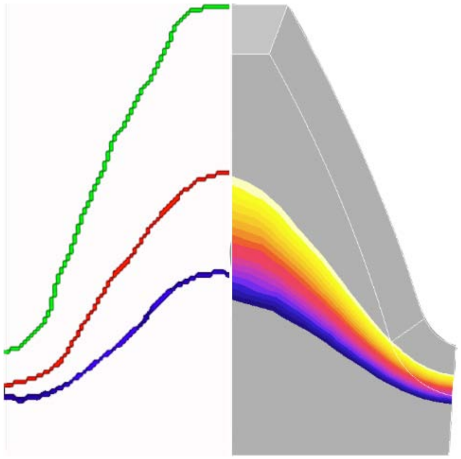

Figure 8.7: Comparison of Isotherm distribution at 2s

It's possible to see how are near the simulation results with the tests one, the differences are dued to the non perfect modelization of the material.

8.6 Linear vs Non Linear B-H Relationship

Since the non linear simulation (shown above) take a lot of time to running out, it's intresting to evaluate the solution obtained by a linear simulation. The linear simulation consider the relative permeability costant for every magnetic field, and vary only with the temperature. This approximation affects the distribution of the magnetic field on the piece, but it doesn't change so much the heating profile at the end of the process.

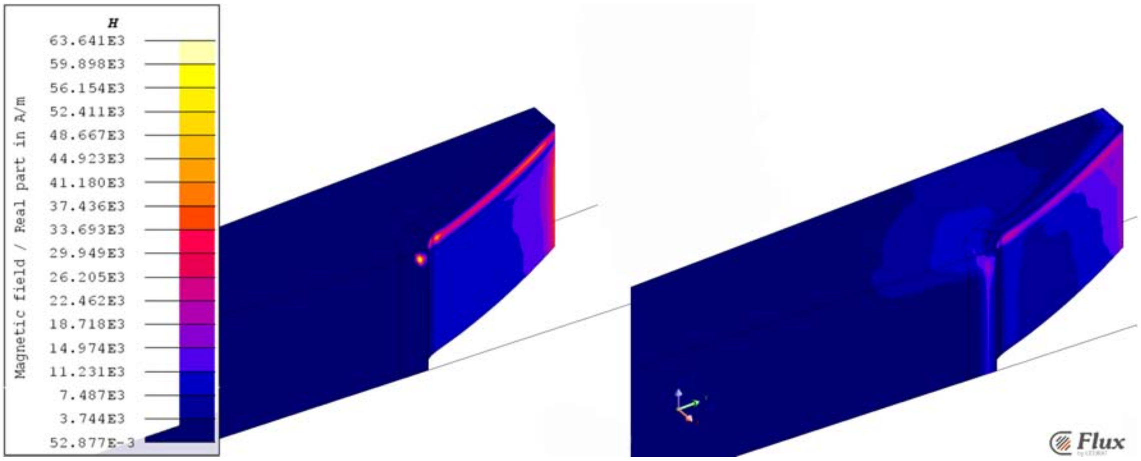

Figure 8.8: Comparison of H field at first step between Non linear (left) and Linear (right) simulations

Looking at the distribution of H field at the beginning of the process, it's possible to see how are different the distributions and the values in the 2 cases. In the non linear simulation there are higher values, concentrated on the side of the tooth. Instead in the linear one there are lower values, distributed also on the top part of the tooth.

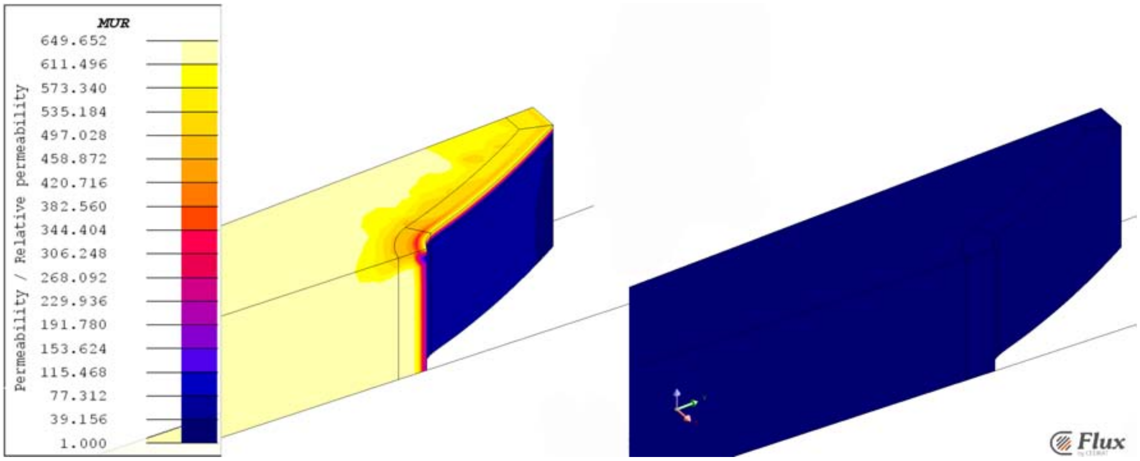

Figure 8.9: Comparison of Relative Permeability at first step between Non linear (left) and Linear (right) simulations

The big difference is in the relative permeability at the beginning of the process. In fact the linear simulation starts with an uniform distribution of μ_r, that is equal to value chosen (in this case 15). Instead the non linear simulation have much higer values, considering also the saturation effect produced by the so high field. In fact all the side part of the tooth has very little value of μ_r, approximately 1.

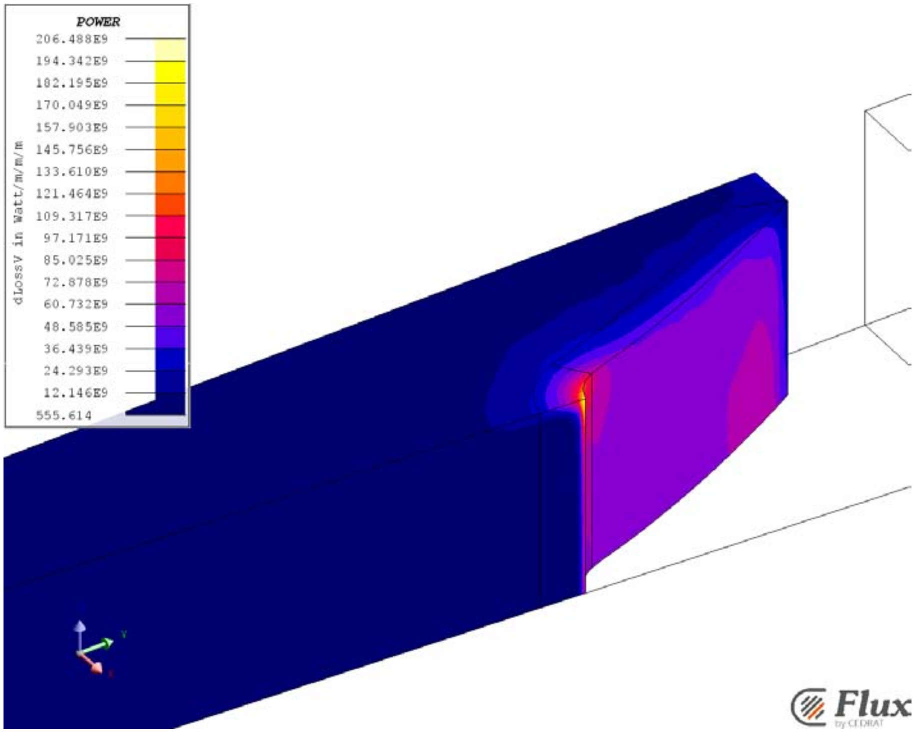

Figure 8.10: Power Distribution in Linear Simulation

But the power distribution is really similar between the two simulations, this means that the thermal distribution will be really similar. With a Matlab script it is easy to create some graphs to compare the two solutions with the tests.

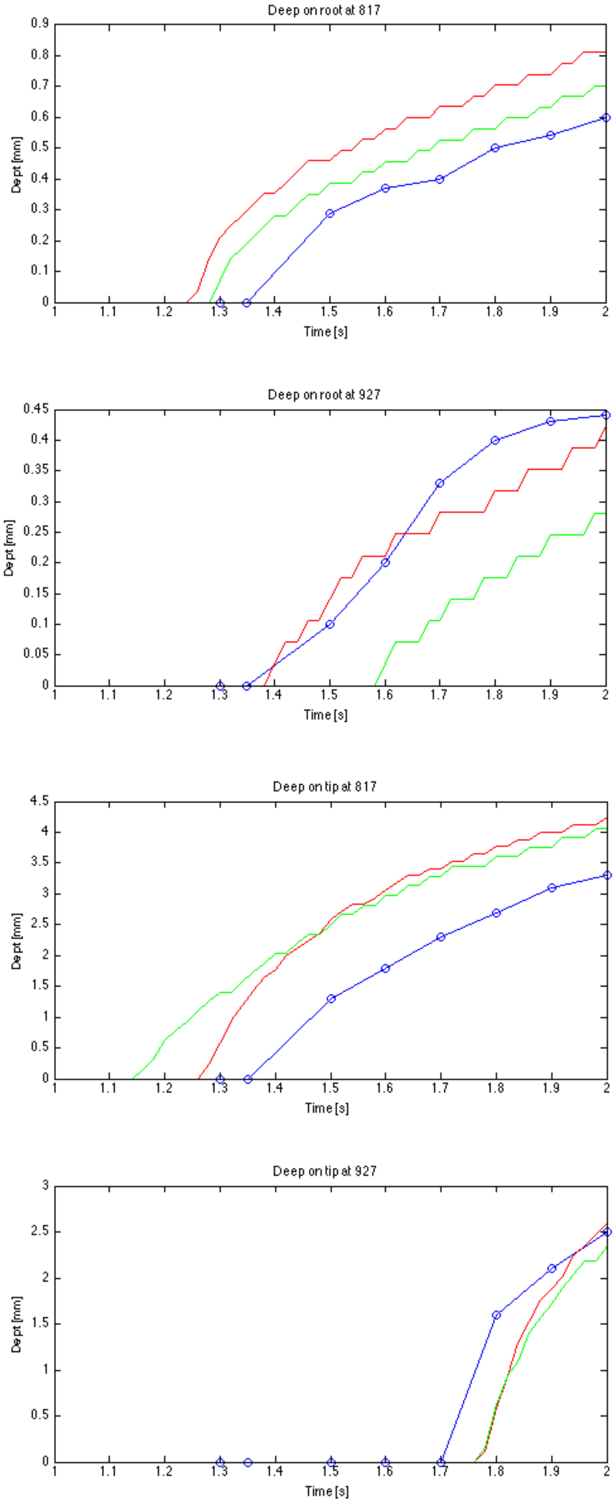

Figure 8.11: Comparison of Isotherms depth: Blue-Sperimental; Green-Linear Sim; Red-Non Linear Sim

8.7 Considerations

From these results it's possible to determine that the model correct, having good approximation with the real results. There are some differences due to the not so good mesh, maybe smaller elements in some strategic parts like the root could create better results, but with so much heavier simulation. But the main difference is that the tests are done in costant power, instead the simulation are voltage controlled. This lead to errors that could be corrected in simulations, as shown before, but the best way should be running some new test imposing the current in the inductor, and not the power of the machine. Finally it's possible to see that the linear simulation is similar to the non linear one, but there is a big limitation: it's necessary to predict correctly the value of μ_r combined with the power in the piece. In fact lower values approximate the piece as imposed with higher values of H field, so with big saturation; instead higher values of μ_r approximate the piece as imposed with lower values of H field. Combining this values with the voltage imposed on the inductor it's possible to obtain so different solutions of the problem. This thing is simplier with the non linear simulation, where there is only the voltage to impose on the inductor, and the material automatically choose the correct value of μ_r depending by the imposed field.

Part III

Experimental Test

9 Induction Hardening Machine: EFD SINAC 650

The EFD induction heating machine consists of four parts:

1. The average frequency generator (MF) that can handle parts with a constant frequency of 10 kHz.
2. The high-frequency generator (HF) which operates with a frequency between 150 kHz and 250 kHz. This generator has the feature to adjust the frequency depending on the inductor used and the workpiece.
3. The active part of the machine which contains the inductor, shower cooling the workpiece and the filter that can simultaneously use both generators.
4. The control panel that allows to select the desired power to choose between a manual or automatic processing, adjust the position of the workpiece and display measurement readings made during the treatment.

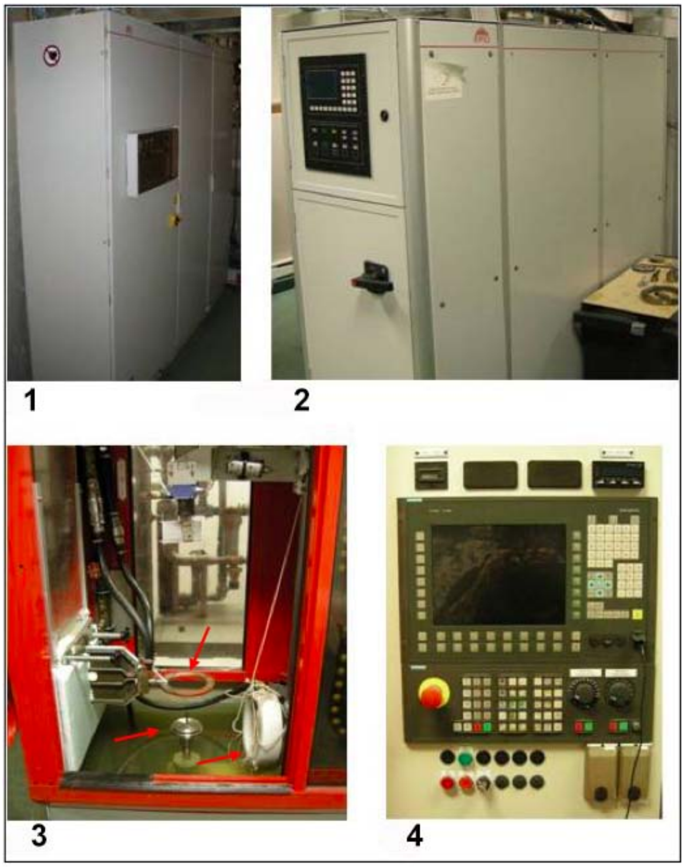

Figure 9.1: EFD Machine

The operation of this machine can be summarized using the simplified circuit design shown in the figure. A diode rectifier is connected to a mains 3 x 480 V (orange on the diagram). The current thus rectified is sent to the frequency converters that provide current to the desired (green) frequency. From there the current passes through a matching transformer to reduce the voltage and increase the intensity (in yellow). Finally, a capacitor reactive power compensation (red) is used to provide the required reactive power. Indeed, inductive machines consume a lot of reactive power, which leads to a large power consumption, voltage drop and large energy losses. To minimize adverse impacts on the power grid, it is necessary to create its own reactive power through capacitors. In the figure, top left, the HF generator, bottom left is the MF generator, and right filter. This allows not only to filter the current signal, but it also prevents the RF current back in MF generator because both HF and MF outputs are connected to the same inductor.

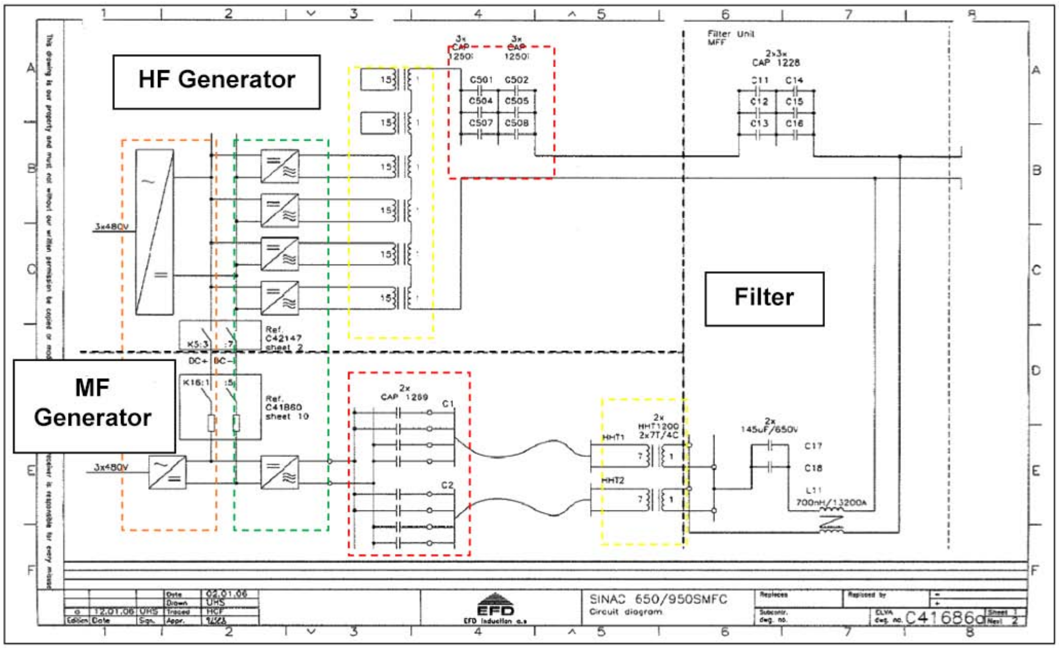
HF Generator
MF Generator
Filter
3x480V
3x480V
3x CAP 1250
3x CAP 1250
C501
C502
C504
C505
C507
C508
15
1
K5:3
:7
Ref. C42147 sheet 2
DC+
DC−
K16:1
:5
Ref. C41860 sheet 10
2x CAP 1289
C1
C2
2x HHT1200 2x7T/4C
HHT1
HHT2
7
1
Filter Unit MFF
2x3x CAP 1228
C11
C14
C12
C15
C13
C16
2x 145uF/650V
C17
C18
L11
700nH/13200A
1
2
3
4
5
6
7
8
A
B
C
D
E
F
Date 02.01.06
Drawn UHS
Traced HCF
Appr.
a 12.01.06 UHS
Edition Date Sign.
EFD
EFD Induction a.s
SINAC 650/950SMFC
Circuit diagram
Replaces
Replaced by
Subcontr. dwg. no.
CLVA dwg. no. C41686d
Sheet 1
Next 2

Figure 9.2: EFD Circuit

9.1 Different Working Modality

In order to adapt to different types of induction heaters, the EFD machine can be used in two modes. The pilot generator in constant power mode called "DC power", the other AC constant nominal value, called "AC current" mode. The first mode is particularly suitable for constant loads and industrial production, while the second is for applications with varying impedances, or corresponding to changes in geometry. Figure 2.3 illustrates the difference between the two control modes. It is clear that the power remains constant during heating in DC mode power then it increases initially and then decreases to a certain time in AC current mode. This change in power control constant current is explained by the fact that at the beginning of the heating, as the temperature of the workpiece surface is less than the Curie temperature and for a given current, as the power increases of electrical resistivity increases with increase in temperature. When the Curie temperature is reached, the depth of penetration increases, the eddy currents move a little deeper into the piece. Or as the current is constant, the magnetic field decays over the area where the Curie temperature is reached increases. Therefore the heating power by Joule effect, the induced magnetic field decreases.

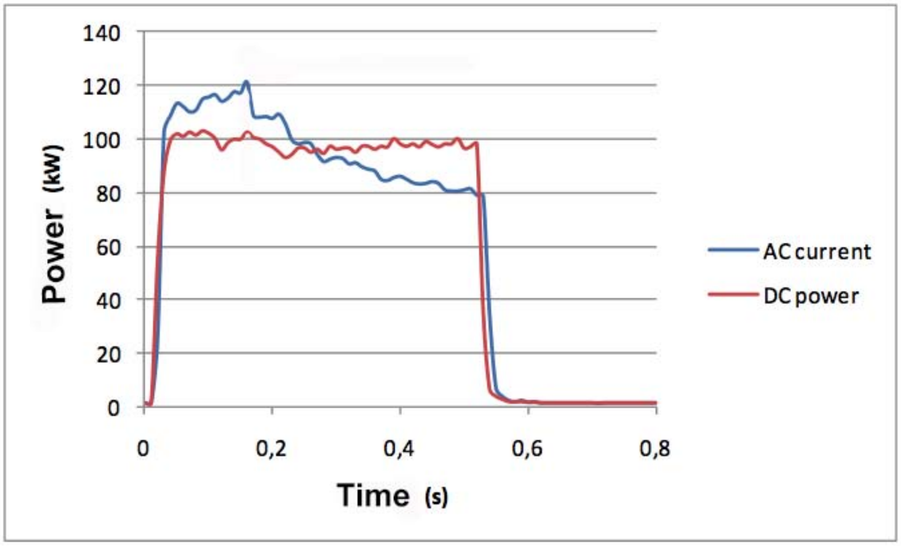

Figure 9.3: Comparing power trend during time in the two modes

10 Data Acquisition

The experimental setting is shown in figure below. Prior to each test, the upper side of the spur gear was coated with a specific temperature-indicating lacquer. Such lacquers contain chemicals in suspension that transform or evaporate at given temperatures, with an accuracy of ±1% of the indicated temperature. A high- speed camera is set above the gear by means of a tripod. The magnification is adjusted so that three teeth are observed within the camera field of view. The gear is lightened up enough for the lacquer coating to appear uniform. The camera records 512 x 352 pixels images at a frame rate of 2000 images per second. A total duration of 4 s (8,000 images) is recorded for each test. The resulting images have a spatial resolution of 40 lm/pixel and a temporal resolution of 0.5 ms between two frames.

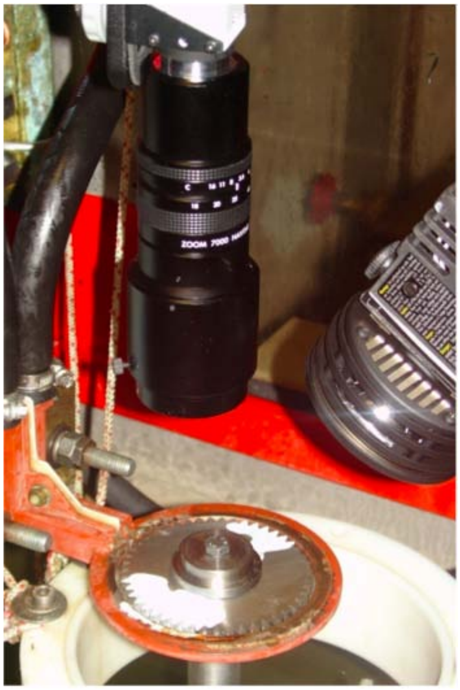

Figure 10.1: Data Acquisition Set Up

The interface between the evaporated and the non-evaporated lacquer indicates the isotherm specific to this lacquer. The different steps required for extracting an isotherm from the raw images recorded by the camera system are summarized inthe scheme.

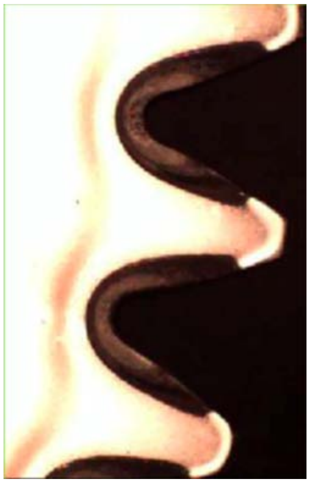

Figure 10.2: Detail of Gear Analyzed

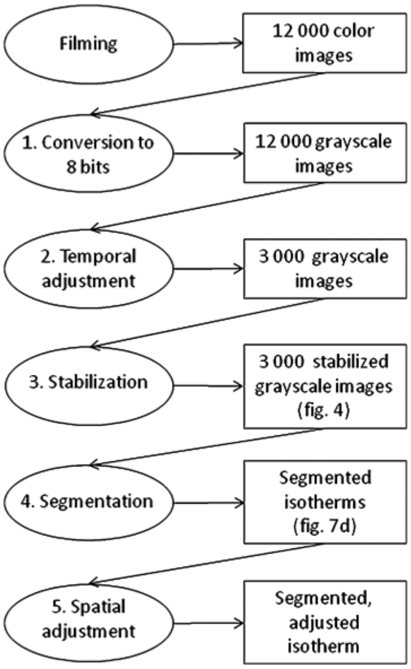
Filming
12 000 color images
1. Conversion to 8 bits
12 000 grayscale images
2. Temporal adjustment
3 000 grayscale images
3. Stabilization
3 000 stabilized grayscale images (fig. 4)
4. Segmentation
Segmented isotherms (fig. 7d)
5. Spatial adjustment
Segmented, adjusted isotherm

Figure 10.3: Scheme for Data Elaboration

The 8,000 images composing the movie are first converted into 8-bit images (255 gray levels). A temporal adjustment is thus needed. It is carried out at the beginning of the treatments and consists of defining a timing reference to which all tests will be referred. By convention, this temporal reference is defined as the end of the HF heating treatment. It is automatically determined by identifying the frame in which the intensity at the root between the teeth is maximal. The stabilization operation intends to eliminate

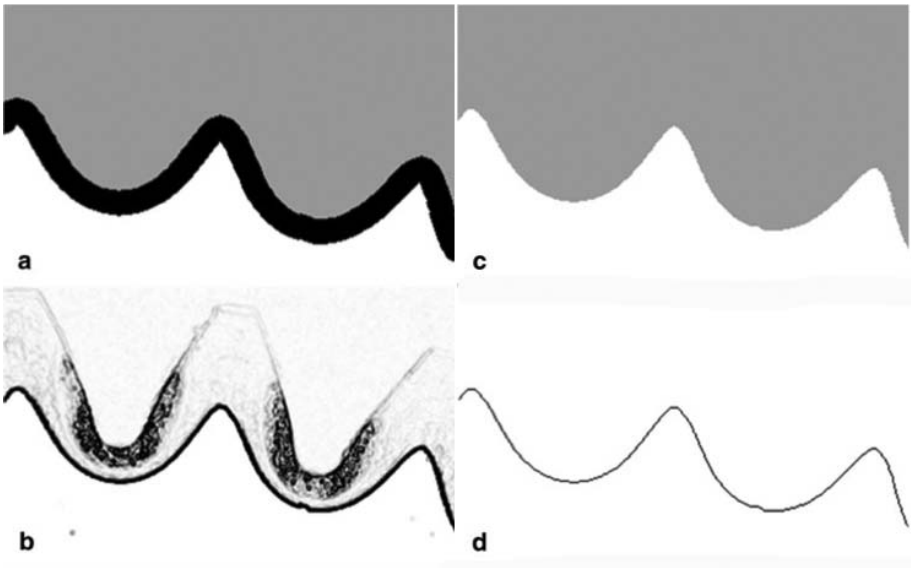

Figure 10.4: Images corresponding to different steps in the image processing(a) Markers, (b) gradient, (c) watershed output, and (d) isotherm

the vibra- tions which introduce small periodic translations between successive images. In the segmentation step the goal is to divide each image into two regions, namely the non-evaporated lacquer and the rest of the image. To do that is needed a robust approach, called ‘‘marker-controlled watershed’’.

The principle of the watershed relies on the equivalence between a gray valued image and a topographic surface, each gray level corresponding to a certain height. The surface can be described in terms of hills and basins that visually relate to bright and dark zones. In the marker-controlled version of the algorithm, only basins identified by so-called markers are taken into account, the others being ignored. Visually, the markers are represented by homogeneous zones, each identified by a distinctive gray level. In spite of the care given to the experimental setting, the images produced by different tests may have slightly different orientations and dimensions. The last step consists of the spatial adjustment of the batch of segmented images in order to have a common spatial reference frame for all isotherms issued from different tests. This is achieved by a series of rotations, rescaling, and translations.

11 Test on Simple Geometry

11.1 Comparison Costant Power vs Costant Current

The first test was carried out on a simple geometry, such as the cylinder already described in previous chapters: the aim is to obtain a direct comparison between the different modes of operation of the machine. To ensure a proper comparison, it was necessary to calibrate the machine in the constant current mode, so as to have the same power of the constant power mode. Below are shown the comparison plots of the power during the time in the two modes. It's impossible to match instant by instant the power in the two cases, because in constant current mode the power decreases when the cylinder reaches the Curie temperature.

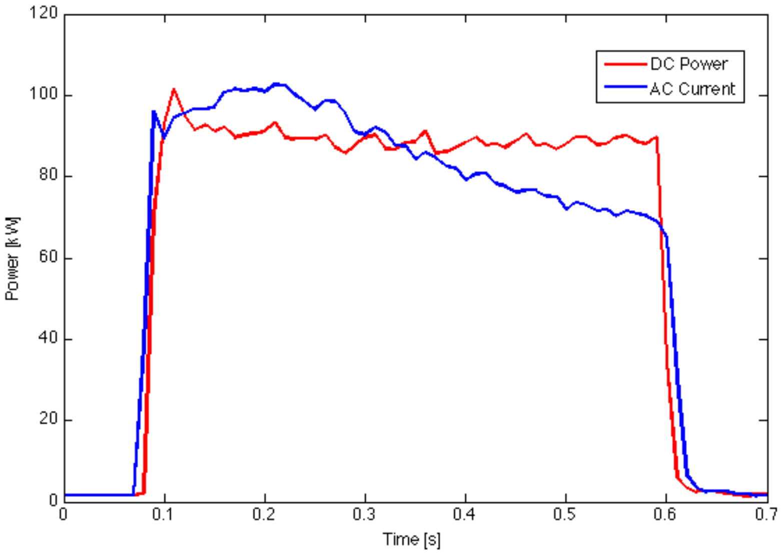

Figure 11.1: Comparison plot of power in the two modalities

11.2 Results

Once carried out the test and processed images in order to extract the depth of the isotherms at 816 ° C, are shown below the results obtained:

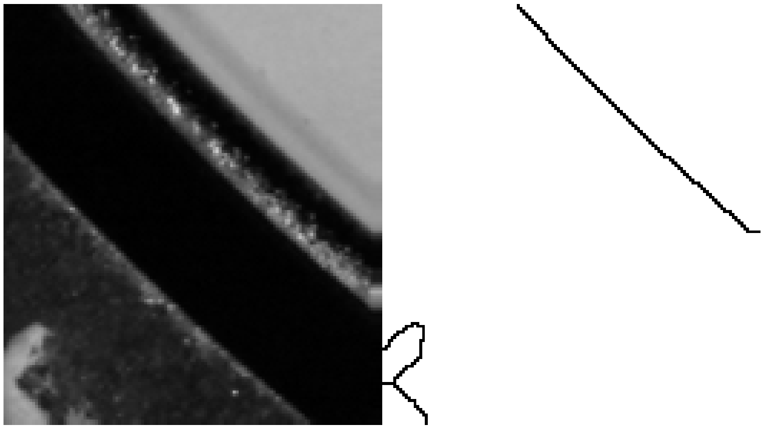

Figure 11.2: Image Analysis of Results

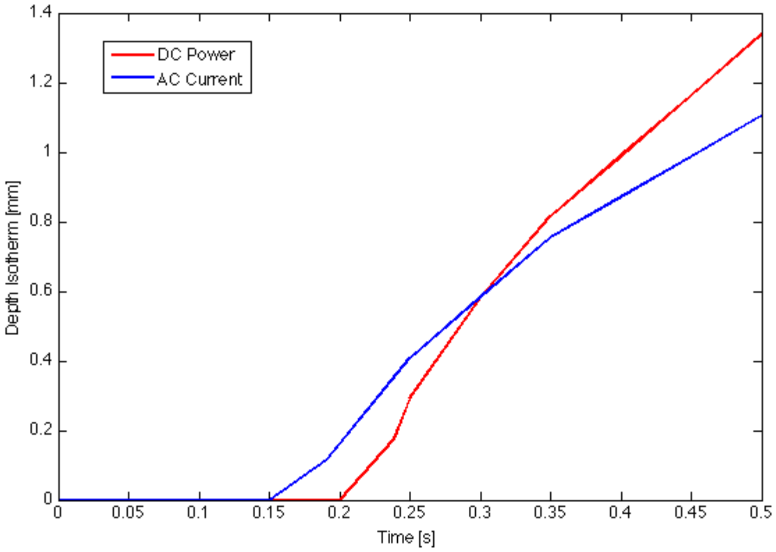

Figure 11.3: Comparison of Isotherm Depth in the two modalities at 816°C

The trend of the isotherm in the constant current mode is very similar to that displayed in the simulations already performed, in fact with more accurate calculations we obtain the following comparison between the test at constant current and the simulation. From the comparison of the two curves, we see that they are very similar to each other. This indicates that the constant current mode is the most suitable in comparison with numerical simulations. Focusing on this aspect, we can estimate the current flowing in the inductor or the power actually dissipated in the piece. The results allow to affirm that to compare experimental data with the simulations it is better to perform the tests at constant current, as this method is most similar to the imposition of boundary conditions of the simulation.

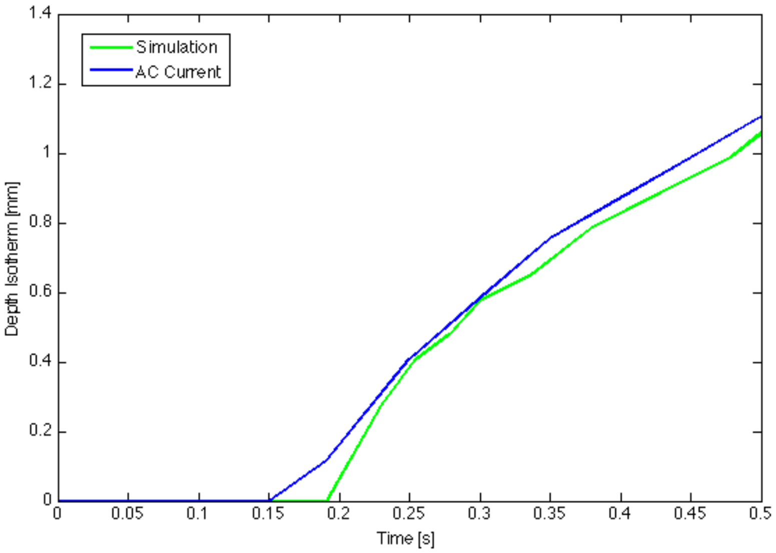

Figure 11.4: Comparison between the simulation and the AC Current mode

12 Test on Gear: EFD112539

The last tests were performed on complex geometry. In particular the EFD112539 geometry was considered, shown in the figure.

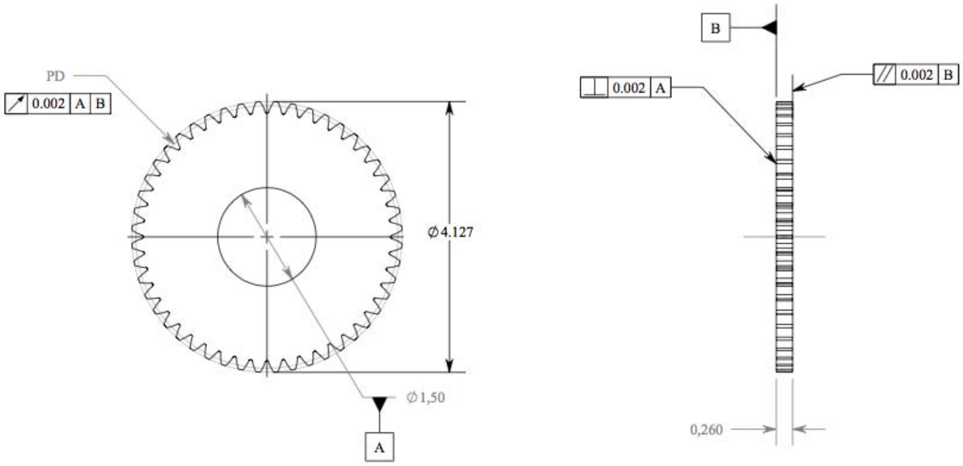
PD
0.002 A B
Ø4.127
Ø1,50
A
B
0.002 A
0.002 B
0,260

Figure 12.1: Geometry EFD112539

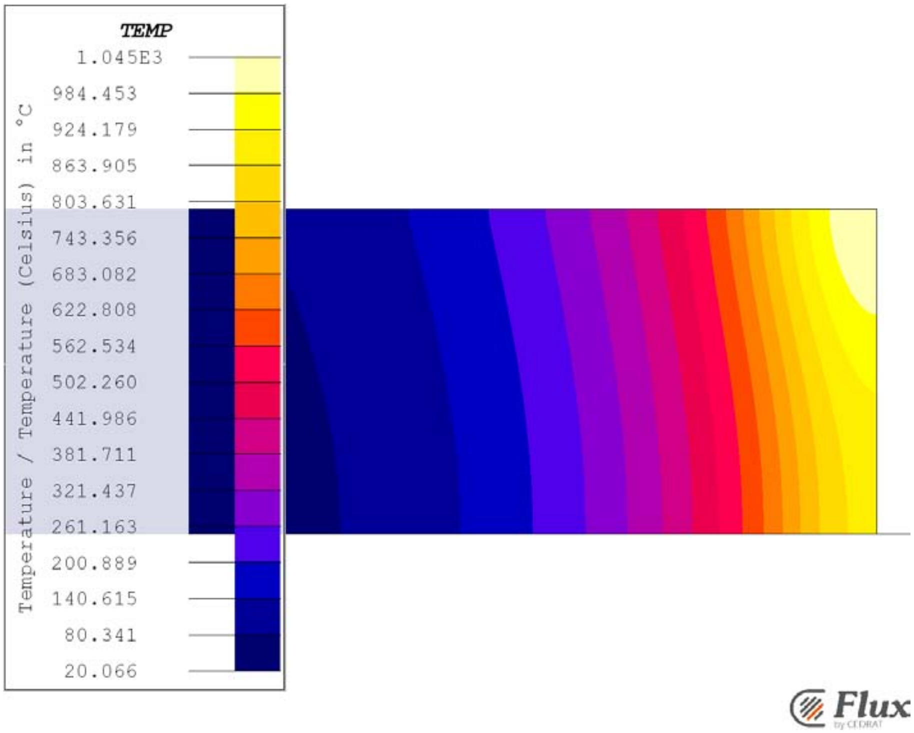

Figure 11.5: Temperature distribution at t = 0.5s

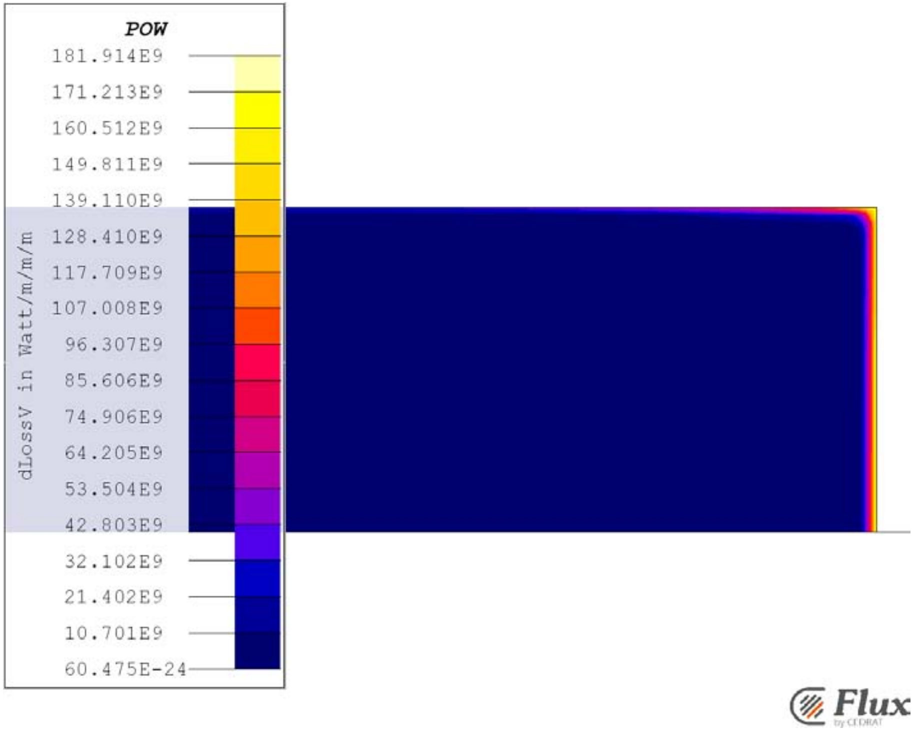

Figure 11.6: Initial Power distribution

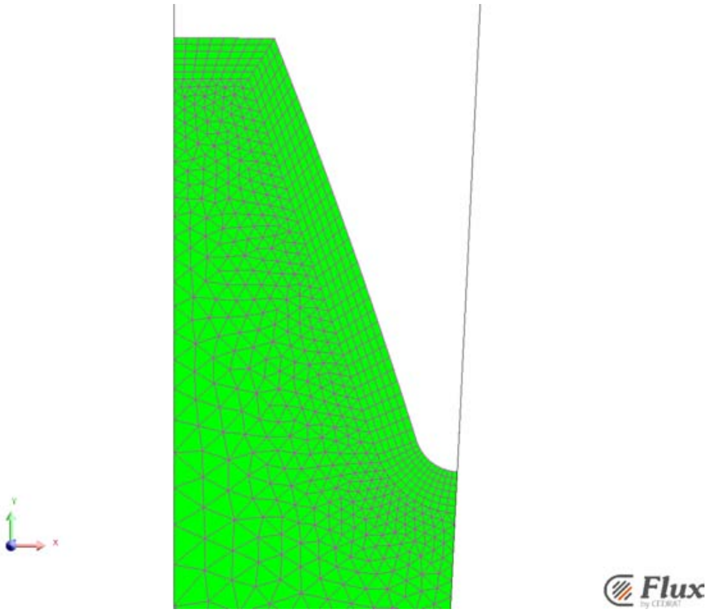

Figure 12.3: Particular of the mesh on half of the tooth

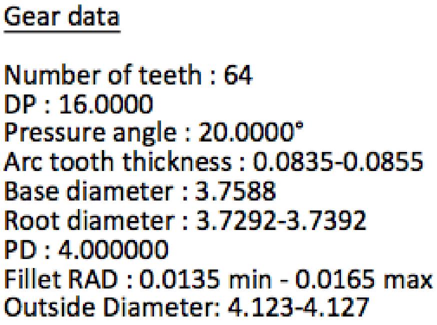

Gear data

Number of teeth : 64
DP : 16.0000
Pressure angle : 20.0000°
Arc tooth thickness : 0.0835-0.0855
Base diameter : 3.7588
Root diameter : 3.7292-3.7392
PD : 4.000000
Fillet RAD : 0.0135 min - 0.0165 max
Outside Diameter: 4.123-4.127

Figure 12.2: General data of EFD112539

12.1 Model Construction

The model is build in the same way described in chapter 8, in particular the mapped regions are focused on the surfaces faced on the air gap, with size elements smaller than the other model previously described, since the geometry has more teeth, but maintain the same diameter, so the region of study is really little.

12.2 Test and Solutions

The recipe for the comparison with the simulations is composed of 3 phases: preheating, diffusion and heating. The preheating phase lasts 1.2 seconds with a frequency of 10 kHz

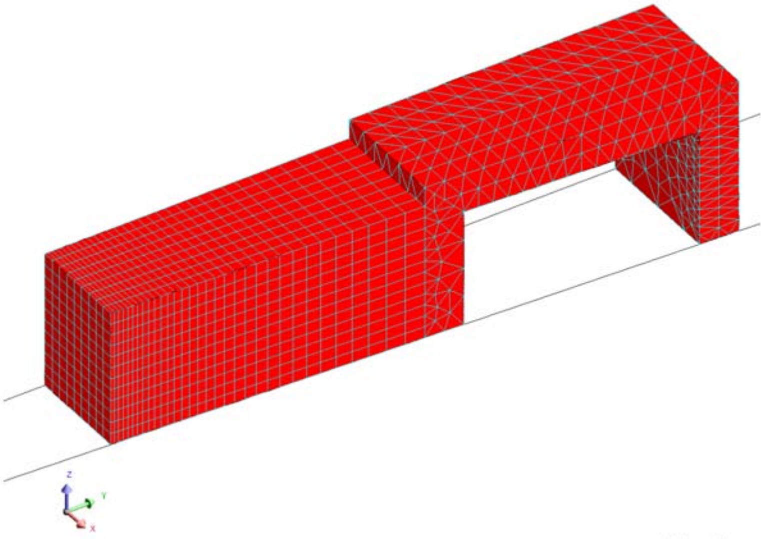

Figure 12.4: Mesh on the inductor

and a total power of 37 kW. The diffusion time is 0.2 s. In this phase the piece is not heated, this let a better distribution of the heat in the piece, which raise temperatures about 500 °C, like is possible to see from the simulation. In the last heating phase, during 0.2 s, the machine heat the piece with a power of 180 kW with high frequency of 190 kHz.

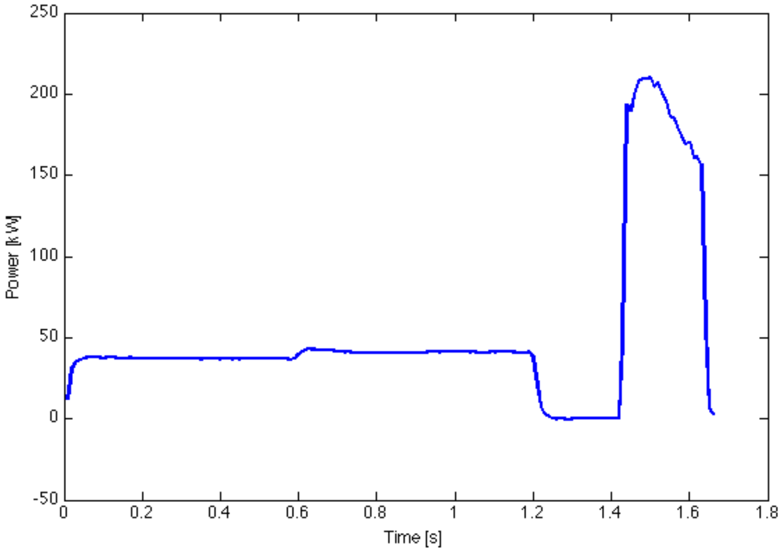

Figure 12.6: Power evolution during time

The tests were conducted in costant current mode, in this way is more easy to find the

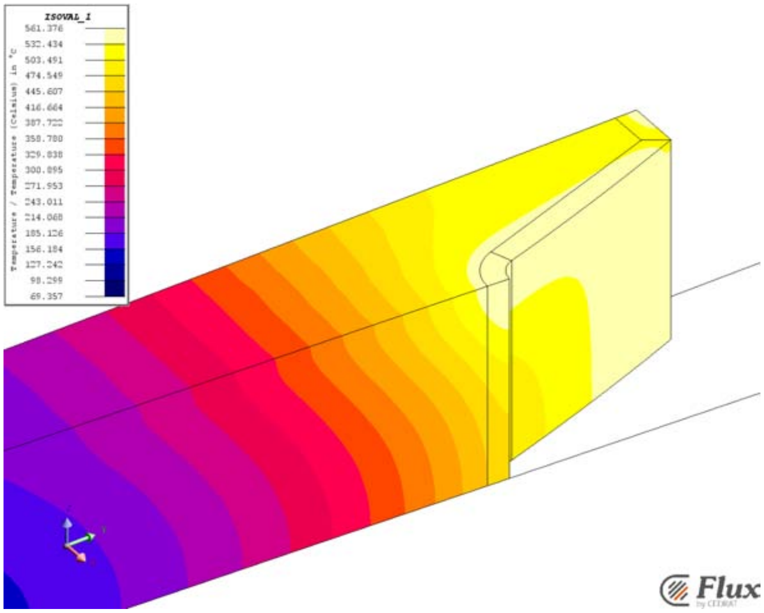
ISOVAL_1
Temperature / Temperature (Celsius) in °C
561.376
532.434
503.491
474.549
445.607
416.664
387.722
358.780
329.838
300.895
271.953
243.011
214.068
185.126
156.184
127.242
98.299
69.357
Flux

Figure 12.5: Temperature distribution at the end of MF phase

corrispondences with the simulations. In fact we can notate that the power in the principal heating phase varies a lot since it raise the Curie temperature. From the images taken we elaborate the following temperature isotherm, for the 816 °C.

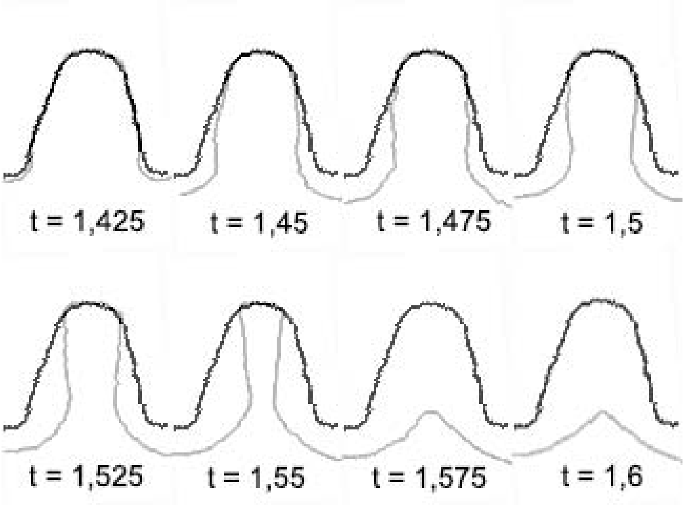

Figure 12.7:

12.3 Results

With these images it's possible to make a comparison with the simulation in same conditions.

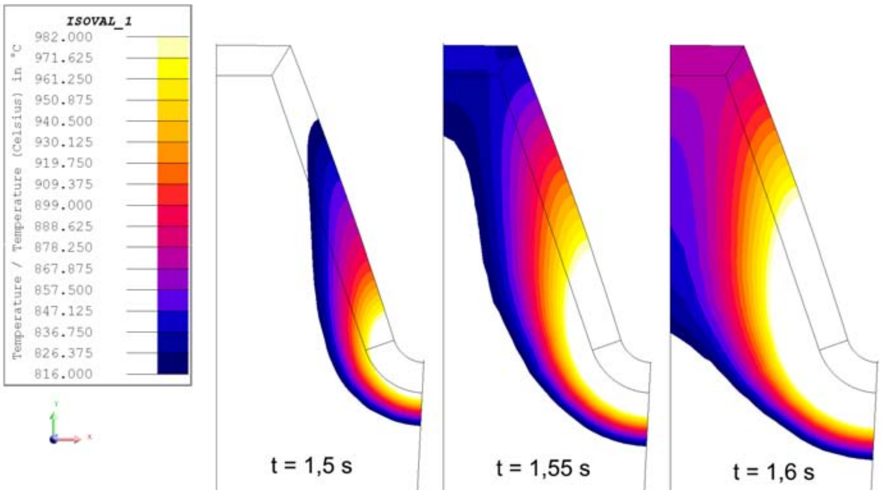
ISOVAL_1
Temperature / Temperature (Celsius) in °C
982.000
971.625
961.250
950.875
940.500
930.125
919.750
909.375
899.000
888.625
878.250
867.875
857.500
847.125
836.750
826.375
816.000
Y
X
t = 1,5 s
t = 1,55 s
t = 1,6 s

Figure 12.8: Temperature Distribution in Simulation in different time steps

It's possible to notice that the behavoiur of the isotherm is similare between test and simulation, there is a little difference in the steps around 1.55 s, maybe because the isotherm change completely in that period, and so a little time or material proprety mismatching could cause a significant difference between tests and simulations.

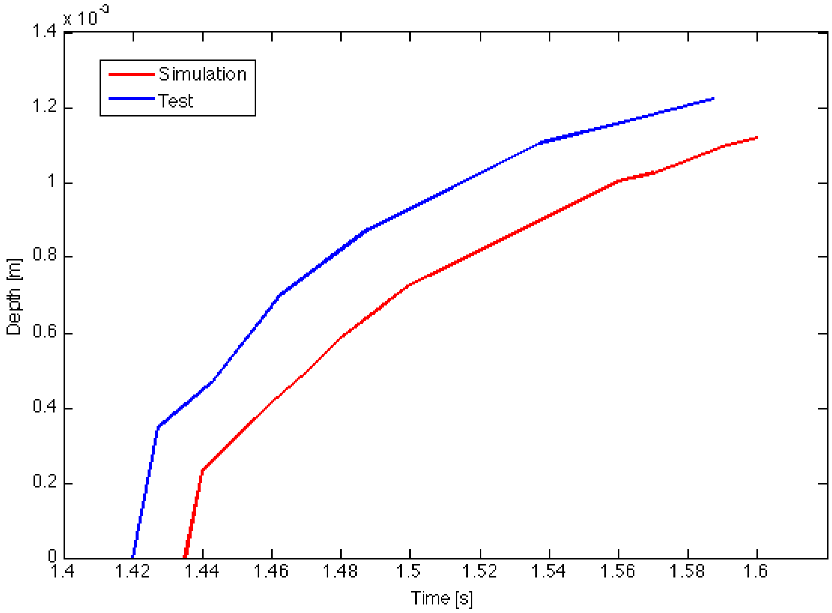

Figure 12.9: Depth of 816°C isotherm on the root of the gear

12.4 Edge Effect

After the test the piece was cutted, first at the root and then at the tip. Then the surfaces were polished and the applied etching, in this way is possible to define the transformation curve of the alloy.

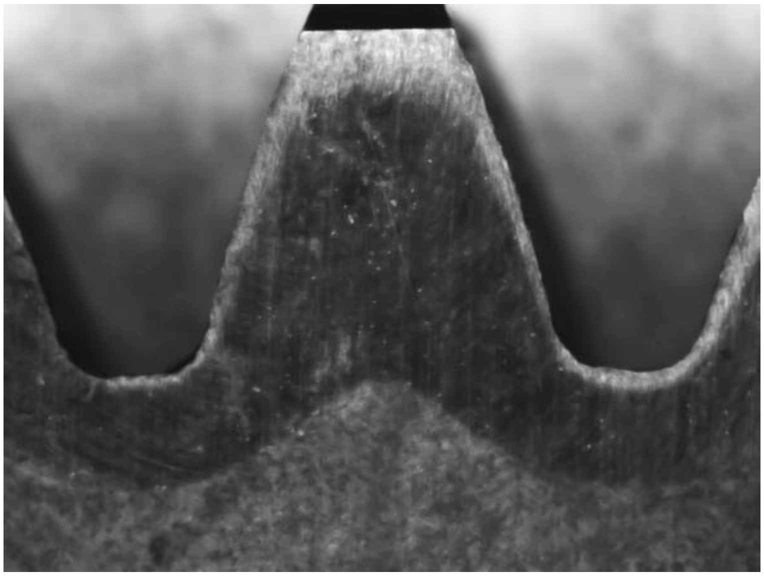

Figure 12.10: Tranformation curve on front of the piece

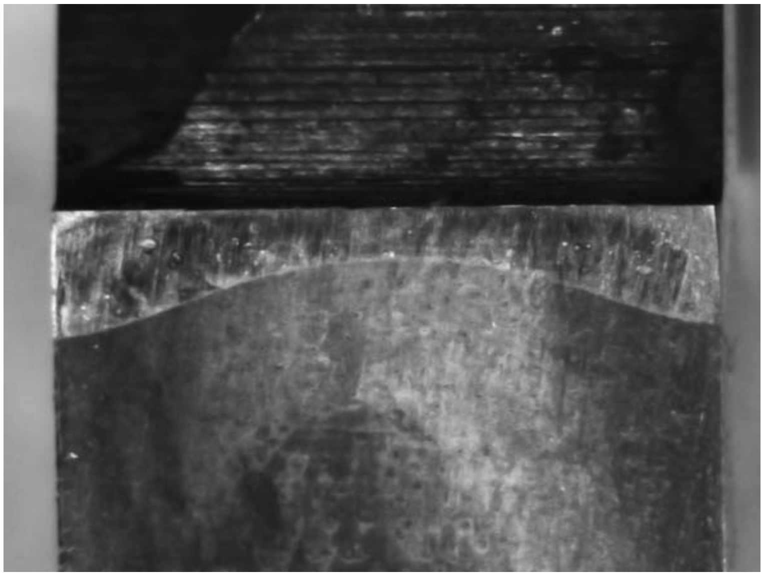

Figure 12.11: Transformation curve on the middle of the root

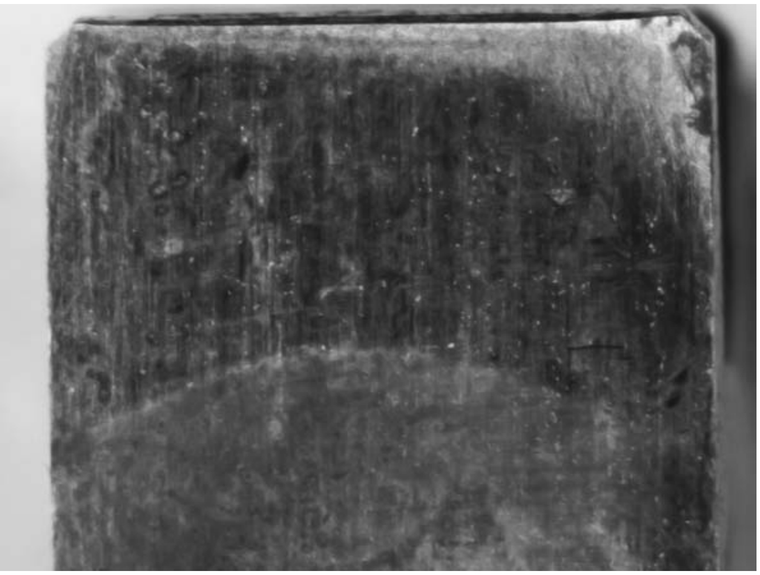

Figure 12.12: Transformation curve on the middle of the tip

Under the line the material is not transformed, in fact it maintain the same hardness as the beginnin , 33 HRC, and over the line the material is almost completely transformed, in fact it has an hardness of 55 HRC. To predict this lines with the simulation it's fundamental to find the correct transormation temperatures. In this simulation the AC1 temperature is supposed to be near 816 °C , so it's interesting to see the distribution of this isotherm in the depth on the root and tip.

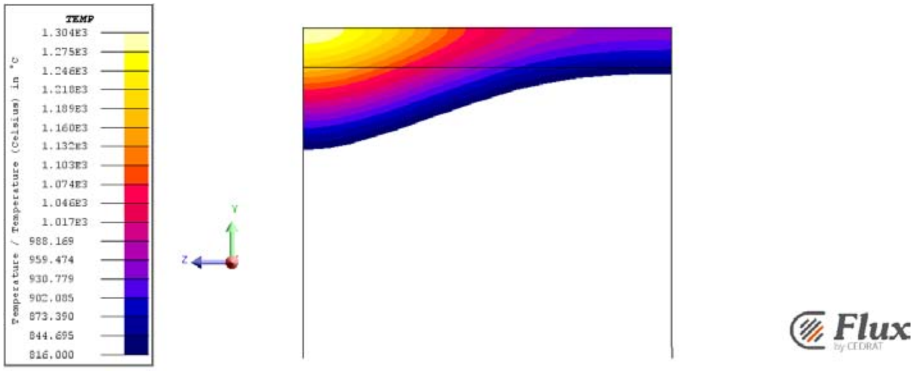

Figure 12.13: 816 °C isotherm distribution on the middle root

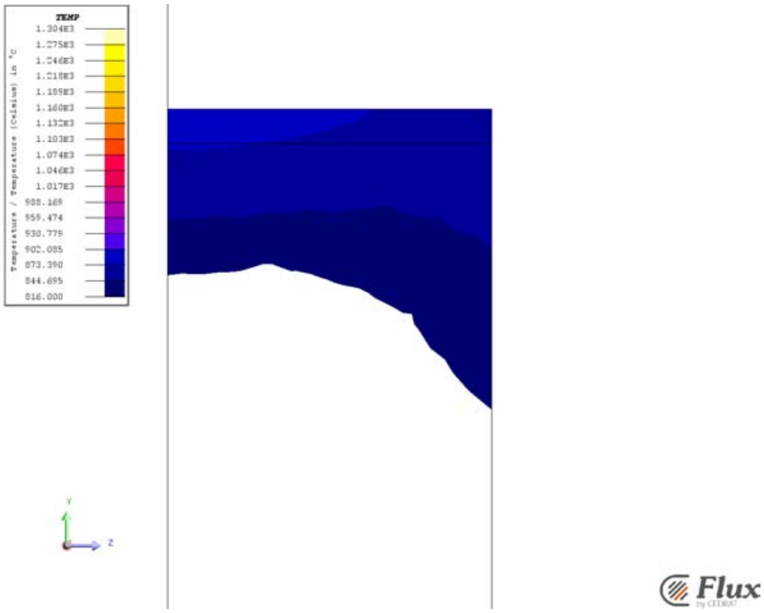

Figure 12.14: 816 °C isotherm distribution on the middle tip

It's possible to see how is similar the distribution of the isotherm on root with the transformation curve. This could due to this reasons: the temperature gradient on the root is high, so the heat doesn't penetrate too much in the depth, or the transformation temperature is really near to the 816 °C. But on the middle tip the situation is different, in fact the the isotherm is different from the transformation curve. This could be because the simulation stop after 1.6 seconds, but in reality the peace still have heat inside, and with the uniform of the temperature, could happend that the transformation curve is in more depth than the original isotherm.

12.5 Conclusions

As is possible to see the model developed responds quite well to the experimental requirements, and behaves in a very similar way to what has been analyzed in tests. The main differences are due both to a non-perfect data acquisition, both of the errors that may have developed in the choice of material parameters. However, it is known that it is impossible to characterize almost perfectly a material, and then in a numerical simulation there will always be an intrinsic error that reach as high as 5% of the exact solution. To improve the simulations so you can make further studies on the characterization of the material. In order to develop the recipes through simulations, and then verify it with experimental tests, it is best not to rely solely on the total power of the machine, but the actual current flowing in the inductor. For this reason it is interesting to be able to repeat part of the tests with the use of a probe Rogowsky that allows to correctly measure the current flowing in the inductor. In this way the current and the frequency will be the fundamental parameters of conjunction between the simulation and experimental tests.

References

[1] Candeo A. et al, “Multiphysics Modeling of Induction Hardening of Ring Gears for the Aerospace Industry” IEEE Transactions on Magnetics, Vol. 47, No. 5 (2011), pp. 918-921;

[2] Candeo A., “Induction hardening of components for the aerospace industry”, PhD Thesis, Università degli Studi di Padova, 2011

[3] Rudnev V., Loveless D., Cook R., Black M., “Handbook of Induction Heating”, CRC Taylor & Francis (2003);

[4] Lupi S., Dughiero F., Forzan M., “Modelling Single- and Double-Frequency Induction Hardening of Gear-Wheels”. The 5th International Symposium on Electromagnetic Processing of Materials, 2006, Sendai, Japan, ISIJ;

[5] Larregain B., Vanderesse N., Bridier F., Bocher P., Arkinson P., “Method for accurate surface temperature measurements during fast induction heating”, Proceedings of the 26th ASM Heat Treating Society Conference 2011;

[6] Lupi S., "Appunti di elettrotermia", A.A. 2005-2006;

[7] Barka N., “Etude de sensibilité du profil de dureté des engrenages traités thermiquement par induction en foncion paramétres machine”, PhD Thesis, ETS Montréal, 2011;

[8] Spezzapria M., “Simulazione numerica del processo di tempra ad induzione di ruote dentate per l’industria aeronautica”, Master thesis, Università Degli Studi Di Padova, 2011;

[9] Mingardi D., “Numerical Models for Induction Hardening of Gears”, Master thesis, Università Degli Studi Di Padova,2012;

[10] Marchesi G., “Lezioni di materiali per l’Ingegneria elettrica”, Libreria Progetto, Padova, 1998;

[11] Blut G. , “Effect de la geomtrie sur les parametres du generateur et le profil de duret lors d’une chauffe par induction : exprience et simulation,” Ph.D. dissertation, Ecole de technologie superieure, Montreal, QC, Canada, 2010. 148

[12] Segura G.M., “Induction heating converter’s design, control and modeling applied to continuous wire heating”, PhD Thesis, Universitat Politecnica de Catalunya, Barcelona, 2012

[13] Cuvelier F., Japhet C., Scarella G., “An efficient way to perform the assembly of finite element matrices in Matlab and Octave”, Inria Research Report, May 2013

[14] Young F.J., ”Induction Heating for Case Hardening Applications”, IEEE transaction on magnetics, VOL. MAG-13, NO. 6 , NOVEMBER 1977

[15] Binns K.J., Lawrenson P.J., Trowbridge C.W., ”The analytical and numerical solution of electric and magnetic fields”, John Wiley and Sons, 1992

Appendix

```
% Script for calculation of applied field on a gear starting from
% dimensional values like modulus m and number of teeth z
% and by electric values like current I and frequency f
clc;
clear all;
close all;

%% Calculation of geometric values

m=0.004;   %Gear Modulus [m]
z=48;   %Number of teeth
R=(z*m)/2;  %Primitive Radius
Re=R+m; %External Radius
Ri=R-(1.25*m);   %Internal Radius
step=m*pi();    %Gear Step
h=8.5*Re/10; %Limiting of studing domain high
s=0.01; %High of the Inductor [m]

%% Electric values
I=1000; %Current [A]
f=10000;    %Frequency [f]

H0=I/s;    %Imposed Field [A/m]
w=2*pi()*f; %Pulse omega
delta=0.00012;  %Skin Depth [m]

%% Mesh
%Define the boundary of domain
pv=[0 Ri;step/8 Ri;(3/8)*step Re;step/2 Re;step/2 h;0 h; 0 Ri];
%Define the relax rule for the mesh
fh=@(p) delta+2000*delta*dpoly(p,[0 Ri;step/8 Ri;(3/8)*step Re]);
fd=@(p) dpoly(p,pv);
%Creation of mesh
[p,t]=distmesh2d(fd,fh,delta,[0 h; step/2 Re],pv);



%% Defining Dirichlet Boundary
b=unique(boundedges(p,t));
j=1;
for i=1:length(b)
    if ((p(b(i),2)>(Ri-delta))&&(p(b(i),1)<step/4))
        dirich(j,1)=b(i);
        j=j+1;
    end

    if ((p(b(i),1)>step/8)&&(p(b(i),1)<step*3/8)&&(p(b(i),2)>Ri))
        dirich(j,1)=b(i);
        j=j+1;
    end

    if ((p(b(i),2)>(Re-delta))&&(p(b(i),1)>step/4))
        dirich(j,1)=b(i);
        j=j+1;
    end
end

N=size(p,1);T=size(t,1); % number of nodes, number of triangles

rho=ones(N,1).*2.5*10^-4;  %Resistivity
mu=ones(N,1).*20*4*pi()*10^-7; %Permeability



%% Building K,M matrixes

% [K,F] = assemble(p,t) % K and F for any mesh of triangles

% p lists x,y coordinates of N nodes, t lists triangles by 3 node numbers
K=sparse(N,N); % zero matrix in sparse format: zeros(N) would be "dense"
M=sparse(N,N);
F=zeros(N,1); % load vector F
a=zeros(N,2); % gradient matrix

```

```
for e=1:T  % integration over one triangular element at a time
  nodes=t(e,:); % row of t = node numbers of the 3 corners of triangle e
  Pe=[ones(3,1),p(nodes,:)]; % 3 by 3 matrix with rows=[1 xcorner ycorner]
  Area=abs(det(Pe))/2; % area of triangle e = half of parallelogram area
  C=inv(Pe); % columns of C are coeffs in a+bx+cy
  D=[2 1 1;1 2 1;1 1 2];
  % now compute 3 by 3 Ke and 3 by 1 Fe for element e
  grad=C(2:3,:);
  for i=1:3
      for j=1:3
          rhoe(i,j)=rho(nodes(i),1);
          mue(i,j)=mu(nodes(i),1);
      end
  end
  Ke=Area*grad'*grad./rhoe; % element matrix from slopes b,c in grad
  a(nodes,:)=a(nodes,:)+(grad'*10^-6);
  Me=(Area/12)*D./mue;
  K(nodes,nodes)=K(nodes,nodes)+Ke; % add Ke to 9 entries of global K
  M(nodes,nodes)=M(nodes,nodes)+Me; % add Me to 9 entries of global M

end

%% Implement Dirichlet Condition

F(dirich)=H0;
Fb=F;

ii=sqrt(-1);
Z=K+(ii*w*M); %Creation of complete general matrix
Z(dirich,:)=0; %Imposing zero on all element of dirichlet rows
Z(dirich,dirich)=-speye(length(dirich),length(dirich));
%Imposing ones on all diagonal element of dirichlet rows

%% Calculation
Zb=Z;
U=Zb\Fb;

H=abs(U);

j=1;
for i=1:length(b)
    if ((p(b(i),1)<delta)||(p(b(i),1)>((step/2)-delta)))
        neum(j,1)=b(i);
        j=j+1;
    end
end
a(neum,:)=zeros(length(neum),2);
a(dirich,:)=zeros(length(dirich),2);

J(:,1)=U.*a(:,1); % x component of J field
J(:,2)=U.*a(:,2); % y component of J field
J_abs=sqrt(abs(J(:,1)).^2+abs(J(:,2)).^2);


%% Plot the FEM approximation U(x,y) with values U_1 to U_N at the nodes
figure(2);
trisurf(t,p(:,1),p(:,2),0*p(:,1),H,'edgecolor','k','facecolor','interp');
title('H Field Distribution [A/m]');
view(2),axis([0 step/2 h Re]),axis equal,colorbar
hold on
plot(p(dirich,1),p(dirich,2));

figure(3);
quiver(p(:,1),p(:,2),J(:,2),-J(:,1));
title('J Field Arrows Distribution ');
view(2),axis([0 step/2 h Re]),axis equal,
hold on;
plot(pv(:,1),pv(:,2),'b');
hold off;
```

```
;;;;;;;;;;;;;;;;;MODIFIED FOR LORENZO;;;;;;;;;;;;;;;;;;;;;
;;;;(Chauffage par induction -    programme de base);;;;;
;;;;;;;;;;;;;;;;;;;;;;;;;;;;;;;;;;;;;;;;;;;;;;;;;;;;;;;;;


; RAPPEL COMMANDES :
; $A_OUT[i]=1 permet de mettre en route, d'activer
; $A_OUT[i]=0 permet de terminer, d'Èteindre
; i peut prendre les valeurs 1,2,3,4
; 1 = generateur MF
; 2 = douche
; 3 = RTM
; 4 = generateur HF
; S300 vitesse de rotation de broche 300 tr/min
; F2000 vitesse d'avance de broche 2000 mm/min
; F=2 attente de 2sec;
; Z=440 ou Z440 deplacement la position de l'axe verticale Z =440mm

;;;;;;;;;;;;;;;;;;;;;;;;;;;;;;;;;;;;;;;;;;;;;;;;;;;;;;;;;;;;;;;;;;
;;;;;;;;;;      DECLARATION VARIABLES PROGRAMME      ;;;;;;;;;;;;;
;;;;;;;;;;;;;;;;;;;;;;;;;;;;;;;;;;;;;;;;;;;;;;;;;;;;;;;;;;;;;;;;;;

DEF REAL COTE_CHAUFFE     ;POSITION DE CHAUFFE
DEF REAL COTE_DOUCHE      ;POSITION DE DOUCHE
;;;
DEF REAL TPS_R_DOUCHE     ;TEMPS DE RETARD POUR LE DECLENCHEMENT DE
LA DOUCHE.
;la douche s'enclenche ‡ la fin d'un temps Ècoule defini par un
compteur.
DEF REAL OFFSET_DOUCHE    ;Temps de retard entre la fin des chauffes
et
 l'enclenchement de la douche
DEF REAL TPS_DOUCHE       ;TEMPS DE FONCTIONNEMENT DOUCHE
DEF REAL TPS_REMPL_DOU    ;TEMPS DEMANDE D'UN REMPLISSAGE DOUCHE
;;;
;;;
DEF REAL TPS_PHASE_HF        ;TEMPS CHAUFFE HF
DEF REAL PUI_HF_PHASE     ;PUISSANCE CHAUFFE INTERMEDIAIRE HF
;;;
DEF REAL TPS_PHASE_MF    ;TEMPS CHAUFFE MF
DEF REAL PUI_MF_PHASE    ;PUISSANCE CHAUFFE MF
;;;
DEF REAL TPS_DIFF        ;TEMPS DIFFUSION
;;;;;;;;;;;;;;;;;;;;;;;;;;;;;;;;;;;;;;;;;;;;;;;;;;;;;;;;;;;;;;;;;;
;;;;;;;;;;       PARAMETRES PROGRAMME A MODIFIER      ;;;;;;;;;;;;
;;;;;;;;;;;;;;;;;;;;;;;;;;;;;;;;;;;;;;;;;;;;;;;;;;;;;;;;;;;;;;;;;;

GAMM="ESSAI"                 ;NOM GAMME POUR RTM

COTE_CHAUFFE =409.175      ;COTE DE CHAUFFE

;RECETTE

TPS_PHASE_HF= 0.2        ;TEMPS CHAUFFE HF
```

```
PUI_HF_PHASE= 65         ;PUISSANCE CHAUFFE INTERMEDIAIRE HF

TPS_PHASE_MF= 1.2        ;TEMPS CHAUFFE MF
PUI_MF_PHASE= 3.2        ;PUISSANCE CHAUFFE MF

TPS_DIFF= 0.15            ;TEMPS DIFFUSION

;DOUCHE

COTE_DOUCHE= 440

;;;;;;;;;;;;;;;;;;;;;;;;;;;;;;;;;;;;;;;;;;;;;;;;;;;;;;;;;;;;;;;
;;;;;;;;;;;;;;;      DEBUT DU PROGRAMME      ;;;;;;;;;;;;;;;;;;
;;;;;;;;;;;;;;;;;;;;;;;;;;;;;;;;;;;;;;;;;;;;;;;;;;;;;;;;;;;;;;;

M181                       ;ENVOI GAMM VERS RTM

M71                        ;MODE_BROCHE
M3 S0                      ;MARCHE ET VITESSE ROTATION BROCHE
M106                       ;OUVERTURE PORTE SI DESIRE, ENLEVER ;
G1 F2000 Z=COTE_CHAUFFE    ;DEPLACEMENT A LA COTE CHAUFFE

MSG ("ATTENTE RTM PRETE")
RTMOK:
STOPRE
IF $A_IN[4]==0 GOTOB RTMOK       ;TEST SI CANAL 1 RTM EST PRET
M195                       ;SURVEILLANCE DEBIT DOUCHE  INACTIVE
;M196                       ;SURVEILLANCE DEBIT DOUCHE  ACTIVE

G4 F=150

Z400              ;DEPLACEMENT A LA COTE VOULUE AVANT LE PROCESS

G4 F=2

G1 F2000 Z=COTE_CHAUFFE    ;DEPLACEMENT A LA COTE CHAUFFE

TRAITEMENT:
MSG ("TRAITEMENT EN COURS")

$A_OUT[3]=1                ;DEPART RTM


;;;PHASE: LES CHAUFFES INTERMEDIAIRES;;;

;CHAUFFE MF (PRE-CHAUFFE)
H6=PUI_MF_PHASE                   ;CONSIGNE DE CHAUFFE MF EN %
$A_OUT[1]= 1                      ;DEPART CHAUFFE MF
G4 F=TPS_PHASE_MF                 ;TEMPS DE CHAUFFE
$A_OUT[1]= 0                      ;ARRET CHAUFFE MF

;DIFFUSION TIME
G4 F=TPS_DIFF
```

```
;CHAUFFE PRINCIPAL HF
H7=PUI_HF_PHASE                     ;CONSIGNE DE CHAUFFE HF EN %
$A_OUT[4]=1                         ;DEPART CHAUFFE HF
G4 F=TPS_PHASE_HF                   ;TEMPS CHAUFFE
$A_OUT[4]=0                         ;ARRET CHAUFFE HF

G4 F=2

;PHASE 4 : LA TREMPE

G0 Z=COTE_DOUCHE          ;DEGAGEMENT POSITION DOUCHE

;FIN DU PROCESS - DEGAGEMENT DE PIECE ET FIN D'ACQUISITION
$A_OUT[3]=0               ;ARRET RTM - FIN DE L'ACQUISITION

G1 Z440 F400              ;DEGAGEMENT POSITION CHARGEMENT

MSG ("ATTENTE RTM PRETE")
RTMPRET:
STOPRE
IF $A_IN[4]==0 GOTOB RTMPRET
M106                       ;OUVERTURE PORTE - PAS DEJA OUVERTE
M241                       ;+1 DANS COMPTEUR
M02                        ;FIN DU PROGRAMME
```